2018

Selective Deposition of Platinum by Strong Electrostatic Adsorption onto Cobalt- and Iron-based Catalysts for Fischer-Tropsch Synthesis

Fahad A. Almalki
University of South Carolina

Selective Deposition of Platinum by Strong Electrostatic Adsorption onto Cobalt- and Iron-based Catalysts for Fischer-Tropsch Synthesis

by

Fahad A. Almalki

Bachelor of Science
King AbdulAziz University, 2001

Master of Science
King Saud University, 2009

Submitted in Partial Fulfillment of the Requirements

For the Degree of Doctor of Philosophy in

Chemical Engineering

College of Engineering and Computing

University of South Carolina

2018

Accepted by:

John R. Regalbuto, Major Professor

John R. Monnier, Committee Member

Christopher T. Williams, Committee Member

Aaron K. Vannucci, Committee Member

John W. Weidner, Committee Member

Cheryl L. Addy, Vice Provost and Dean of the Graduate School

DEDICATION

Dedicated to my wife, Faysah Almalki, she is always working hard with me. The hardships and challenges are easy with her. Dedicated to my kids, Abdulaziz, Lana, Yazeed, and Yoseph. They love engineering and science subjects and I always have interesting and encouraging discussions with them. To my parents, Abdulaziz Almalki and Thuraya Almalki, they wish all the best for me and never hesitated to support me.

ACKNOWLEDGMENTS

First, I would like to express my sincere appreciation and gratitude to my academic advisor, Dr. John R. Regalbuto. Dr. Regalbuto never stopped his support and advice all the time during my course of doctoral study. I have been exposed under his supervision to a valuable experience and knowledge that boosted my excitements and interests in scientific research. Taking the opportunity to work at CReF was a great experience in heterogeneous catalysis and expanded my knowledge of science and engineering principles. Also, I would like to deeply thank Dr. John R. Monnier, a member of my committee, for valuable discussions and guidance, especially in catalytic activity measurements and reaction performance experiments.

My special thanks to the other committee members, Dr. Christopher T. Williams, Dr. Aaron K. Vannucci and Dr. John W. Weidner for their valuable input, reviewing my work and dissertation and for their scientific expertise.

I would like to give a great mention to my colleagues and all CReF people, with whom I have shared knowledge, experience, and interesting discussions. Special appreciation for them and their enthusiasm for research, interests in team-work, and productivity. I would like to thank all people in chemical engineering and chemistry departments, whom I worked with or got help from in research facilities, laboratories, and various analytical equipment.

ABSTRACT

Cobalt and iron based catalysts are commercially predominant for Fischer-Tropsch synthesis, Co-based catalysts for their stability, activity, and inactivity for the water gas shift reaction and Fe-based catalysts for their cheap cost, high light-olefins and alcohols selectivity, and tolerance to H_2/CO ratio. These catalysts are structure sensitive with lower activity at nanoparticle sizes smaller than 6-8 nm. Co-based catalysts exhibit high activity, low CH_4 selectivity, and high C_5^+ selectivity, while Fe-based catalysts are more selective to low-molecular-weight hydrocarbons such as olefins and alcohols. The reducibility of cobalt and iron is another important factor which may be key for improving their performance, and this might be achieved by adding a noble metal which, via hydrogen spillover, can facilitate Co oxide and Fe oxide reduction to the metal nanoparticles which are more active for CO hydrogenation reaction.

The promotion of transition metals by a noble metal will be most efficacious if the noble metal is in direct contact with transition metal nanoparticles, and none is wasted on the surface of the support. In this study, we demonstrate that such a selective deposition is possible. We first employ incipient wet impregnation to synthesize silica supported cobalt oxide and iron oxide catalysts of the optimum size. Second, Pt is steered onto the transition metal oxide surfaces by controlling the impregnation pH. We compared these samples at various Pt loadings to Pt/Co and Pt/Fe catalysts of the same nominal composition prepared by the common, undirected method of co-impregnation of Pt-Co and Pt-Fe. Cobalt and

iron loadings were 10 wt % and Pt loading varied between 0.03 and 1.72 atomic % in each catalyst set. Catalysts were characterized by XRD, TPR, and STEM. The catalyst reactivity was evaluated at conventional Fischer-Tropsch conditions of (220^{o}C for Pt-Co/SiO_2 and 250 for Pt-Fe/SiO_2) and 20 bar with a H_2/CO ratio of 2:1.

The reactivity of the Co catalysts clearly depends on the preparation method, which can be attributed to the intimate coordination of Pt with Co. At higher Pt loadings, the Pt has effects not only on Co oxide reduction but also are extended to Fischer-Tropsch reaction itself. At very low Pt loadings, the promotional role appears to be limited to improving Co reducibility. Methane selectivity is decreased and C5+ selectivity is increased by unprecedented levels. Thus, promotion of Co by Pt for FTS is effective with very small amounts of Pt selectively adsorbed onto the Co phase.

The effect of Pt on Fe-based catalysts is different from the one in the Co-based catalyst. The effect on Fe-based catalysts is limited to the promotional of iron oxide reduction, and no promotional effect was observed for the FT reaction. This difference in Pt effects for Co/SiO_2 and Fe/SiO_2 reaction performance is attributed to the nature of the active phase, thus, the active phase in Co-based catalyst is the Co^0 metal phase, which is strongly promoted by Pt, while Fe carbide is the widely accepted active phase and therefore the Pt has no promotional effect on transformation Fe-oxides species to Fe-carbides in a H_2 environment.

TABLE OF CONTENTS

Dedication iii

Acknowledgement iv

Abstract v

List of Tables ix

List of Figures x

Chapter 1: Introduction to Fischer-Tropsch Technology..... 1

1.1 The global energy future: Fischer-Tropsch synthesis overview..... 1

1.2 Fischer-Tropsch reaction kinetics and mechanism..... 5

1.3 Catalysts for Fischer-Tropsch Synthesis 11

1.4 Fischer-Tropsch supported-metal catalysts syntheses..... 17

1.5 Synthesis of Catalysts..... 22

1.6 Dissertation layout..... 40

Chapter 2: Rational synthesis of bimetallic catalysts: experiments and characterization 41

2.1 The hypothesis of rational deposition of platinum onto transition metal oxide surfaces. 41

2.2 Control experiements – PZC and Pt adsorption measurements..... 44

2.3 Discussion..... 54

2.4 Conclusion..... 58

Chapter 3: Characteristics and Catalytic Activity of Platinum-Promoted Cobalt-based Catalysts..... 59

3.1. Introduction..... 59

3.2. Materials and methods..... 64

3.3. Results and discussion. 69

3.4. Conclusion..... 84

Chapter 4: Characteristics and CatAlytic Activity of Platinum-Promoted Iron-Based catalysts..... 85

4.1. Introduction..... 85

4.2. Methods and materials..... 87

4.3. Results and discussion..... 88

4.4. Conclusion..... 99

References..... 101

LIST OF TABLES

Table 1.1: Typical hydrocarbons distribution for LTFT and HTFT 12

Table 3.1: Pt weight loading and Pt/Co atomic % based on SEA uptake onto Co/SiO_2 .. 69

Table 3.2: Co and Pt species particles size of $Pt\text{-}Co/SiO_2$ sequential IWI + SEA 73

Table 3.3: Co and Pt species particles size of Pt-Co/SiO2 simultaneous IWI..... 73

Table 3.4: TOF and CTY of $Pt\text{-}Co/SiO_2$ sequential IWI + SEA 77

Table 3.5: TOF and CTY of $Pt\text{-}Co/SiO_2$ simultaneous IWI 77

Table 3.6: FT activity and hydrocarbons selectivity comparisons 83

Table 4.1: Pt weight loading and Pt/Fe atomic % based on SEA uptake onto Fe/SiO2 ... 89

Table 4.2: TOF and FTY of $Pt\text{-}Fe/SiO_2$ sequential IWI + SEA 98

Table 4.3: TOF and FTY of $Pt\text{-}Fe/SiO_2$ simultaneous IWI 98

LIST OF FIGURES

Figure 1.1: Oxygenate (enol) mechanism of CO hydrogenation reaction 6

Figure 1.2: Carbide mechanism including dissociative CO hydrogenation 7

Figure 1.3: Product distribution of FTS function of chain growth probability..... 9

Figure 1.4: illustration of various impregnation techniques 29

Figure 1.5: ideal concentration range for Precipitation-deposition process 30

Figure 1.6: The regime of Strong Electrostatic Adsorption (SEA) 32

Figure 1.7: pH shift model simulation with varying surface loading for Alumina (PZC=8.5) 33

Figure 1.8: Charging condition and adsorption constants of the γ-alumina surface by RPA model..... 35

Figure 1.9: Anionic and cationic Pt complexes adsorption onto gamma-alumina 36

Figure 1.10:steric-close-packed adsorption of CPA retaining one hydration sheath..... 37

Figure 1.11: RPA-prediction curves of CPA and PTA complex based on PZC of oxides38

Figure 1.12: Electron microscopy characterization of Pt/Silica catalysts prepared by SEA method..... 39

Figure 2.1: Schematic of the use of SEA based on the surface potential of Co_3O_4 and SiO_2 42

Figure 2.2: Pt-Co sequential preparations using IWI for Co/SiO_2 and SEA for Pt onto Co/SiO_2 43

Figure 2.3: Control experiments of metal-free solution pH shift data for SiO_2 at different surface loading 44

Figure 2.4: Control experiments of metal-free solutions pH shift date for pure oxides slurries (Co_3O_4 + Fe_2O_3) 46

Figure 2.5: Pt uptake onto pure oxides (Co_3O_4, Fe_2O_3, and SiO_2) 47

Figure 2.6: Control experiments pH shift of pure oxides (Co_3O_4 and Fe_2O_3) at SL = 1000 m^2/L 48

Figure 2.7: STEM images and EDXS results of samples reduced at 250ºC (a) Pt/(Co_3O_4+SiO_2), (b) Pt/(Fe_2O_3+SiO_2) 49

Figure 2.8: Pt uptake survey of 200 ppm CPA with 500m/L SL for silica supported Co- and Fe- based catalysts 51

Figure 2.9: STEM images for (a) Pt-Co/SIO_2 sequential IWI-SEA (b) Pt-Co/SIO2 sequential IWI-SEA and their EDXS analyses 52

Figure 2.10: STEM images for (a) Pt-Co/SiO_2 simultaneous IWI (b) Pt-Co/SiO_2 simultaneous IWI and their EDXS analyses 53

Figure 3.1: The influence of Co particle size on (a) activity normalized to the cobalt loading (b) TOF, (c) methane selectivity, (d) hydrogenation 61

Figure 3.2: Fischer-Tropsch reaction flow system equipped with GC 68

Figure 3.3: XRD profiles of Pt-Co/SiO_2 sequential IWI +SEA catalysts 70

Figure 3.4: XRD profiles for Pt-Co/SiO_2 simultaneous IWI catalysts 71

Figure 3.5: TPR profiles of Pt-Co/SiO_2 sequential IWI + SEA 75

Figure 3.6: TPR profiles of Pt-Co/SiO2 simultaneous IWI 75

Figure 3.7: CO conversion % for (a) Pt-Co/SiO_2 sequential IWI +SEA (b) Pt-Co/SiO_2 simultaneous IWI 78

Figure 3.8: Hydrocarbon selectivity (a) Pt-Co/SiO_2 sequential IWI +SEA (b) Pt-Co/SiO_2 simultaneous IWI 79

Figure 3.9: Olefin/Paraffin ratio for hydrocarbons of (a) Pt-Co/SiO_2 sequential IWI +SEA (b) Pt-Co/SiO_2 simultaneous IWI 80

Figure 4.1: XRD profiles of Pt-Fe/SiO_2 sequential IWI +SEA catalysts 90

Figure 4.2: XRD profiles of Pt-Fe/SiO_2 simultaneous IWI catalysts 90

Figure 4.3: TPR profiles of Pt-Fe/SiO_2 sequential IWI + SEA 92

Figure 4.4: TPR profiles of Pt-Fe/SiO_2 simultaneous IWI 93

Figure 4.5: CO conversion % for (a) Pt-Fe/SiO_2 sequential IWI +SEA (b) Pt-Fe/SiO_2 simultaneous IWI 94

Figure 4.6: Hydrocarbon selectivity (a) Pt-Fe/SiO_2 sequential IWI +SEA (b) Pt-Fe/SiO_2 simultaneous IWI 95

Figure 4.7: Olefin/Paraffin ratio for hydrocarbons of (a) Pt-Fe/SiO_2 sequential IWI +SEA (b) Pt-Fe/SiO_2 simultaneous IWI 96

Figure 4.8: CO_2 selectivity for (a) Pt-Fe/SiO_2 sequential IWI +SEA (b) Pt-Fe/SiO_2 simultaneous IWI 97

CHAPTER 1

INTRODUCTION TO FISCHER-TROPSCH TECHNOLOGY

1.1 The global energy future: Fischer-Tropsch synthesis overview

Today, one of the world's major issues is to afford and maintain a sustainable and renewable source of energy. The world's demand for fossil fuels is projected to increase by 28 %, from 575 Q Btu in 2015 to 736 Q Btu in 2040 [1]. Despite worldwide policies to encourage renewable energy use, OPEC projected an increase in world oil consumption in 2016 higher than the expected 95.4 m b/day, to 102.3 m b/d [2]. Significant growth in the global economy, increase in the world's population and the high rate of urbanization are the main reasons for increasing energy demand globally and they play an important role in the world's energy security for new generations. Accordingly, one of the major key components associated with the growing world economy is transportation. Consequently, an increase in the world transport activity would increase air pollution, including greenhouse gas emissions (GHG). This is attributed to a combustion of transport fuels which are mainly produced from fossil fuels. Transportation is responsible for more than 24% of the world CO_2 emissions in 2015, the second largest contributor after electricity (42%), and it has increased by 68% since 1990. The growth of transportation energy consumption is considered the highest of all other sectors [3-4].

Light-duty vehicles and freight trucks account 75% of road vehicle use. In fact, there are many factors playing major roles in the projected growth in road traffic fuels such as decentralized cities, economic development in some countries and high rate of urbanization around the world, which would accelerate the demand rate on road traffic due to an expected increase access to personal and public vehicles [5]. However, gasoline and diesel are the fuels predominantly used, as they are blends of hydrocarbons ranging from C_4-C_{12} and C_9-C_{27} respectively. Both include paraffin (alkanes), olefins (alkenes), cycloalkanes (naphthenes), as well as smaller amounts of sulfur, nitrogen, oxygen, and metal compounds [6]. Diesel is projected to be the most used transport fuel because of its high efficiency and high energy density compared to gasoline.

The higher efficieny of diesel engines stems from self-ignition, which occurs as the compressed air temperature exceeds the diesel fuel's self-ignition temperature at a higher compression ratio of diesel compared to gasoline engines [5]. The self-ignition quality can be measured by the cetane rating which is referred to hexadecane $C_{16}H_{34}$ hydrocarbon that easily ignites when exposed to air with a small amount of heat [7]. Therefore, high cetane diesel is more ideal, burning with high efficiency and less CO_2 emission.

A promising technology, Fischer-Tropsch Synthesis (FTS), can effectively and commercially produce synthetic diesel or gasoline, has gained significant attention with vast investments in research. Fischer-Tropsch Synthesis is well-established process commercialized around the world. FTS can improve the production and quality of fuels that would meet the world's energy demand and the global environmental constraints [8] & [9].

FTS converts synthesis gas, a mixture of CO and H_2, to a wide range of hydrocarbons, consisting of paraffins, olefins, alcohols, aldehydes, and ketones. Historically, in 1932 Hans Fischer and Franz Tropsch were the first scientists to propose the production of a mixture of hydrocarbons, "Synthine", by converting CO and H_2 under high pressure over Co and Fe based catalysts. Just a few years later in 1936, the first large scale FT reactor began operation and was commercialized in Braunkohle-Benzin, Germany, converting coal-based syngas to hydrocarbon products. From 1955 to 1982, Sasol completed 3 major processes, Sasol I, II, and III, in Sasolburg, South Africa. Significant development was accomplished during that time toward the design of catalysts, reactor, and processes of FTS [10-11]. Since the 1980s, an investment in FTS has been conducted worldwide with a great interest in geographically distributed energy resources.

Abundant, versatile, affordable and well-distributed world natural gas resources are attracting petroleum and petrochemical societies to heavily invest in research to develop and improve FTS performance and productivity toward clean and sustainable fuels and chemicals. This process of converting natural gas to liquid fuels is known as gas to liquid process (GTL). However, FTS is the main part of this process, in which the syngas is converted to hydrocarbons. Syngas can be produced either by partial oxidation, steam reforming, or methane reforming. The produced syngas is then processed via FTS to produce a wide range of hydrocarbons, alchols and waxes. Upgrading FT products via hydrocracking and isomerization processes are always integrated into GTL as further desired products are produced and their selectivity increased ,such as gasoline and diesel [12-14].

Another primary feedstock that has been utilized for liquid fuel production is coal, which is the predominant source of energy for electricity and still prevails in gasification technology. In fact, this technology is considered one of the most versatile and important processes in the world's industry and energy sectors [15]. However, using coal to produce syngas and generate power plants has technical and environmental drawbacks, such as high CO_2 emissions during the burning process and H_2-deficiency with a H_2/CO ratio less than 0.8. Thus, an additional H_2-adjusted process is required to increase subsequent processes' efficiency, particularly in FTS process, which requires sufficient H_2/CO ratio in the catalytic polymerization-like reaction [16-17].

Today, biomass plays an important role as a potential and major alternative energy source, because of diverse materials, abundance, and carbon neutral characteristics. Biomass-based syngas gasification is perceived as a promising source of energy when combined with reliable, commercial and attractive FTS technology. Biomass can be derived from a wide range of raw materials such as wood derivatives, high-yield energy crops, and agriculture crops [18-19]. The main challenges in biomass utilization for renewable energy production are its high content of moisture, oxygen, and particulates, which require further processes for liquid separation and scale-up issues [20]. Under current estimates of the world's energy consumption, demand, and projected scenario, the utilization of biomass as an energy supply could meet about 30% of the world's total energy supply by 2050 [21]. Biomass to Liquid (BTL) Fischer-Tropsch integrated processes are mostly limited to research-laboratory scale and still facing process and chemistry-related problems. Thus, researchers and scientist are interested in exploring the BTL pilot scale up to a large industrial scale [22].

1.2 Fischer-Tropsch reaction kinetics and mechanism

FT reaction is basically a surface polymerization-like reaction, hydrogenating adsorbed CO, which is assumed to be dissociative adsorption on an active site, producing different hydrocarbons during subsequent mechanisms of C-C coupling, chain growth, and termination steps. In the hydrogenation of adsorbed CO on a transition metal active site, an average release of heat is reported as 35 kcal [23]. Therefore, the high exothermicity effect requires heat removal and is considered to play a major role in the reactor and catalyst design for FTS. This hydrogenation effect is extended for different hydrocarbon reactions that simultaneously take place on the surface [24-26].

$$(2n+1)H_2 + nCO \rightarrow C_nH_{2n+2} + nH_2O \quad \text{(alkanes) (1.1)}$$

$$2nH_2 + nCO \rightarrow C_nH_{2n} + nH_2O \quad \text{(alkenes) (1.2)}$$

$$2nH_2 + nCO \rightarrow C_nH_{2n+2}O + (n-1)H_2O \quad \text{(alcohols) (1.3)}$$

$$CO + H_2O \rightarrow CO_2 + H_2 \quad \text{(water gas shift) (1.4)}$$

$$2CO \rightarrow C + CO_2 \quad \text{(Boudouard) (1.5)}$$

Regardless of what reaction takes place, all depend on dissociative chemosorption of CO. Therefore the metal active site that is exposed to CO has to have the ability to adsorb CO and then break the C-O bond, but this dissociation process is still uncertain. Many researchers have tried to explain the dissociation of adsorbed CO with different mechanisms, specifically, through unassisted C-O dissociation or H-assisted C-O dissociation [27].

One of the early mechanisms that was widely recognized in the early 1950s is called enol mechanism. It starts with non-dissociative CO adsorption followed by the hydrogenation to form adsorbed OHCH. This mechanism is characterized by the elimination of water, hydrogenation of adsorbed R-OH and coupling of OH-R – R-OH as depicted in Figure 1.1. The insertion of the OH group that is coupled with C during the H_2O elimination step is proposed in this mechanism, instead of C-O cleavage. The chain propagation is formed by repeating the pattern of H_2O elimination, hydrogenation, and C-C coupling, but the termination step for this mechanism and insertion of C-OH are not described [28-30].

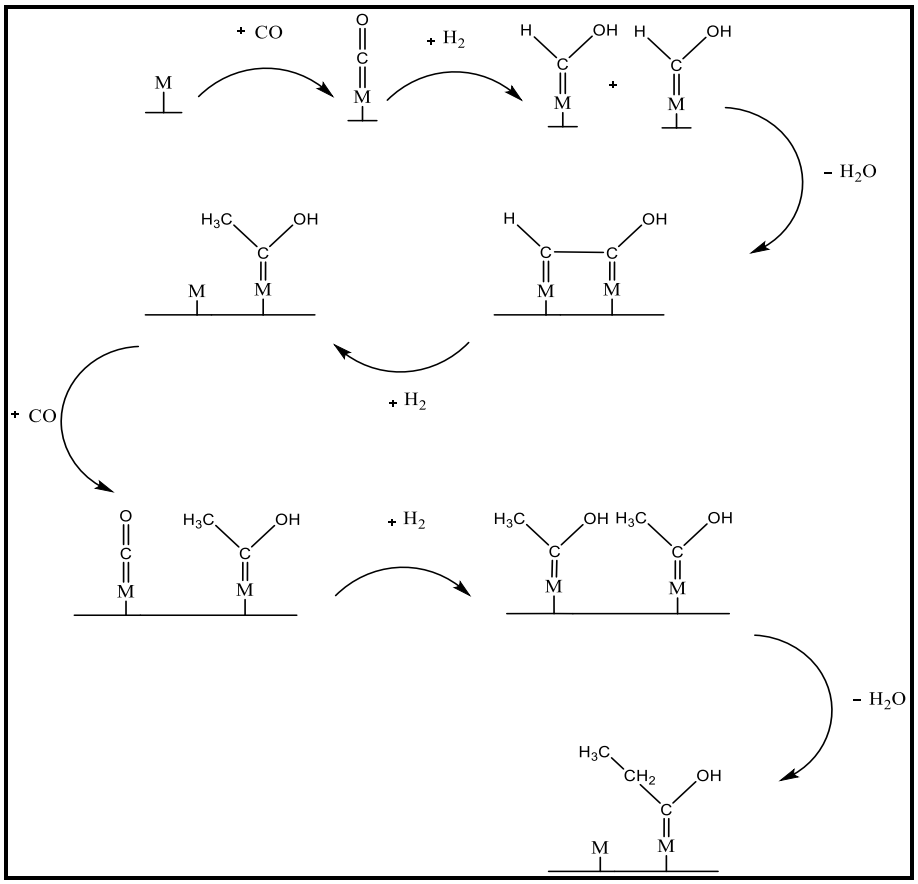

Figure 1.1: Oxygenate (enol) mechanism of CO hydrogenation reaction

Later, the dissociative adsorption of CO was proposed as a mechanism in which CO would be adsorbed on two active sites forming a bridge of a C-O bond with the metal active site. Then, the C-O bond would be cleaved, forming C-M and O-M surface species. The dissociative chemisorbed H facilitates a hydrogenation reaction of C-M and O-M species, and with one further hydrogenation reaction, H_2O molecules are released. Following this, many subsequent hydrogenations take place, converting M-C to methyl surface intermediates M-CH_x. It is anticipated that surface methyl intermediates are subjected to the C-C coupling reaction, which is known as the chain propagation of methyl group monomers, forming M-R-HCOH. Therefore, thus the length of intermediate R is a major key factor in FTS, which determines the hydrocarbons' selectivity [31-32].

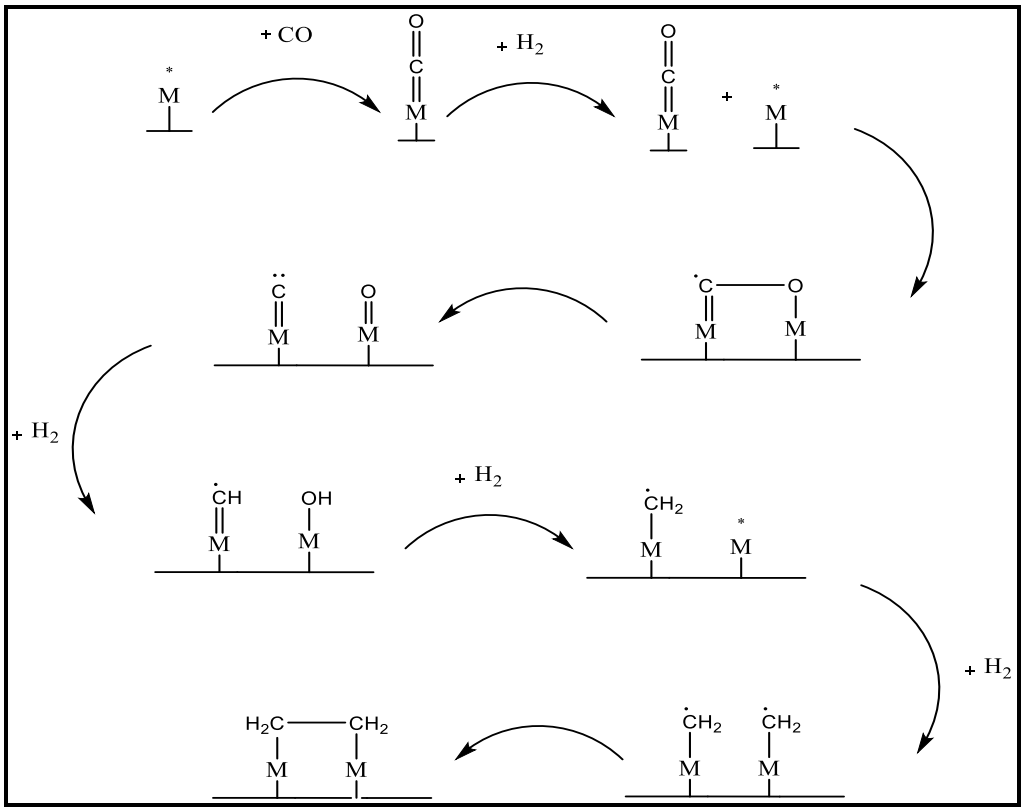

Figure 1.2: Carbide mechanism including dissociative CO hydrogenation

Many of the pathways introduced to interpret the FT reactions consist of many high-exothermic reactions that can be described by many different mechanisms. In general, the reaction conditions could alter the mechanism pathways e.g. the high FT reaction temperature would increase the hydrogenation rate, thus the methanation rate would increase and decrease the the C_{5+} selectivity. While the low reaction temperature would slow the hydrogenation rate to a level at which the longer hydrocarbon-chain would be more selective, and as a result the C_{5+} selecivity increases [33-34]. In most FT mechanisms, the chain propagation step is mostly described by M-CH_x monomers coupling to then form long chain intermediates with the different functional groups.

In the termination mechanism, hydrocarbon intermediates are usually terminated from the surface by two mechanisms, either when hydrogenated CH-M is bonded to the surface site or when adsorbed surface CH_3 is coupled with another group. The nature of the methylene M-CH_2 monomers coupling has been reported to be more complicated, due to different methylene groups expected to form during the reaction mechanism and based on energy barriers which have been described by many mechanisms with different CH_x species [35-37]. Consequently, complexity in describing the FT reaction mechanism has resulted in difficulties in controlling the selectivity of desired hydrocarbons. As well, the FTS mechanism depends on many factors, such as reaction conditions, type of catalyst, physicochemical characteristics of the catalyst, and the design of the FT reactor. Therefore, an early, simple and one dependent-variable relationship was introduced to describe FT hydrocarbon product distribution.

$$M_n \rightarrow (1-\alpha)\alpha^{n-1} \qquad \text{(ASF) (6)}$$

This relationship is known as the Anderson-Schulz-Flory equation (ASF) by which the product distribution of hydrocarbons can be determined by chain growth probability (α) as shown in equation (6). M_n represents the hydrocarbon molar fraction and "n" is the carbon number. However, ASF is a simplified relation that cannot describe well the gasoline and diesel ranges of hydrocarbons as seen in figure 1.3. The high rate of re-adsorption of α-olefins C_2 and C_3 was reported to be the main reason for this deviation from ideal ASF, particularly in low molecular-weight hydrocarbons. Therefore, the experimental analysis of light hydrocarbon products is underestimated especially in Co-based catalysts. In general, chain-growth probability (α) is strongly influenced by reaction pressure, temperature, syngas composition, type of catalysts, and promoters [38-41].

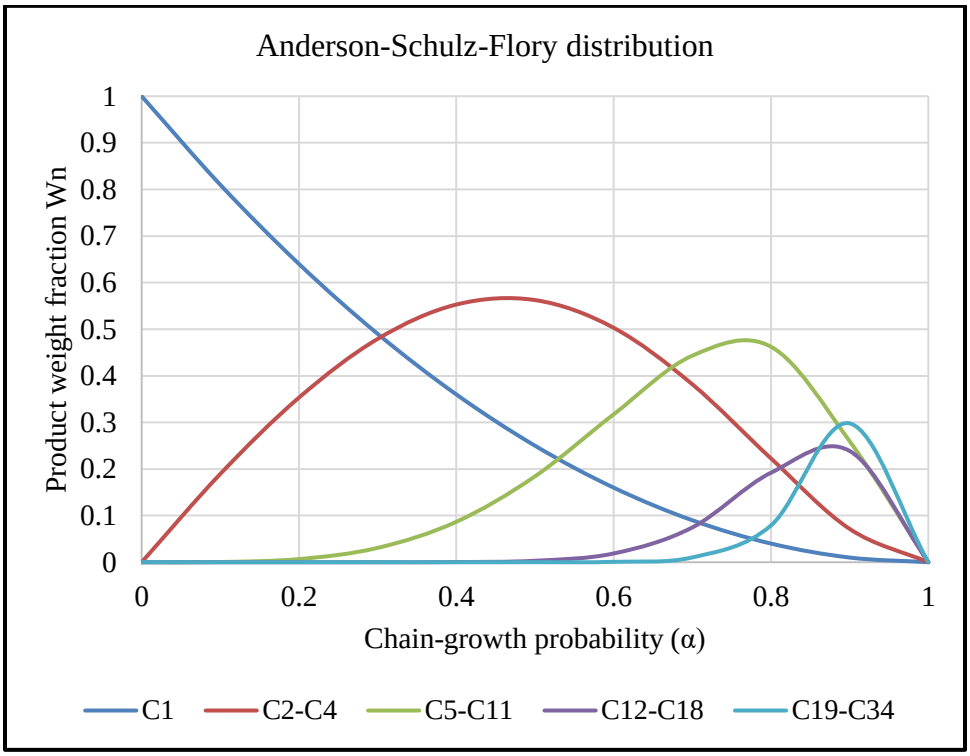

Figure 1.3: Product distribution of FTS function of chain growth probability

Deviation from ASF has been observed experimentally in many FTS catalysts; thus ASF alone cannot describe all fractions of hydrocarbon products. This is attributed to the different activity and reaction mechanisms of each catalyst. For instance, CH_4 does not follow the ASF relationship and forms from different routes resulting in high selectivity of CH_4 [42-43]. In many studies, a bi-model was suggested, so that two values of chain-growth probabilities (α_1 and α_2) can be computed and superimposed to predict hydrocarbon distribution with more accuracy. Nevertheless, modeling of hydrocarbon distribution in FTS is still a challenge with a complexity in interrelationships between various FT factors [16].

Undesired hydrocarbon products in FTS remain one of the main challenges for researchers. More understanding of the reaction mechanism will improve FTS performance and as a result, the desired hydrocarbon selectivity will increase. For instance, the high selectivity of methane and low moleuclar-weight hydrocarbon products are an indication of high hydrogenation rate and usually associate with an increase in exothermicity in the reaction. Therefore, removing any excess heat and controlling the reaction temperature would be a great contribution to the FT reactor design and operating conditions. Another undesired product is CO_2, which is catalyst-dpendent and produced via water-gas shift reaction. In this reaction, the production of H_2 and consumption of CO play major roles in CO/H_2 adjustment in coal to liquid (CTL) process, due to the H_2-deficiency in coal-based syngas. This would be different in the gas to liquid (GTL) process, where H_2 is rich and Co-based catalyst is favored for its high reaction performance and high yield of long-chain hydrocarbons [44].

1.3 Catalysts for Fischer-Tropsch Synthesis

Before discussing the role of catalysts in FT synthesis and its impact on energy and industry sectors, it is worth mentioning the choice of the FT process itself. This choice is based on the industrial and energy-related demands for chemicals and liquid fuels. According to aforementioned mechanisms, the hydrogenation rate during the chain-growth propagation step plays an important role in hydrocarbon products selectivity. However, the hydrogenation rate is highly affected by reaction conditions and catalysts. Commercial utilization of FTS is conducted in two modes of conditions: high-temperature Fischer-Tropsch (HTFT) and low-temperature Fischer-Tropsch (LTFT). Each mode is aimed at different desired hydrocarbon products [45].

In LTFT, the operation temperature of the reaction is in the range of 220-250 ºC and is mostly conducted in the slurry reactor to increase its efficiency. Both Fe and Co are used, but at different temperatures. In this range of temperatures, FT products are aimed for paraffinic high molecular-weight hydrocarbons. Thus, the low temperature leads to less selectivity of unwanted low molecular-weight hydrocarbons due to the relatively low hydrogenation rate. In LTFT, the hydrogenation of adsorbed CO on the surface's active site is high enogh to conduct further chain-growth propagation, consequently the high molecular-weight hydrocarbon products selectvity would increase, and low molecular-weight hydrocarbon product would decrease. Any increase in the reaction temperature would have an effect on the hydrogenation rate, which then results in a high termination rate. Therefore, the reaction would be more selective toward low molecular-weight hydrocarbons [46-47].

On the other side, HTFT operates at high temperatures up to 350 ºC, aiming for gasoline and light alkene products. Hydrocarbons in HTFT are more branched, which increase gasoline's octane number. Light alkenes can be oligomerized to produce diesel with a conventional cetane number due to the high branched content of HTFT [48]. In contrast, LTFT produces diesel with a cetane number that is remarkably higher than oil-derived diesel, but its yield in most cases does not exceed 18% of the total product. However, the diesel production in LTFT can be boosted up by a further process of hydrocracking of wax. The high cetane-number diesel yield can then reach up to 60% of the total products.

Light naphtha in LTFT can be produced in a considerable amount with high paraffin contents. However, it is very suitable for high-yield ethylene production [49]. The HTFT process is the best choice for gasoline production at high CO convesion. Moreover, Fe-based catalysts at the conditions of HTFT produce more alkenes in low molecular-weight hydrocarbons, but the oxygenates are less selective in the LTFT mode. Further processing of these alkenes in oligomerization increases gasoline yield over non-selective acid catalysts, followed by the hydrogenation process to improve gasoline quality. Table 1.1 shows the typical FT products distribution for iron catalyst for both HTFT and LTFT and cobalt catalyst for LTFT process [50-51].

Table 1.1: Typical hydrocarbons distribution for LTFT and HTFT

	Co LTFT at 220ºC	Fe LTFT at 235ºC	Fe HTFT at 340ºC
C_1	4	3	8
C_2-C_4	8	8.5	30
C_{5+}	87	84.5	57
Oxygenates	1	4	5

Chemicals for industrial use are an additional target in commercial FT plants, such as polyethylene, polypropylene, polyvinyl chloride and acrylonitrile production. Oligomerization of ethylene for polyethylene production requires light hydrocarbons alkenes which can be produced in large amounts based on catalysts and conditions of the reaction. Moreover, linear alcohols in C_{10}-C_{14} are one of the desired products that FT is able to supply with an easy separation from other hydrocarbons, due to the higher boiling point of alcohols compared to alkanes and alkenes [52-54].

From the previous overview of FT's role in energy and chemical industry sectors, its noted that the catalysts play key roles in the FTS purpose and use. Therefore, an efficient design of catalysts would significantly affect the hydrocarbon distribution and consequently determine the specific use of FTS. FTS can produce mainly gasoline, diesel, wax or chemicals. What determines the selectivity of FTS products are the mechanisms of chain-growth propagation, degree of hydrogenation rate, and readsorption rate of olyefins [38]. Since FT's discovery in 1926, only iron and cobalt have been used commercially to catalyze CO hydrogenation, due to their capability of adsorbing and hydrogenating CO to produce a wide range of hydrocarbons. In fact, Ru performs this reaction with the best activity at a lower temperature (~150 ºC) with the maximum selectivity of high molecular-weight hydrocarbon, but the scarcity and high price of Ru limits its commercial use in FT process. Ni is also a very active catalyst for FTS, but forming Ni-carbonyl at FT realistic reaction conditions redirects product selectivity to low moelcular-weight hydrocarbons and mostly methane is produced. The high methanation rate is attributed to the high hydrogenation rate of Ni-carbonyl [44], [55] & [56].

Activity of Co and Fe have been explored and it is concluded that Co has activity 3 times more than Fe in LTFT reaction conditions. Fe has more activity at HTFT conditions, but stability of Co was superior compared to Fe and exhibited a lifetime 250 times longetr than Fe. This might be ascribed to the high resistance of Co to the high partial pressure of water observed at low or high reaction pressure, temperature and space velocity. High dispersion of Co nanoparticles supported by oxides is the major key catalyst-design target in order to efficiently utilize the expensive transition metal and increase its volumetric productivity to mitigate the high exothermic effects of CO hydrogenation reaction [38]. Accordingly, maintaining high nanoparticles dispersion on supported catalyst would result in a high density of active sites and an increase in catalyst activity.

However, such high dispersion of cobalt nanoparticles in contact with high surface area oxide supports (SiO_2, TiO_2, or Al_2O_3) was reported to increase strong metal support interaction (SMSI), thus, a cobalt-support complex is formed during synthesis and pretreatment procedures. In addition, Co activity and hydrocarbon selectivity are strongly diminished by nanoparticle sizes smaller than about 6-8 nm, while nanoparticles bigger than 6-8 nm have no influence on FT activity or selectivity [57-60]. This effect of the metal-support interaction was attributed to the decrease in the number active sites in the small nanoparticles that are specifically active for long-chain propagation reaction. Therefore, the increase in methane selectivity and decrease in C_{5+} selectivity were observed for catalysts with the small nanoparticles size, which posses high hydrogenation rate leading to an inhibition in long-chain propagation and re-adsorption of α-olyfins reactions as they are necassry for the long chain hydrocarbons selectivity to be high [61-62].

The correlation between Co particle size and extent of reduction was recorded in Jacob et al. when non-reducible metals were added to Co and resulted in shifting the reduction temperatures toward high temperature due to a decrease in Co nanoparticle size [63]. Another factor that has been studied to investigate the decrease in Co activity is the transition of Co^0 to Co_2C after a prolonged time on stream reaction, which was reported as a deactivation mechanism. Though the Co_2C phase might have no activity for CO hydrogenation, the transition of Co^0 to Co_2C after long exposure to CO and H_2 at the reaction condiction to Co (hcp) was reported. The high ratio of hcp/fcc in Co^0 phase demonstrated higher activity and more stability compared to fcc-rich Co^0 phase [64].

Commercial use of Fe catalyst is attractive due to its cheap price compared to Co, but low intrinsic activity of Fe-based catalyst compared to Co is a disadvantage. However, if high active site density of Fe could be synthesized to improve FT reaction performance, then it could be comparable to Co-based catalysts activity. Fe-based catalyst have high activity of WGS reaction along with CO hydrogenation reaction, thus it is more tolerant to the H_2/CO feed ratio. However, Fe-based catalyst might be activated for more than one purpose of FT reactions, therefore, each reaction condition would increase the selection of specific desired range of hydrocarbons. Although Fe-based catalyst is more flexible to the operation conditions and purpose of utilization, the attrition of catalysts activity is faster compared to Co-catalysts and transition of Fe-oxide species to Fe metal and carbides species is uncetain. Different Fe-oxides and Fe-carbides can co-exist in the FT reaction environment. There is controversy regarding which Fe species is active for CO hydrogenation reaction [65-67].

Therefore, understanding the transitions between different Fe species would give a deep insight on how to design Fe-based catalyst that is active for CO hydrogenation reaction and improve FTS performance as it might be comparable with Co-based catalyst's performance in FTS. It has been observed that certain Fe species are rich in the small nanoparticles, therefore it could be concluded that the transformation between various Fe species is particle-size dependent. However. α-Fe, Fe^{2+}, and magnetite Fe_2O_3 were observed in Fe-based catalysts after pretreatment in H_2, while other species such as χ-Fe_5C_2 was detected as a dominant phase that formed during FT reaction. Other Fe-carbide species Fe_xC have been considered as active sites for CO hydrogenation reaction and each one has different products selectivity and this is dependent on nanoparticle size. This is an indication that the Fe metal phase is not stable during FT reaction and would transform into other species such as Fe-carbides. This transformation might be induced by relatively low activation of the Fe metal sepcies into Fe-carbides which is expected to be lower than the activation of CO adsorption and hydrogenation of intermediates [68-69].

Both Co and Fe catalysts are widely used in commercial FT reactors based on desired product slate and feedstock availability. It should be noted that the reaction mechanism is different for each transition metal catalyst. Although some mechanisms are still not understood, it is commonly accepted that the CO adsorption is dissociative on Co while it is not on Fe. Both catalysts might be improved by the rational synthesis of promoted catalysts for improving the yields of desired products. That is the goal of this thesis.

1.4 Fischer-Tropsch supported-metal catalysts syntheses

1.4.1 Supported Co-based catalysts

Transition metals that have been used in the FT reaction are in most cases supported by oxides such SiO_2, Al_2O_3 and TiO_2. Therefore, mechanical strength, high dispersion, high active site density, and more stability would be provided. Supported Co catalysts have been used since FT was discovered and commercialized in the 1930s. Since then, research groups have been studying the activity of Co and correlated that to its structure, the effect of support, synthesis, type of precursors, and pretreatment conditions influences [38].

The effects on activity and hydrocarbon selectivity of the interaction of Co with support has shown an inverse relation with Co particle size below 6-8 nm, while Co activity is not particle size-dependent with particles greater than 6-8 nm as shown by Iglesia et al., when active site time yield is independent of Co particle size for large nanoparticles [70]. For Co particles smaller than 6-8 nm, den Breejen et al. and Bezemer et al. demonstrated the diminishment of the intrinsic Co active site activity with decreasing Co particle size. There is a consensus on the optimum size (6-8 nm) of Co nanoparticles that can accommodate a maximum active site density with the highest turnover frequencies (TOF) of cobalt [60] & [71].

The extent of reduction, which is very low in small nanoparticles, is strongly affected by metal-support interaction. This interference with Co reducibility was ascribed to the formation of Co-support species, which have shown no activity for CO hydrogenation reaction [72].

The effect of support texture, surface, and porosity in Co-based catalysts have been a focus of study for many research groups to investigate support effects on Co reduction, FT activity, and hydrocarbon products selectivity. The effect of the pore size of mesoporous silica on the size of Co_3O_4 nanoparticles has been studied by Khodakov et al., by which the Co_3O_4 nanoparticles' size is proportional to the pore size of the mesoporous silica support. However, it has been concluded that the formation of Co_3O_4 is preferential inside the pores of the silica support, which means the support pore size has pronounced effects on Co dispersion more than weight loading [61].

This variance of Co dispersion based on silica pore size showed different extents of reduction of Co_3O_4. Thus, the smaller Co_3O_4 nanoparticles in a small pore size of silica reduce to the least extent, while the bigger CO_3O_4 nanoparticles that formed in larger pore sizes showed a higher extent of reduction. This was observed by XANES spectra shift of CoO to the Co^0 metallic phase, which was higher for small Co_3O_4 nanoparticles. The small Co_3O_4 nanoparticles showed lower activity compared to the big nanoparticles, and thus this phenomenon was attributed to the low extent of reduction of Co_3O_4 nanoparticles in narrow pores of silica.

Another effect observed with small Co_3O_4 nanoparticles was the formation of a mixed metal-support complex that is hard to reduce. As a result, fewer Co active sites required for CO adsorption and hydrogenation will be available. Moreover, the contribution of Si ions in small Co_3O_4 nanoparticles is ascribed to the increase in the metal-support interaction, consequently, a reduction on the activity of Co will be a major drawback on the FT reaction performance [73-75].

In strong Co-support interactions, a high-temperature reduction is required to transform Co_3O_4 and CoO species to the Co metal phase. This high-temperature of pretreatment would induce sintering of nanoparticles, resulting in a reduction in cobalt active site density and a decrease in the efficient use of expensive metals. The reduction of many supported cobalt-based catalysts has been studied to investigate the effect of reduction temperature on Co structure. Co (hcp) showed more stability and activity under FT synthesis conditions than the Co (fcc) structure, which was attributed to similar stacking sequences between Co (hcp) and Co_2C. Thus, a low reduction temperature is preferential for forming the more active and stable Co structure (hcp) [76]. However, forming the (hcp) structure of the Co metal phase is not a straightforward process and it is influenced by many factors such as Co precursor, drying process, calcination temperature, and presence of promoters.

In fact, metal-support interaction is lowest with SiO_2 and highest with TiO_2 and Al_2O_3; therefore, the weaker interaction would mostly lead to the formation of larger nanoparticles of Co_2O_3 [22-25]. Accordingly, the reduction of the supported Co catalyst plays an important role in the FT catalyst activity. There is a tradeoff between Co dispersion and its extent of reduction, which is affected by Co-support interaction. That can be optimized by modifying cobalt-support interaction or enhancing the reducibility of Co_3O_4 [77-79].

In Co-based catalysts for FTS, the main catalyst design challenges are to maximize Co active site density, minimize Co-support interaction, and increase the extent of reduction. Therefore, the efficient and rational synthesis of Co is considered as the key catalytic design factor by which an efficient use of Co would be achieved.

1.4.2 Supported Fe-based catalysts

In FT history, iron-based catalysts were the first commercial use of CO hydrogenation reaction and were used mostly in coal-based syngas conversion to hydrocarbons, “coal-to-liquids” or CTL. The purpose was to produce gasoline and diesel liquid fuels from coal, and FTS was run at a low temperature. Since then, researchers have focused on promoting Fe catalysts and modifying the support to be mechanically stable, because the CO hydrogenation was conducted in slurry reactors, and a wide pore support was required to allow the diffusion of high molecular-weight hydrocarbons. The other industrial purpose of Fe-based catalysts is to produce low molecular-weight olefinic hydrocarbons, where the FT reaction is conducted at high-temperature (HTFT). For this process, small pore diameter with low porosity support is favorable [66] & [80].

The pretreatment procedure is an important step in the activation process for Fe-based catalysts; the catalyst can be treated in H_2, CO or syngas. This facilitates the formation of an active phase of Fe or Fe-carbide from Fe-oxides. There are many forms of Fe-oxides, Fe metal phases, and Fe-carbides. Therefore, the pretreatment of Fe-based catalysts is critical, and structural change during this process is still unclear [81-82].

Fe-based catalysts are more vulnerable to deactivation during the FT reaction compared to Co-based catalysts, and that is attributed to the high rate of WGS reaction, which is a characteristic side reaction of Fe, along with CO hydrogenation. This is indicative of re-oxidation of Fe-carbides and that was detected by Li et al. using X-ray Absorption Spectroscopy (XPS), but the mechanism of transition still is unclear [83].

The effect of the particle size of Fe on catalysts' activity is not certain and still under debate. Large nanoparticles of Fe were discovered by Boudart and McDonald to be more active [84], but more selective to methane and less to C_{5+} with a high rate of deactivation compared to small nanoparticles. Barkhuizen et al. also observed the low activity of small nanoparticles compared to large nanoparticles of Fe, which was attributed to the higher oxidation rate of small nanoparticles of Fe and the transition of small nanoparticles of Fe-carbides to magnetite [84-85].

The removal of a catalyst bed exotherms is the main key in Fe-catalyst FTS reactor design. For the catalyst itself, high dispersion of Fe nanoparticles is an important target, but particle size dependence and the deactivation mechanism of the active Fe metal phase are uncertain. The Fe nanoparticle structure showed high sensitivity to particle size, gas partial pressure, texture of support, and reaction conditions. Therefore, most studies have focused on the stabilization of the active phase of Fe nanoparticles during the FT reaction and how to maintain high dispersion of the active phase [86-88].

Iron catalysts can be stabilized during the FT reaction by either adding promoters or modifying the support due to the high structure sensitivity of Fe nanoparticles. WGS reaction activity is another reaction that also can be influenced by Fe particles size, reaction conditions, and stability of catalysts. This activity also would have some effects on catalyst deactivation and products selectivity such as oxygenates and CO_2. Many studies agreed that the Fe zero valent state is not the active phase for FTS and, that was detected by observing the construction of Fe-carbides in several stages of Fe catalysts during the FT reaction, but no activity or product selectivity changes were observed [89].

1.5 Synthesis of Catalysts

1.5.1 Overview of Catalysis

Today many disciplines such as chemical, biological and environmental science and engineering have found that their applications are strongly dependent on chemical reactions, kinetics and catalysis. Catalysts play a pivotal role in our lives and contribute significantly in the chemical industry and energy sectors. The three-way catalyst is perhaps the best example of the efficient use of catalysts in the reduction of pollution of the environment and the development of the ammonia synthesis process is perhaps the best historical example of catalysis serving global agriculture and world's population growth. Currently, the interdisciplinary nature of catalysts led to their extensive use in many disciplines, and account for more than 20% of the U.S. gross national product. The applications of catalysis have grown rapidly over the last 70 years, and the need for catalysts to be more selective toward desired products and improve their lifetime are the most interesting topics, but development in this field still does not meet disciplines' needs [90].

In many applications, the use of catalysts requires precious metals such as ruthenium, platinum, palladium, and rhodium in different reaction conditions. However, catalysts might deactivate during reaction, thus reducing catalysts' lifetime, which requires a treatment to regenerate catalyst activity. There are many modes of catalyst deactivation such as metal nanoparticle sintering, decoration, or restructuring, which make the regeneration process infeasible or costly.

As a heart of the chemical industry, catalysis is a core field of science that is facing fundamental and commercial challenges, and innovation in this field is key development to the world economy and standard of living. Therefore, many scientists and researchers have been focusing on understanding the fundamentals of designing catalysts that improve sustainability and meet growing product demand. Advances are needed in catalytic processes in numerous applications and sectors.

Catalysts are classified by the media of catalysts, reactants, reaction intermediates, and products. Accordingly, catalysts and reactants either coexist in one homogeneous phase, which are known as homogeneous catalysts, or each one exists in a different phase such as solid catalysts with reactants in the gas phase. In some cases, multi-phase reaction, solid, liquid and gas, are all involved in a catalytic reaction. The homogenous catalytic reaction is characterized by high conversion and high ability to control the desired product's selectivity, but it is strongly affected by the reaction temperature and low thermal stability, and it adds significant cost for the separation of catalysts from reaction media. While heterogeneous catalysts can be more thermally stable and have strong mechanical properties, which enable catalysts to actively work at extreme reaction conditions, weak control on product selectivity is the main challenge in heterogeneous catalysts. The sintering of precious metal nanoparticles is caused by the agglomeration of metal nanoparticles at high temperatures. Another important catalyst design consideration that would reduce catalyst functionality is the loss of active sites caused by the decoration of non-active materials blocking active sites or strong metal-support interaction [91].

The significant role of catalysts to face increasing challenges in energy, economy, and environment has increased their importance which has been a motivation to innovate

a rational design in catalysis by using powerful characterizations techniques to understand their fundamentals, structure-function, reaction kinetics and mechanisms in order of facilitate catalysts' activity and control products selectivity. In our study, we will focus on preparation method and characterization of heterogeneous catalysts, therefore, this overview will be more oriented to heterogeneous catalysts.

Industrially, the heterogeneous catalyst is favored in many applications due to its ability to functionalize chemicals, such as in selective hydrogenation, oxidation, and redox processes which are widely used in environmental protection and green chemistry applications. Another interesting and promising use of the heterogeneous catalyst is the dehydrogenation of alkanes to produce alkenes, which are valuable chemical feedstocks, and the epoxidation of alkenes, which is still a challenging reaction for higher alkenes.

Other challenging reactions of interest are the oxidation of a C-H bond to form alcohols, where catalysts should be designed to have the ability to break the selective C-H bond in longer chain hydrocarbons, hydrogenation of oxygen to produce hydrogen peroxide, and direct oxidation of ethane to acetic acid. Some chemical reactions are kinetically and thermodynamically hard to conduct, and the heterogeneous catalyst would provide multi-functions to address these challenges. However, these reactions require severe reaction conditions; therefore, it would be highly beneficial and cost-effective to consider these effects in heterogeneous catalyst design and synthesis [92].

The goal of commercially manufacturing heterogeneous catalysts is to design a catalyst with high active site density to efficiently maximize the use of active metal atoms, instead of being wasted inside the bulk of a metal particle. The term metal dispersion,

defined as the fraction of metal atoms at the active surface divided by the total number of atoms, is a key metric of metal atoms' availability for the catalytic reaction. High dispersion is normally preferred.

Dispersion can be measured with various techniques such as gas chemisorption, in which the analytic gas molecule is chemically adsorbed at a known stoichiometry to the active metal sites. This allows the number of accessible active sites to be titrated. A constructive interference of monochromatic X-rays in XRD is another technique that can measure the size of metal nanoparticles. The XRD measurement is usually coupled with an analysis of images obtained by electron microscopy (EM) [93].

In heterogeneous catalyst characterizations, more techniques are usually preferred to characterize the metal nanoparticles facets, structure and geometry to determine precisely the number of active sites and to sort their functions according to their coordination. It has been recognized for more than 85 years in the field of heterogeneous catalysis that particles size has a great influence on activity and selectivity. This remarkable influence of particle size on catalysts activity is expressed in turnover frequency (TOF), which is the rate of reaction in moles per number of active sites that are accessible to reactant molecules per unit time. This parameter is another important metric in heterogeneous catalyst performance.

The correlation of TOF with respect to particle size can describe how sensitive the metal nanoparticles' structure is to the reaction activity. For insensitive structures, TOF does not change with varying metal nanoparticle size, while sensitive structures have particle size dependency for TOF. The cause of particle size dependence can be

investigated by studying electronic, structural, and adsorption characteristics of metal clusters. The geometrical properties are not simple to be determined, and that is attributed to the non-uniformity of nanoparticles, the different type of active sites with different functionalities, and the presence of defects on metal nanoparticles' surfaces. Therefore, the nanoparticle size effect is not straightforward to study, and that has led researchers to observe the effect of crystal facets whose ratios depend on particle size, but mostly for a range of size < 10 nm. However, this difference between properties of particle size less than 10 nm and bulk crystals has been a hot research interest, and this transition in particle size has various effects on the crystal's structural and electronic properties [94].

High surface area oxides mechanically support and facilitate a high dispersion of metal particles and help stabilize the nanometer-size crystals, which can have various crystal faces ratios and create a high density of unsaturated coordination sites that are active for the chemisorption of reactant molecules and intermediates. The support might be inert for the reaction or have some contributions such as adsorbing hydrogen followed by migration process of H_2 to metal nanoparticles, which is known as spillover mechanism, or create interaction with metal nanoparticles. In some systems, the strong interaction between metal nanoparticles and support is considered a major challenge in the catalysts' design and synthesis. Successfully designing catalysts with controlled particle size and optimum properties that have highly active and thermally stable is the overarching goal of research into catalyst preparation and pretreatment procedures.

The deposition of metal precursors onto a high surface area carrier is mostly conducted in aqueous media where dissolved metal precursors can easily diffuse and distribute over the carrier surface area. The drying process is the next procedure, which

evaporates most of the water from the support and leaves metal precursors anchored on the inner and outer pores of the support surface. These procedures can take place with or without interaction between the metal precursor and the functional group of support. Normally, incipient wetness or dry impregnation represents the adsorption of metal precursors without interaction with support. Any interaction between metal precursors and support can be classified according to the type of interaction, and the most common mechanisms are deposition-precipitation and ion exchange [95].

Metal oxide supports such as SiO_2, Al_2O_3, and TiO_2 are commonly used as catalyst supports. These highly porous, stable oxides anchor metal particles of nanometer size, exhibiting superior catalytic stability due to a monolayer of surface oxide that contains various functions of hydroxyl groups which are highly affected by the support. The hydroxyl groups play a great role in catalysts' synthesis, and it is worth mentioning that they can dictate electronic properties, acid/base support, and strength of interaction. In this chapter, the brief introduction of various catalysts syntheses will be presented to demonstrate synthesis's influence on the metal nanoparticle's physical and chemical properties and to show comparison with respect to our rational synthesis method "Strong Electrostatic Adsorption".

1.5.2 Impregnation

In the impregnation method, the active metal precursor is dissolved in a solution and then carrier support is mixed with the solution. The impregnation process can be classified according to the ratio of solution volume to the support's pore volume. Another classification of impregnation is related to the type of interaction between the support

surface and the dissolved metal precursor. According to the ratio of the solution volume to support pore volume, in excess solution's volume, the impregnation can be defined as a wet impregnation, soaking or dipping.

During contact between the active metal precursor and support, the diffusion of the metal precursor into porous support is dictated by the adsorption isotherm, the size and geometry of the carrier's pores, and the equilibrium concentration of the precursor in the solution. At short contact times, the mass transfer of the metal precursor into porous support controls the metal precursor's concentration inside the support's pores.

The interaction between the metal precursor and the support drive the mechanism of adsorption, which can be either chemical or physical adsorption. Hydrolysis of the surface, ion exchange, electrostatic adsorption, or ligand exchange could take place during this interaction process, which mostly occurs in an equilibrium condition.

On the other hand, the mass transfer and concentration of the metal precursor in the impregnation solution dictate the process of precipitation and crystallization during impregnation when there is no precursor-support interaction.

Accordingly, metal precursor-support interaction, diffusion of the precursors into support pores, and the concentration profile of the metal precursor are the major parameters that control the deposition and distribution of the active metal [96].

The other type of impregnation based on the ratio of the volume of solution to support pore volume is known as incipient wet impregnation, in which the active metal precursor solution volume is approximately equivalent to support-pore volume.

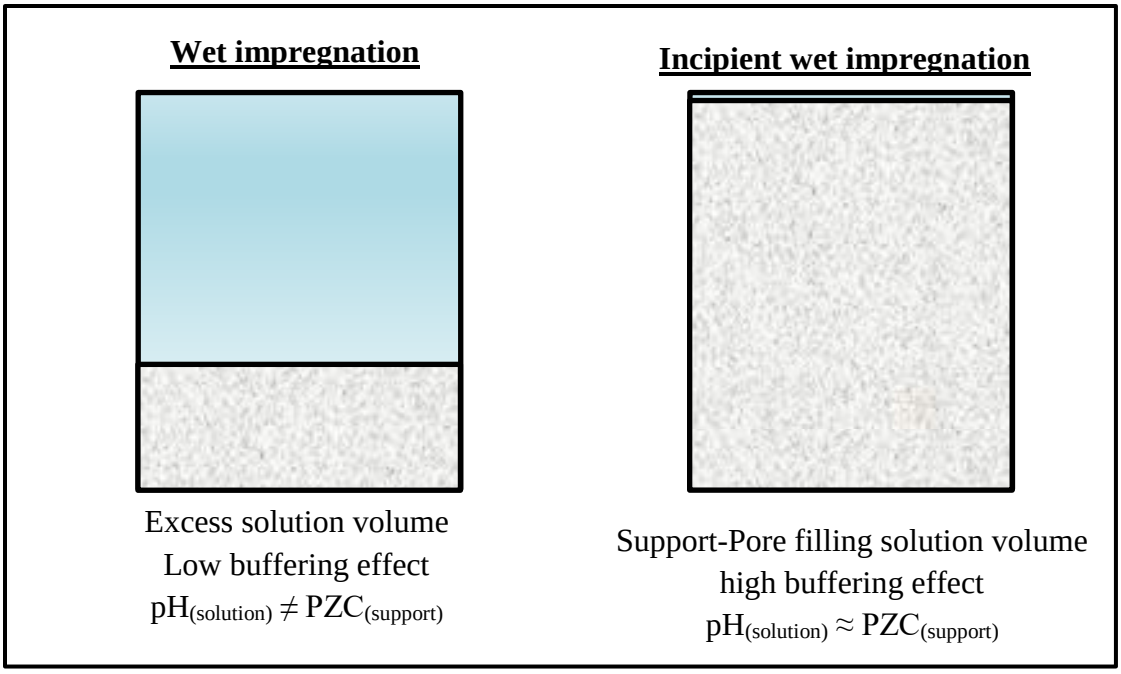

Figure 1.4: illustration of various impregnation techniques

In the absence of precursor-support interaction, the concentration and solubility of the metal precursor in solution control the weight loading of metal in the carrier support. However, increasing metal precursors concentration might have some effects on the pH of the solution.

Consequently, at extreme pH, this might lead to a deterioration of support. The inverse of the ratio of precursor-solution volume to support-pore volume can be defined as surface loading (SL) as shown in equation 7:

$$\mathrm{SL} = \frac{surface\ are\ of\ support\ \left(\frac{m^2}{g}\right) \times supportweight\ (g)}{metal\ precursor\ solution\ volume\ (L)} \qquad \text{(surface loading) (7)}$$

1.5.3 Deposition-precipitation

The metal dispersion after thermal treatment of catalysts is weakly controlled by impregnation method, and the metal weight loading can be controlled based on the metal precursor's solubility in the impregnation solution. The deposition-precipitation preparation procedure of catalysts can provide erlatively higher dispersion of the metal after thermal treatment. The key mechanism of this process is the gradual transformation of the dissolved precursor into an insoluble form through a chemical reaction. Gradual growing concentration of insoluble precursors results in nucleation, followed by precipitation and deposition of metal particles onto the support surface, forming a well-dispersed metal nanoparticle. The process of precursor nucleation is basically induced by adding a base agent such as NaOH (precipitation agent), which raises the pH of the solution. Thus, this increase in OH^- concentration consequently generates metal-hydroxide species.

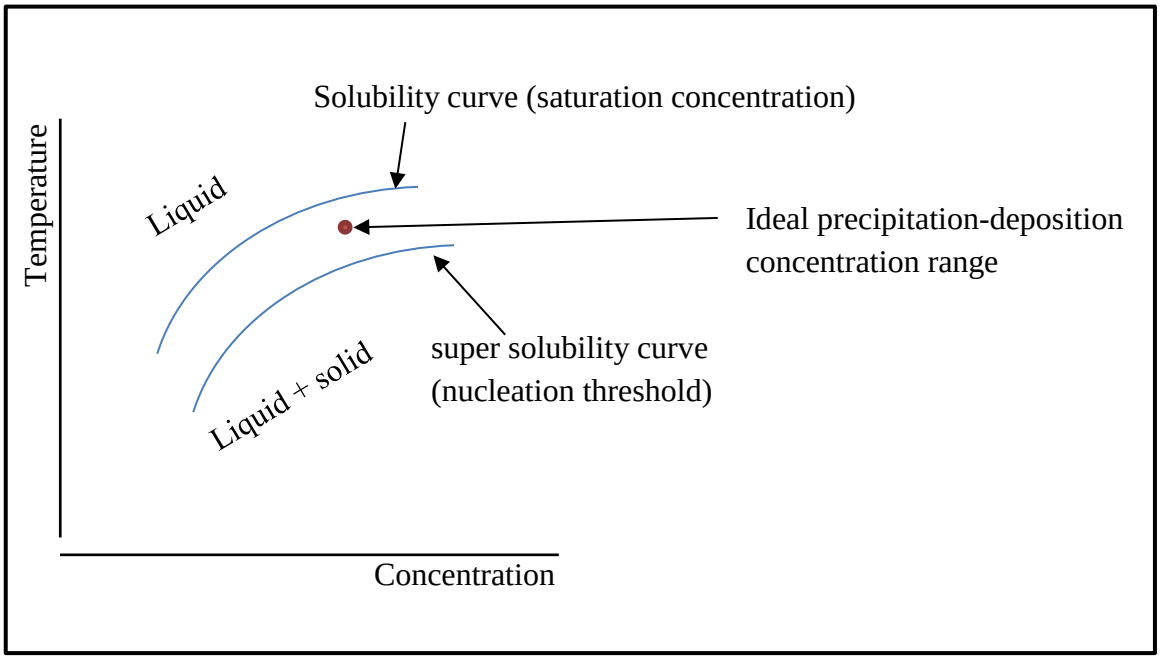

Figure 1.5: ideal concentration range for Precipitation-deposition process

The major challenge in the precipitation-deposition method is the pace of is the nucleation mechanism. As seen from Figure 1.5, the concentration of metal-hydroxide has to be located between the solubility curve, when the metal precursor concentration is saturated in solution, and the nucleation threshold or super-solubility curve. The mechanism can be controlled by the slow addition of a precipitation agent to the metal-precursor solution. Consequently, the preparation of nucleated metal precursors would occur selectively on the support. Therefore, this leads to a high dispersion of metal nanoparticles on the support; otherwise, a high nucleation rate will be extended to bulk solution, and large crystals and low metal dispersion would be the main consequences [97].

The addition of a precipitating agent is considered the limiting step, and can be conducted by various procedures. One of the most widely used methods is an injection of the precipitation agent with a special syringe below the surface of the liquid. High efficient mixing is required for a rapid distribution of the precipitation agent; then homogeneity of mixing and precipitation of nucleated metal can occur. But this is not a straightforward method, and efficient mixing by agitation in large scale cannot be achieved. Another factor that can improve metal dispersion is the associated precursor-support strong interaction that can be established during the precipitation-deposition mechanism and induced by the chemical affinity between the metal precursor and the support surface. Therefore, it is important in a precipitation-deposition process that the support facilitate the nucleation of the metal precursor in solution close to its surface and in some cases create metal-support interaction. Redox is another advantage in the precipitation-deposition method, where reduced and oxidized metal precursors can be deposited, and that can occur by developing the metal precursor's oxidation state.

1.5.4 Strong Electrostatic Adsorption

The support oxides in wet or dry impregnation, where a suspended solid is in direct contact with the liquid solution, have demonstrated a pH-dependent surface charge that is governed by terminal hydroxyl ligand groups. This phenomenon has been studied by Noh and Schwarz by adding oxide to a liquid solution using the mass titration method to estimate the point of zero charge (PZC) [98]. The PZC is a critical parameter which is the pH at which the net surface charge is zero. The proton transfer reaction at hydroxyl groups would describe the surface charge. Accordingly, these hydroxyl groups can be protonated or deprotonated based on the pH of the solution. The surface will be positively charged when hydroxyl groups are protonated or negatively charged when hydroxyl groups are deprotonated. These reactions can be described by ionization reaction constants K_1 and K_2. Figure 1.6 depicts the mechanism of surface ionization reactions of the protonation and deprotonation of hydroxyl groups.

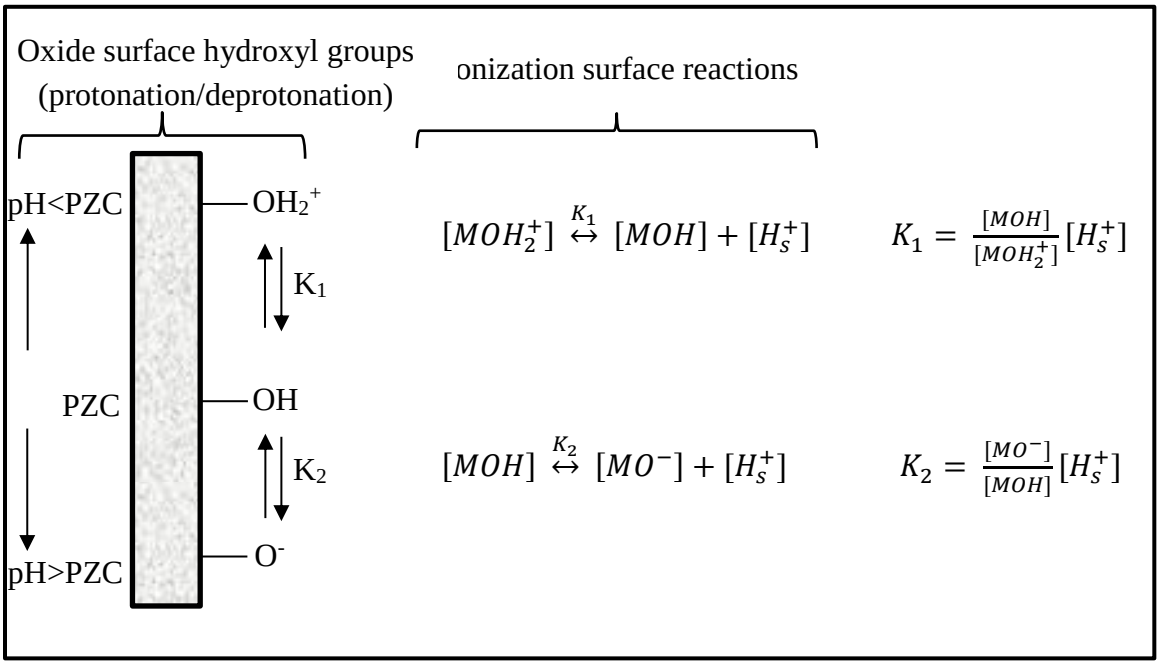

Figure 1.6: The regime of Strong Electrostatic Adsorption (SEA)

According to the protonation/deprotonation of the oxide's hydroxyl groups, the equilibrium of pH is usually achieved, and that depends on how much of the surface area is exposed to the solution. This is what has been mentioned in the previous section as surface loading, SL, surface loading (m_2/L). High SLs of oxide exert strong buffering on the solution pH. This is attributed to a high concentration of hydroxyl groups per volume of solution; their number exceeds hydroxide ions in the solution. In both cases, whether the solution pH < PZC or >PZC, high surface loading (high amount of oxide) leads to more proton transfer from or to surface hydroxyl groups. According to the number of hydroxyl groups available for ionization reaction, the resulting equivalent number of either $[H^+]$ or $[OH^-]$ in the solution would accumlate and represent the equilibrium pH of the surface. Accordingly, if more surface hydroxyl groups are in contact with a solution, it would lead to a wider range of initial pH of solution shifting to the same final pH [99]. This variation in pH shift curve is correlated with SL and can be shown in Figure 1.7.

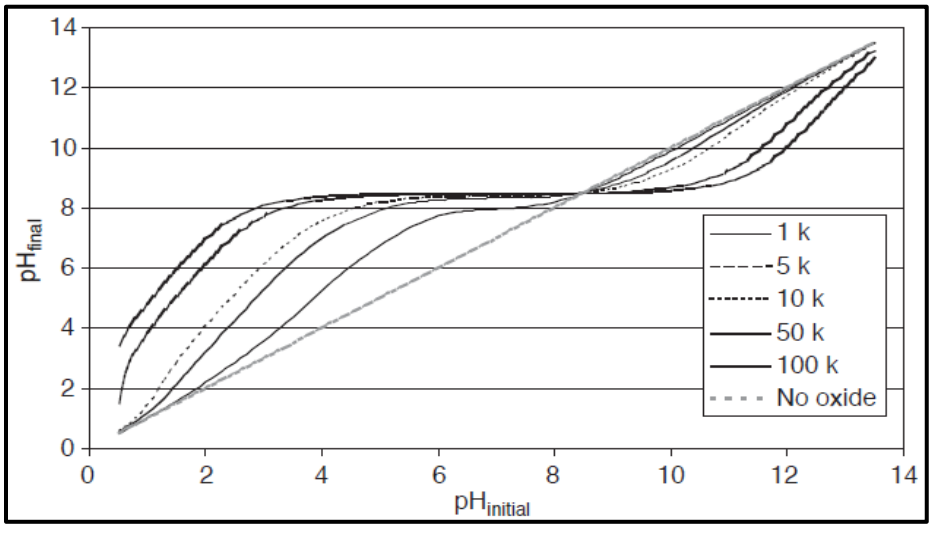

Figure 1.7: pH shift model simulation with varying surface loading for Alumina (PZC=8.5)

From Figure 1.7, the effect of surface loading is correlated with the pH shift curve's width; thus, at maximum surface loading, which is the condition of incipient wetness impregnation, the final pH plateau is equal the PZC of the support. This is one of the most used methods of measuring oxide PZC, which is called equilibrium pH at high oxide loading (EpHL) [99], by which a pH probe is used to measure final pH of high surface loading thick slurries. It is should be mentioned that the pH shift model and control experiments are conducted between the solid oxides and metal-free solutions and are aimed to determine oxide PZC.

Another key experiment that plays a major role in SEA synthesis is the metal uptake survey. The strong metal precursor adsorption profile can be investigated by an uptake survey experiment, by which a set of pH-adjusted metal complex solutions are in contact with a certain amount of oxide support according to a chosen SL. This uptake survey exhibits a volcano shape metal uptake that is pH dependent; therefore, the optimum pH can be determined by the final pH of the solution at maximum metal uptake.

Therefore, the oxides with low (acidic) PZC can build a negative charge on their surface during contact with a pH > PZC, as the hydroxyl groups will be deprotonated. Consequently, the cationic metal complex would be electrostatically adsorbed onto the surface. In a high PZC oxide surface, the low pH (pH < PZC) solution is in contact with the oxide. Therefore, a positive charge would accumulate and be built on the surface via protonation of hydroxyl groups, which would result in strong electrostatic adsorption between an anionic metal complex and the protonated hydroxyl groups of the oxide surface.

Basically, the uptake of the metal precursor is increasing when a solution pH moves away from the support's PZC, but this increase is retarded at the extreme pH of the solution, high acidic or high basic pH. This retardation in the metal precursor uptake is attributed to the ionic strength effect. Spieker and Regalbuto employed the Revised Physical Adsorption (RPA) model to predict the physical adsorption of anionic and cationic platinum complexes on γ-alumina [100]. Surface charge σ_0 and electric potential ψ are depicted in Figure 1.8 (a). Simple electric double layer theory is utilized in this RPA model; therefore, the driving force of the metal precursor adsorption is the surface potential. The electric potential of γ-alumina is retarded at the extreme pH of the solution.

Adsorption constants of the anionic chloroplatinate complex ($PtCl_6^{-2}$) and cationic platinum tetraammin complex [$(NH_3)_4Pt^{+2}$] are shown in Figure 1.8 (b) and predicted by RPA model. Both show retardation at the extreme pH of the solution.

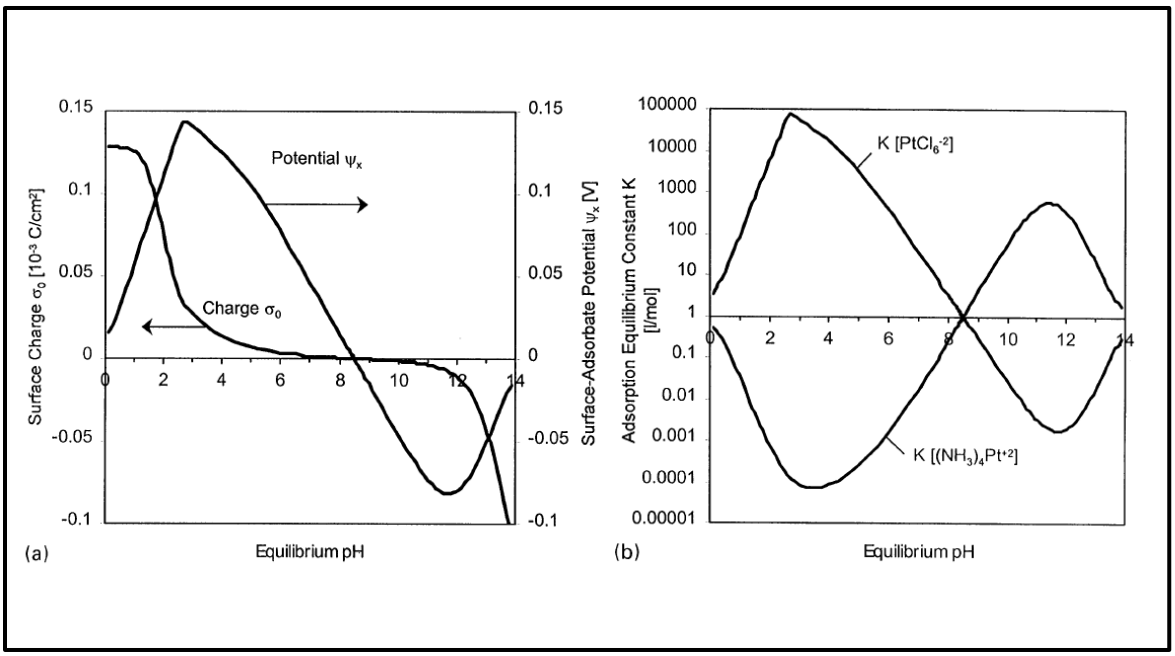

Figure 1.8: Charging condition and adsorption constants of the γ-alumina surface by RPA model

The adsorption of the anionic Pt complex is predicted to increase when the pH of the solution is below PZC, and RPA model predicts retardation will start from pH 2.5 and increase with lowering the solution's pH. The cationic Pt complex is predicted to increase adsorption at a high pH above PZC and start retarding at pH 11, and an increase in the retardation effect is predicted with an increase of the solution's pH. Figure 1.9 shows the predicted adsorption of Pt metal, anionic and cationic, complexes on γ-alumina.

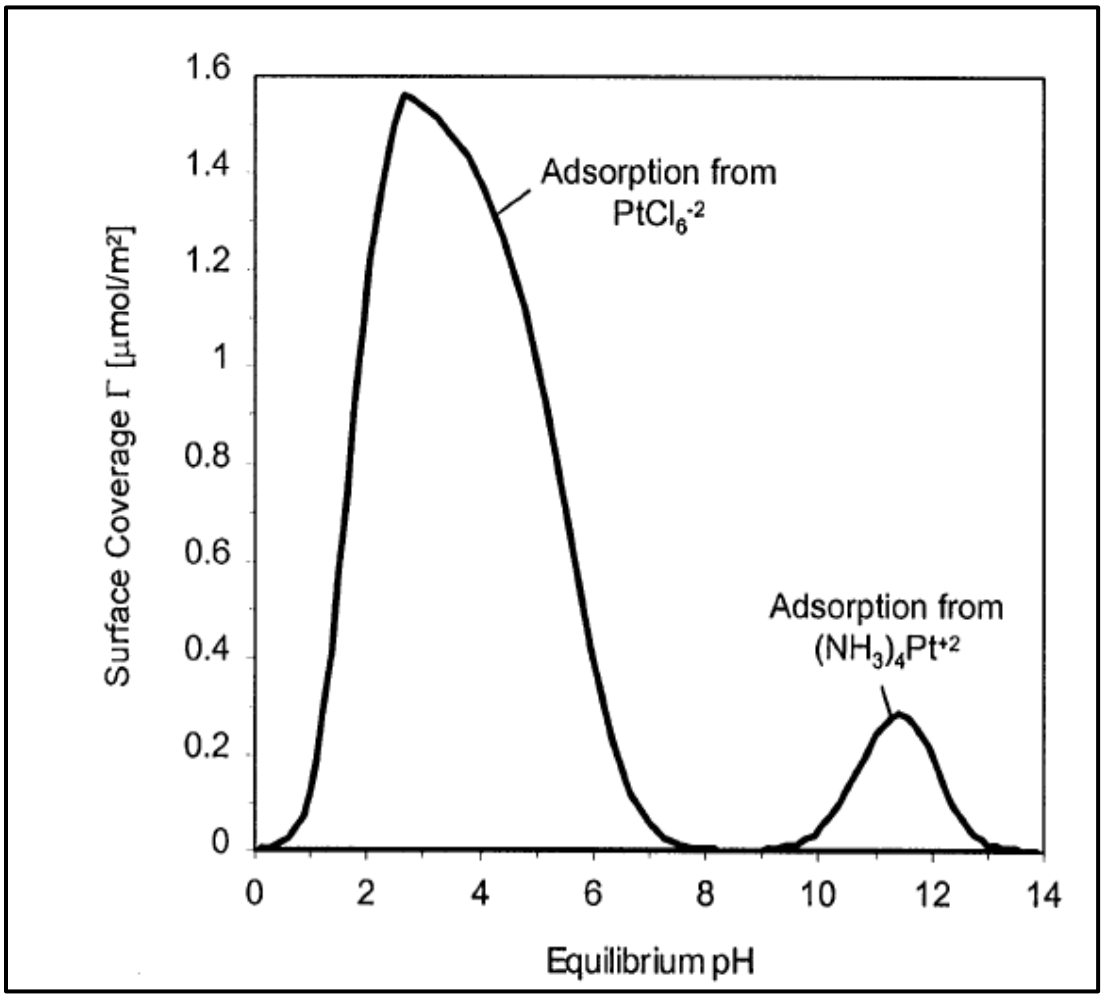

Figure 1.9: Anionic and cationic Pt complexes adsorption onto gamma-alumina

The high adsorption of the anionic Pt complex is attributed to the number of hydration sheaths which is expected to be one for the anionic metal complex and two for the cationic metal complex. The effect of the number of hydration sheaths on the maximum metal complex adsorption was proposed in collide science [101]. A low number of hydration sheaths that the metal complex retains would lead to a smaller area occupied by physically adsorbed metal complexes. It is commonly assumed that the maximum uptake of either anionic or cationic metal complexes is based on the close-packed monolayer. Thus, the steric of the anionic/cationic metal complex monolayer that either retains one- or two- hydration sheaths is playing a key role in the metal uptake onto the oxide's surface. Figure 1.10 depicts the adsorption of chloroplatinate [$PtCl_6$] complex onto terminal hydroxyl groups with 5OH/nm^2 and approximately one metal complex per nm^2.

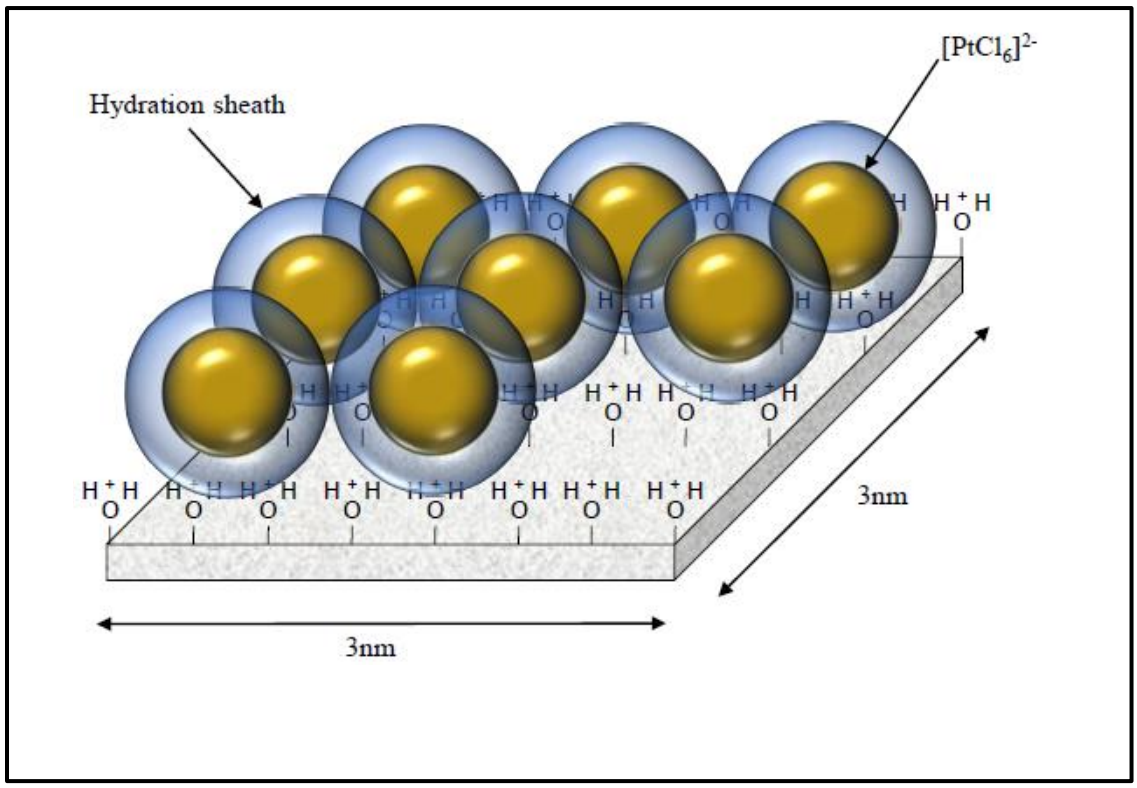

Figure 1.10:steric-close-packed adsorption of CPA retaining one hydration sheath

As mentioned before, these predictions of the metal uptake and PZC of supports are calculated by the RPA model. In this model, the Langmuir adsorption isotherm is employed representing the metal adsorption density on the surface and assuming the adsorbed metal complex is steric close-packed monolayer which is depicted in Figure 1.10. The key feature in the RPA model is that the Gibbs free energy adsorption is only dependent on coulombic term of adsorption; the other solvation and chemical free energies terms are eliminated. The additional revision was conducted for surface potential charge calculation of non-Nernstain description of the charge-potential relationship in the electric double layer. Therefore, the RPA model can predict cationic and anionic metal complexes' adsorption for different PZC oxides showing the trend of metal-uptake plateau width with the PZC of the oxides. In cationic uptake, further lowering the PZC toward an acidic pH would result in a broadening of plateau's width of the PTA complex adsorption curve. Increasing the PZC would further narrow the uptake curves and the complementary trend is predicted with anionic uptake on high PZC supports.

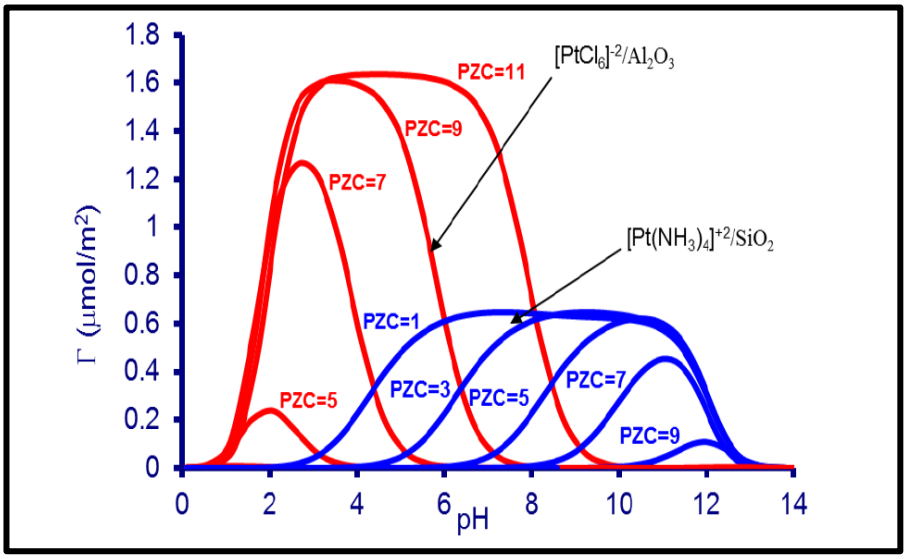

Figure 1.11: RPA-prediction curves of CPA and PTA complex based on PZC of oxides

SEA in catalyst preparation is considered as a simple and straightforward method that is extendable to many applications. It is hypothesized that a strong electrostatic force when the metal precursor solution is in contact with hydroxyl groups is sufficient enough for the adsorbed metal complexes to be bonded and stable with hydroxy terminals during drying and thermal treatment to form well-dispersed metal nanoparticles. Highly dispersed (particle size 1 nm) Pt/silica that was prepared by SEA had been verified using high-angle annular dark field imaging as shown in Figure 1.12 and confirmed by chemisorption [102]. This high dispersion of Pt nanoparticles also exhibited a narrow particle size distribution. The application of SEA can be used for the bimetallic catalysts' preparation and it is believed to improve ensemble, electronic, and synergetic effects.

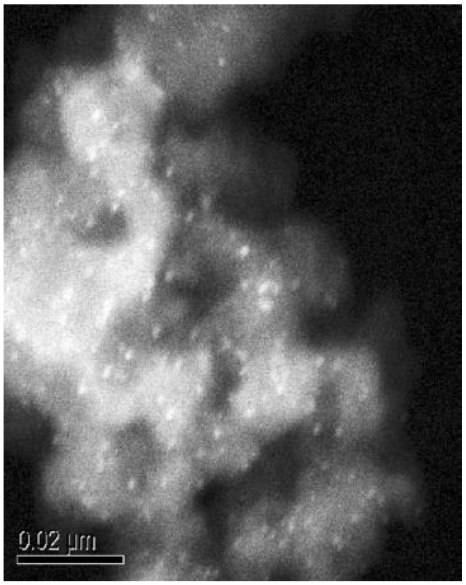

Figure 1.12: Electron microscopy characterization
of Pt/Silica catalysts prepared by SEA method

1.6 Dissertation layout

The main work of this study is the selective deposition of Pt onto Co_3O_4 and Fe_2O_3, which are supported by silica. The adsorption of Pt was conducted by the SEA method. The hypothesis of selective adsorption of Pt onto Co_3O_4 can be verified by observing Pt uptake on different surfaces of pure oxides and mixed oxides. Experiments of catalyst preparation and characterizations will be presented and discussed in Chapter 2.

The promotional effects of the selective deposition of Pt onto the cobalt oxide surface in the Co/SiO_2 catalyst will be discussed in Chapter 3 and compared to a bimetallic $Pt\text{-}Co/SiO_2$ catalyst prepared by the conventional method of co-impregnation. The catalytic reaction performance of Fischer-Tropsch was conducted for both sets of catalysts. The study of catalyst activity, hydrocarbon distribution, and olefin/paraffin ratio are presented with a comparison between the two sets of catalysts. This study is extended to Fe-based catalysts in Chapter 4.

CHAPTER 2

RATIONAL SYNTHESIS OF BIMETALLIC CATALYSTS: EXPERIMENTS AND CHARACTERIZATION

2.1 The hypothesis of rational deposition of platinum onto transition metal oxide surfaces.

In our study, the adsorption of noble metal Pt onto mixed oxides, which are either cobalt and silicon oxides or iron and silicon oxides, is hypothesized to be selective on each transition metal oxide (Co_3O_4 or Fe_2O_3).

That the adsorption of the Pt onto silica will be negligible is attributed to the difference in surface charge to achieve selective Pt adsorption. The key feature of our rational synthesis is that the silica has an acidic PZC while both transition metal oxides have PZCs higher than silica's. This means the surface charge profile of silica is different from transition metal oxides' charge profile.

Because of this difference in surface potential profiles of silica and transition metal, there is a sufficient gap that different charges exist over the surfaces of the support and either supported transition metal oxides when the composite materials are exposed to a solution at a pH between the PZCs of the components as depicted in Figure 2.1.

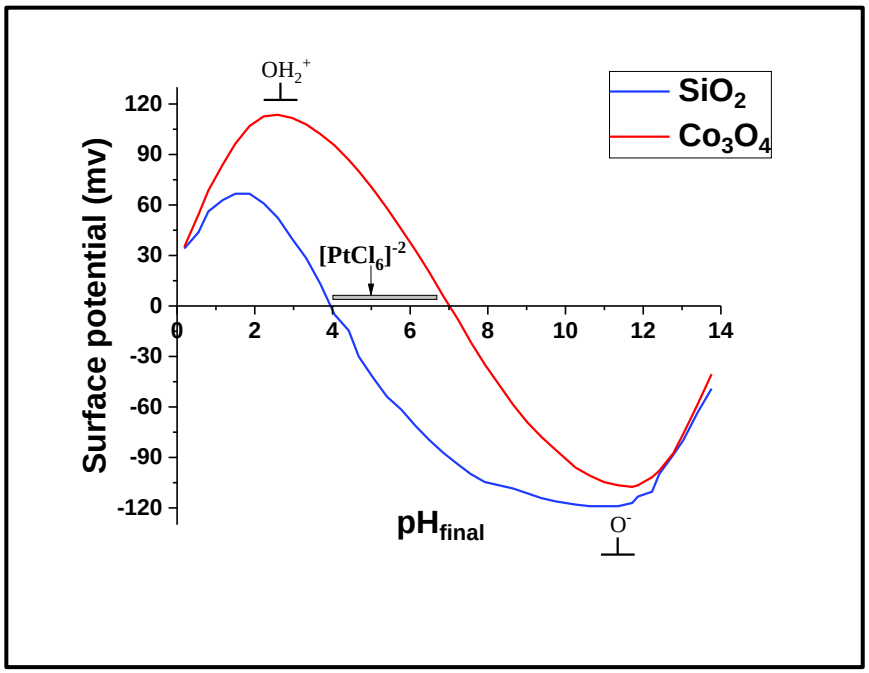

Figure 2.1: Schematic of the use of SEA based on the surface potential of Co_3O_4 and SiO_2

According to the difference in surface potential in Figure 2.1 for mixed oxides, the procedure of our synthesis would follow the next steps depicted in Figure 2.2:

1. Prepare weight 10% of a transition metal on SiO_2 using the incipient wetness impregnation method by preparing a solution of volume equivalent to the silica pore volume.
2. Mix the transition metal precursor and citric acid with equimolar ratio (1:1) in the solution. The citrate improves the metal dispersion [103-104].
3. Dry for 36 hours and thermally treat samples at 450ºC in the air to form nanoparticles of transition metal oxides on the SiO_2 surface .
4. Contact the prepared sample in a pH-adjusted $[PtCl_6]^{2-}$ solution at a specific surface loading, then shake, filter, and dry for 36 hours.
5. Thermally treat samples in H_2 at 600ºC or conduct the in situ reduction at 450ºC.

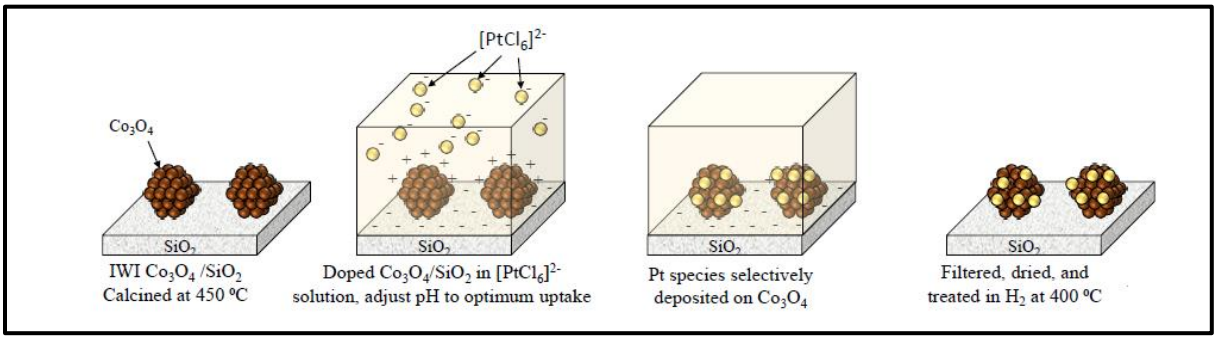

Figure 2.2: Pt-Co sequential preparations using IWI for Co/SiO_2 and SEA for Pt onto Co/SiO_2

These synthesis procedures were also followed for Fe/SiO_2. The only difference in the case of Fe/SiO_2 was that the air treatment was conducted at 275ºC. Other experiments were run to determine surface oxides' PZCs and the Pt uptake on each oxide, to verify the selective adsorption of Pt. Control pH-shift experiments were used to determine the PZC individually of each oxide - SiO_2, Fe_2O_3, and Co_3O_4. As each one has different PZCs and so differenct surface charging parameters, Pt adsorprion will be studied by Pt uptake as a function of pH on each oxide separately. In IWI-synthesis, the mixed oxides, Co_3O_4/SiO_2 and Fe_2O_3/SiO_2, will be contacted with CPA solutions to determine the optimum pH value at the maximum uptake of Pt for each aforementioned oxide. According to our hypothesis, the $[PtCl_6]^{2-}$ complex would be electrostatically adsorbed at a pH-solution that is below the silica's PZC when the surface oxide is positively charged. Therefore, the low PZC support would not have enough pH range to build a positive charge on its hydroxyl groups, and that is ascribed to high ion strength effects at a pH level close to the support's PZC. Finally, another set of co-impregnation Pt-Co and Pt-Fe are prepared for comparison.

2.2 Control experiements – PZC and Pt adsorption measurements.

Silica (Aerosil®300, average BET surface area ≈ 270 m^2/g) was obtained from Degussa to be used as an oxide support. In our study, first, we need to measure the point of zero charge of silica by weighing an appropriate amount of silica with three different surface loadings (SL), 1000, 10,000, and 30,000 m^2/L, using the equilibrium pH shift method. Series of pH solutions were prepared using NaOH or HCL to adjust the pH within a range of 2-13. Add the corresponding SL amount of silica to these series of adjusted-pH solutions and shake for an hour. Then the final pH for each solution was measured. Accoring to this, a plateau on the pH-shift curve (final pH vs. initial pH) represents the PZC of silica (see Figure 2.3).

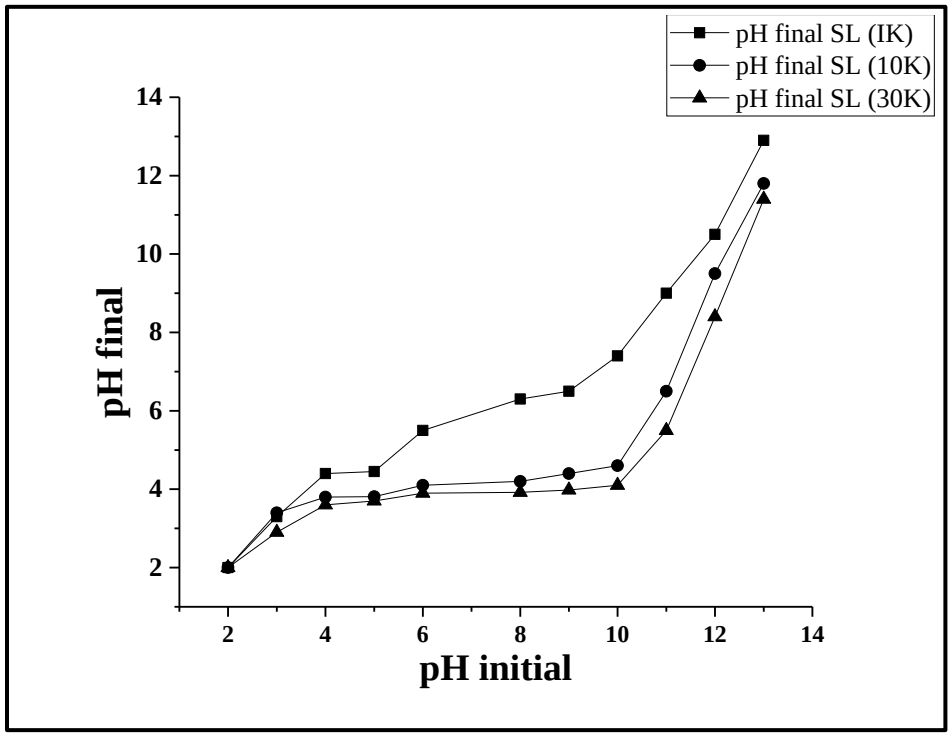

Figure 2.3: Control experiments of metal-free solution pH shift data for SiO_2 at different surface loading

According to our discussion in Chapter 1 regarding the prediction data of the pH shift model, in the real pH shift experiments, increasing the surface loading would broaden the plateau width.

Therefore, at a higher surface loading there is more surface area of silica. Consequently, the number of hydroxyl groups are more concentrated, which would increase the proton transfer between hydroxyl terminal groups and ions in solution. However, at a high surface loading, the equilibrium pH of the solution is more representative of PZC support due to the high buffering effect at a high surface loading of silica. The PZC of silica is represented by a plateau at the high surface loading which approaches 3.6, readily seen in Figure 2.3.

Pure Co_3O_4 and Fe_2O_3 oxides were prepared by thermal decomposition of $CoCO_3 \cdot xH_2O$ (Aldrich, 43-47%) calcined at 400ºC for 4 h, and calcination of $Fe(NO_3)_3 \cdot 9H_2O$(ALDRICH) at 275ºC for 5hr then washed by deionized water to eliminate nitrite on the surface. By using a special spear-tip electrode, we measured the PZC of thick cobalt oxide and iron oxide slurries, where the surface loading is maximum (incipient wet impregnation conditions).

Three initial pHs, 3, 6, and 9, were selected for the metal-free solutions to make slurries of pure cobalt oxide and iron oxide. The measured final pHs for each material are shown in Figure 2.4. Plateaus are seen in both cases as all initial pHs shifted to 7.2 or 6.2 for Co_3O_4 and Fe_2O_3, respectively. The same control experiments of metal-free solution for SiO_2 slurries were conducted and initial pHs were shifted to final pH at 3.5.

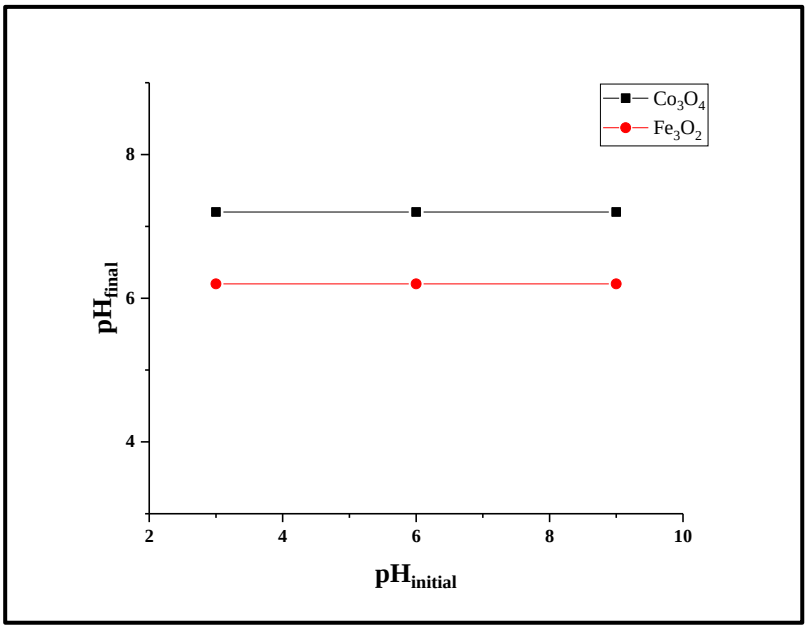

Figure 2.4: Control experiments of metal-free solutions pH shift date for pure oxides slurries (Co_3O_4 + Fe_2O_3)

The platinum adsorption experiment (uptake survey) onto pure oxides, thermally decomposed cobalt oxide, iron oxide and silica, was performed to demonstrate Pt uptake behavior on each pure oxide. Three sets of adjusted-pH (2-13) solutions of hexachloroplatinic acid (H_2PtCl_6, 99%) (200 ppm) were aged to stabilize their pHs. Then 500 m^2/L of each oxide, were contacted (separately) in CPA solutions, followed by shaking for about 1 hour, after which 5 ml of each contacted CPA solution-oxide was filtered and analyzed for Pt concentration measurement using a Perkin Elmer Optima 2000DV inductively coupled plasma (ICP) spectrophotometer. Pt concentration was also measured in pre-contact solutions; the difference in Pt concentrations of pre- and post- contact solutions represents the Pt uptake on each oxide as shown in Figure 2.5. All samples exhibit behavior attributable to electrostatic adsorption; the silica does not adsorb anionic complexes, while the Co_3O_4 and Fe_2O_3 do, although the Fe_2O_3, which has the lower PZC,

takes up more Pt than the Co_3O_4 which does not agree quantitatively with the RPA theory as seen in Figure 1.11.

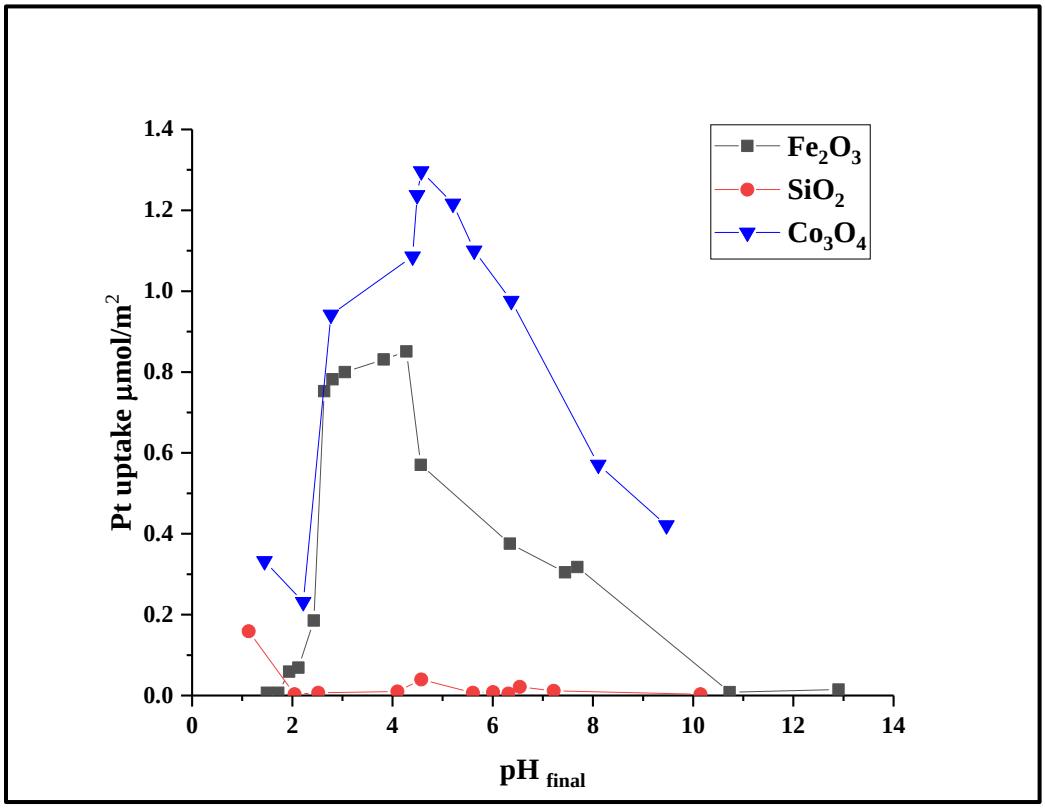

Figure 2.5: Pt uptake onto pure oxides (Co_3O_4, Fe_2O_3, and SiO_2)

Determination of the pH shifts of the pure oxides (Co_3O_4 and Fe_2O_3) was conducted at a low surface loading for comparison with the metal-containing uptake surveys. The pH-adjusted metal-free solutions with a range of pH from 2 to 13 were contacted with amounts of pure oxide equivalent to 1000 m^2/L surface loading. Figure 2.6 shows the pH shift data for pure oxides at low surface loading.

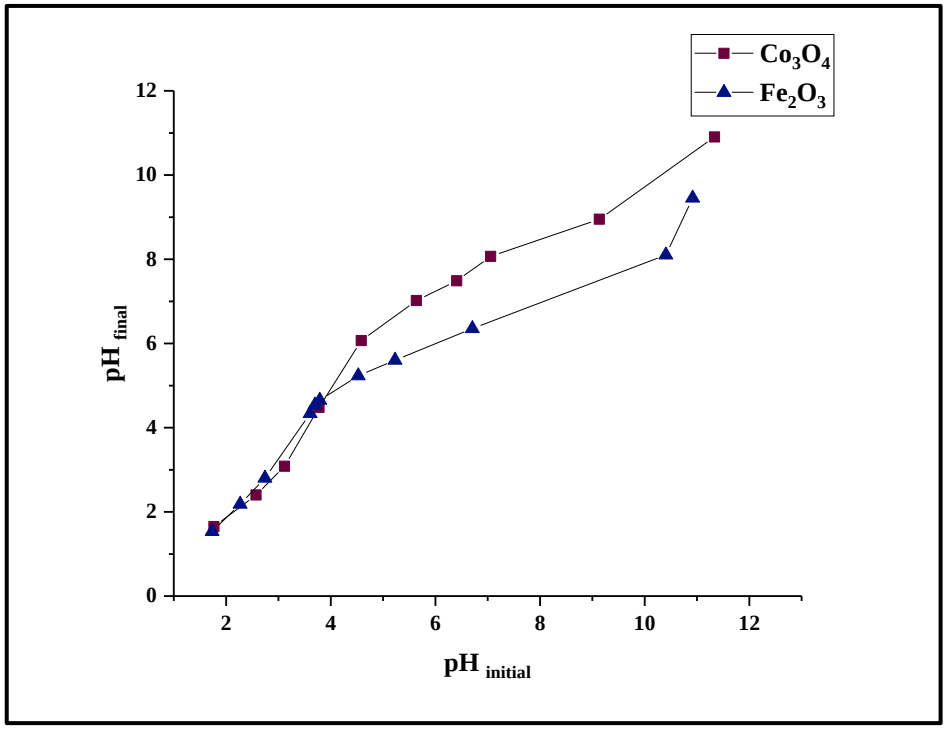

Figure 2.6: Control experiments pH shift of pure oxides (Co_3O_4 and Fe_2O_3) at SL = 1000 m^2/L

Physical mixtures of pure oxides Co_3O_4+SiO_2 and Fe_2O_3+SiO_2 were prepared with 0.083 g for silica, 0.453 g for Fe_2O_3 and 0.43 g for Co_3O_4, according to a different surface area of each oxide, to achieve 500 m^2/L or each oxide (1000 m^2/L SL total) with the CPA solution. Therefore, each of the two mixtures, Co_3O_4 + SiO_2 and Fe_2O_3 + SiO_2, were individually contacted in 50 ml of 200 ppm CPA solution at an initial pH (3.5 and 3.3) that gave the optimum final pH after contact (4.7 and 4.1), respectively, according to the Pt uptake onto transition metal oxide, depicted in Figure 2.5. The two samples were shaken for one hour, then filtered and dried at room temperature for 36 hours. The thermal treatment in the H_2 environment is set at 250ºC for one hour to reduce Pt to the metal phase. These samples were characterized by STEM, and chosen spots were analyzed by EDXS to obtain the weight percentage for different elements on both dark and light areas, which are presented in Figure 2.7.

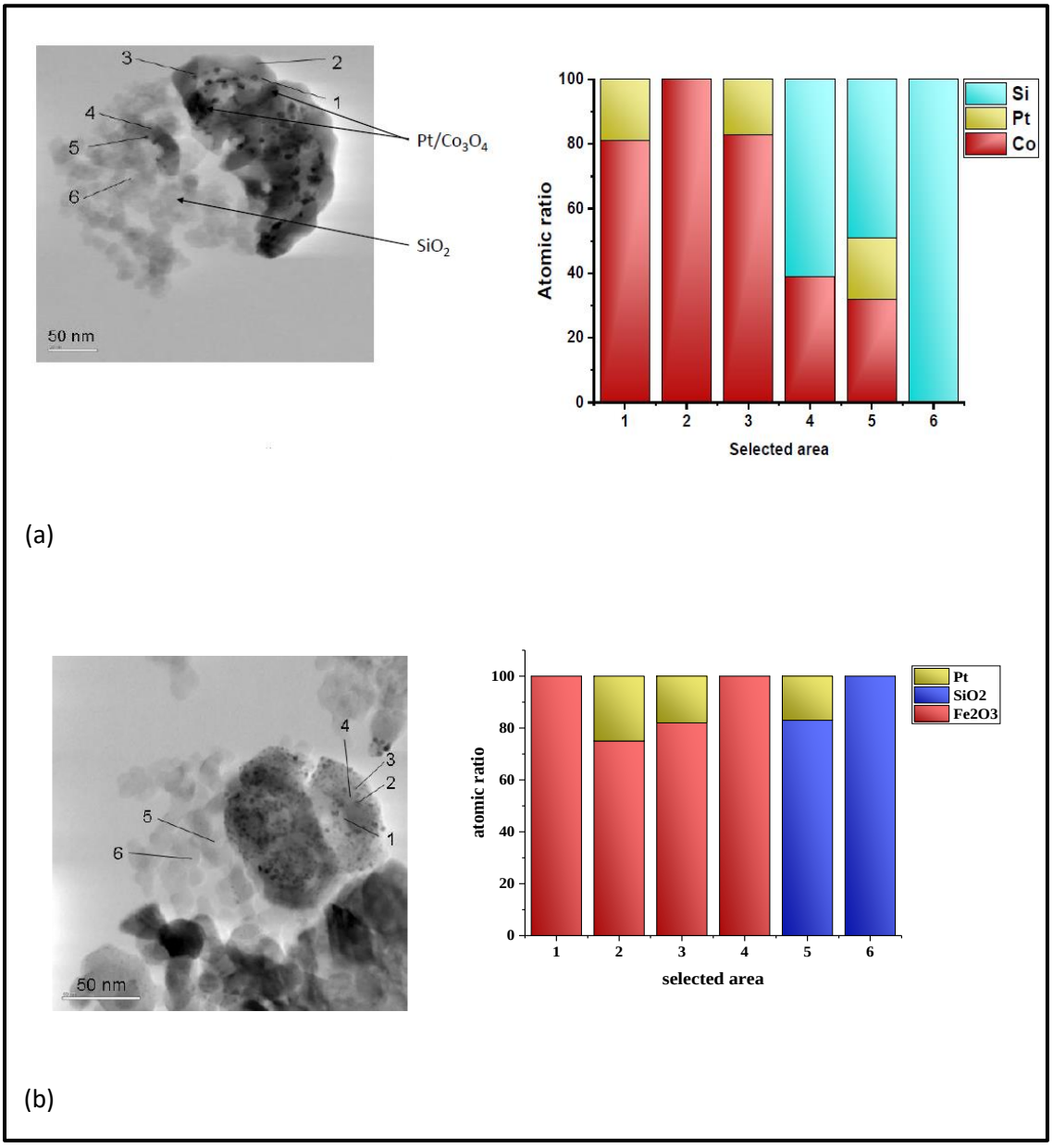

Figure 2.7: STEM images and EDXS results of samples reduced at 250ºC
(a) $Pt/(Co_3O_4+SiO_2)$, (b) $Pt/(Fe_2O_3+SiO_2)$

The partitioning of Pt as evidenced in Figure 2.7 will be addressed in detail in the discussion. To prepare the monometallic silica-supported cobalt oxide and iron oxide, incipient wetness impregnation was employed by dissolving cobalt nitrate ($Co(NO_3)_2 \cdot 6H_2O$, 98%) or iron nitrate ($Fe(NO_3)_3 \cdot 9H_2O$, 98%) with citric acid (mole/mole

for each) in a volume of deionized water corresponding to the silica pore volume (1.95 ml/g). The cobalt precursor salt was weighed to achieve 10 wt.% Co and a similar procedure was used for the iron-based catalysts, with a similar weight percent. The benefit of using citric acid is mentioned in many studies [103-104]. The optimum 6 nm size of cobalt nanoparticles and iron nanoparticles was achieved by using cobalt nitrate + citric acid and iron nitrate + citric acid which would increase the metal-support interaction. By adding the solution drop-wise to Aerosil®300 silica and continuously shaking, a paste eventually formed and was dried at ambient temperature for at least 36 hours. After drying the sample was calcined in a muffle furnace at 400 ºC for 4 hours and cooled to room temperature. The aforementioned Co/SiO_2 and Fe/SiO_2 prepared by citric acid enhanced IWI catalysts were tested for CPA adsorption. Similar to the Pt uptake survey that was conducted for pure oxide, 200 ppm CPA solutions, with final pHs in a range from 1 to 13 were contacted with silica-support Co- and Fe-based catalysts, as shown in Figure 2.8. These results will be discussed in detail in the discussion. The Pt promoted Co/SiO_2 catalysts were synthesized first by incipient wetness impregnation for Co/SiO_2 then second, by deposition of Pt using pH controlled to the optimal value. This synthesis sequence will be termed "sequential IWI-SEA." The amount of supported Co_3O_4/SiO_2 needed to give 1000 m^2/L of supported Co_3O_4 (as opposed to 1000 m^2/L of catalyst) was estimated from the Co_3O_4 particle size as determined from powder XRD (see Chapter 3) to be 16.7 g Co_3O_4/SiO_2 per liter of solution. 48 mL of solution were used, and so 0.8 g of Co_3O_4/SiO_2 was added into it. The chloroplatinic acid solutions were prepared in a range from 200 to 30 ppm and pH adjusted to achieve the optimum final pH, which was obtained from Figures 2.3 and 2.8. After one hour contact the solids were filtered and dried 36 hours. This was

repeated for each Pt solution (200 – 30 ppm). Pt concentration was measured in pre and post contact solutions to estimate the Pt wt.% loading. Similar procedures were followed for Pt-Fe/SiO_2 sequential IWI-SEA.

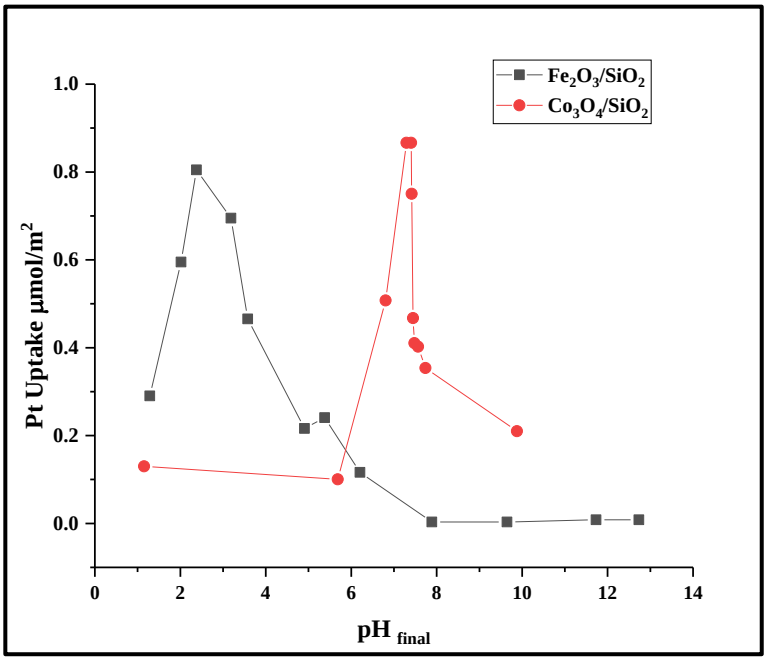

Figure 2.8: Pt uptake survey of 200 ppm CPA with 500m/L SL for silica supported Co- and Fe- based catalysts

A control set of catalysts was synthesized by co-impregnation with various Pt loading and constant 10 wt. % of either transition metal. These are labeled as simultaneous IWI catalysts. Both metal precursors of Pt and Co were dissolved in DI water with amounts corresponding to the metal weight loadings of the first method of sequential incipient wetness impregnation + strong electrostatic adsorption. A similar procedure was followed for Pt-Fe catalysts. Then, samples were dried for two nights at ambient temperature and calcined in the muffle furnace at 400ºC for 4 hours. Based on TPR, the

catalysts were thermally treated in a mixture of H_2 and He to reduce Co and Fe nanoparticles at the appropriate temperature.

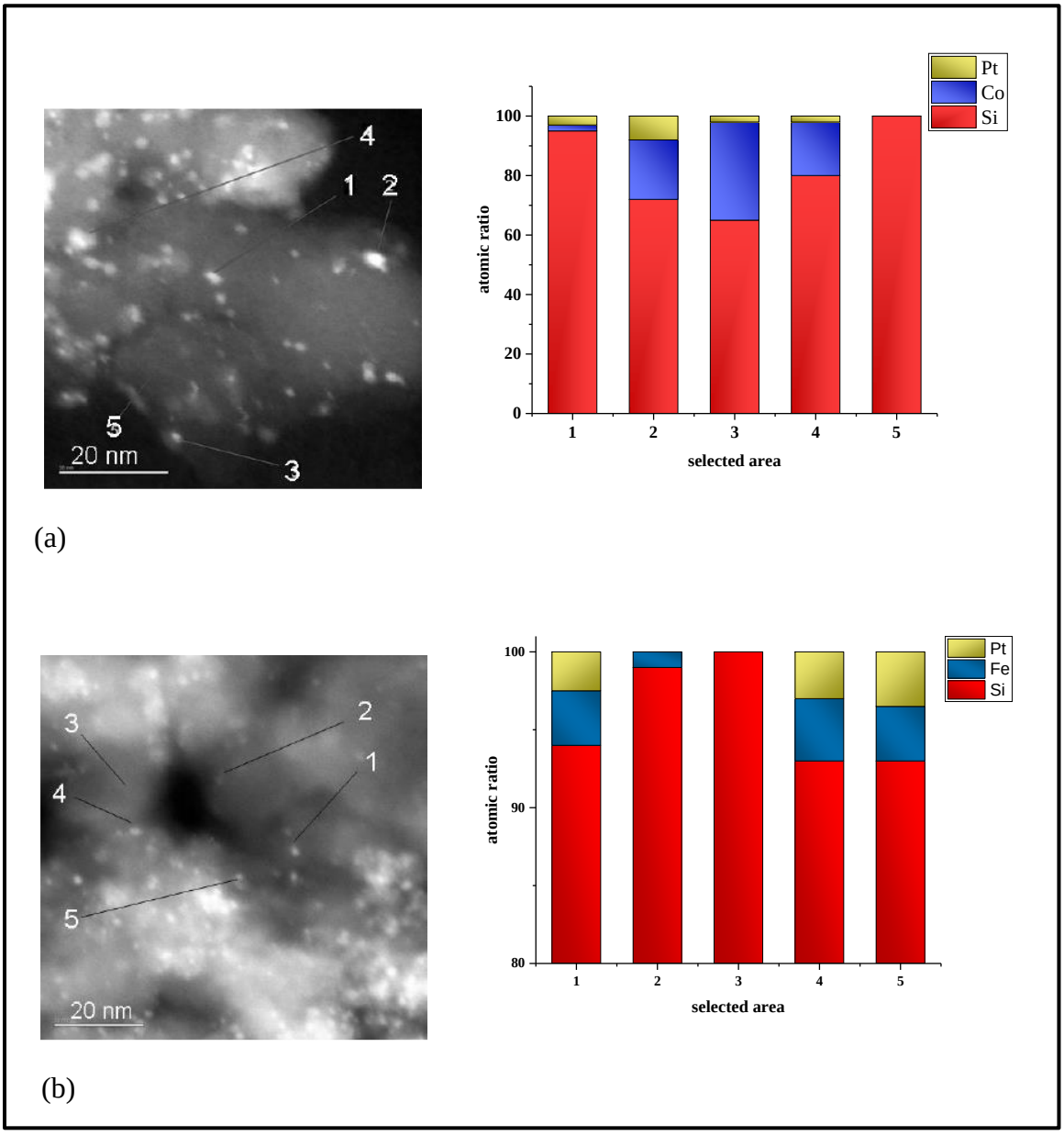

Figure 2.9: STEM images for (a) Pt-Co/SIO_2 sequential IWI-SEA (b) Pt-Co/SIO2 sequential IWI-SEA and their EDXS analyses

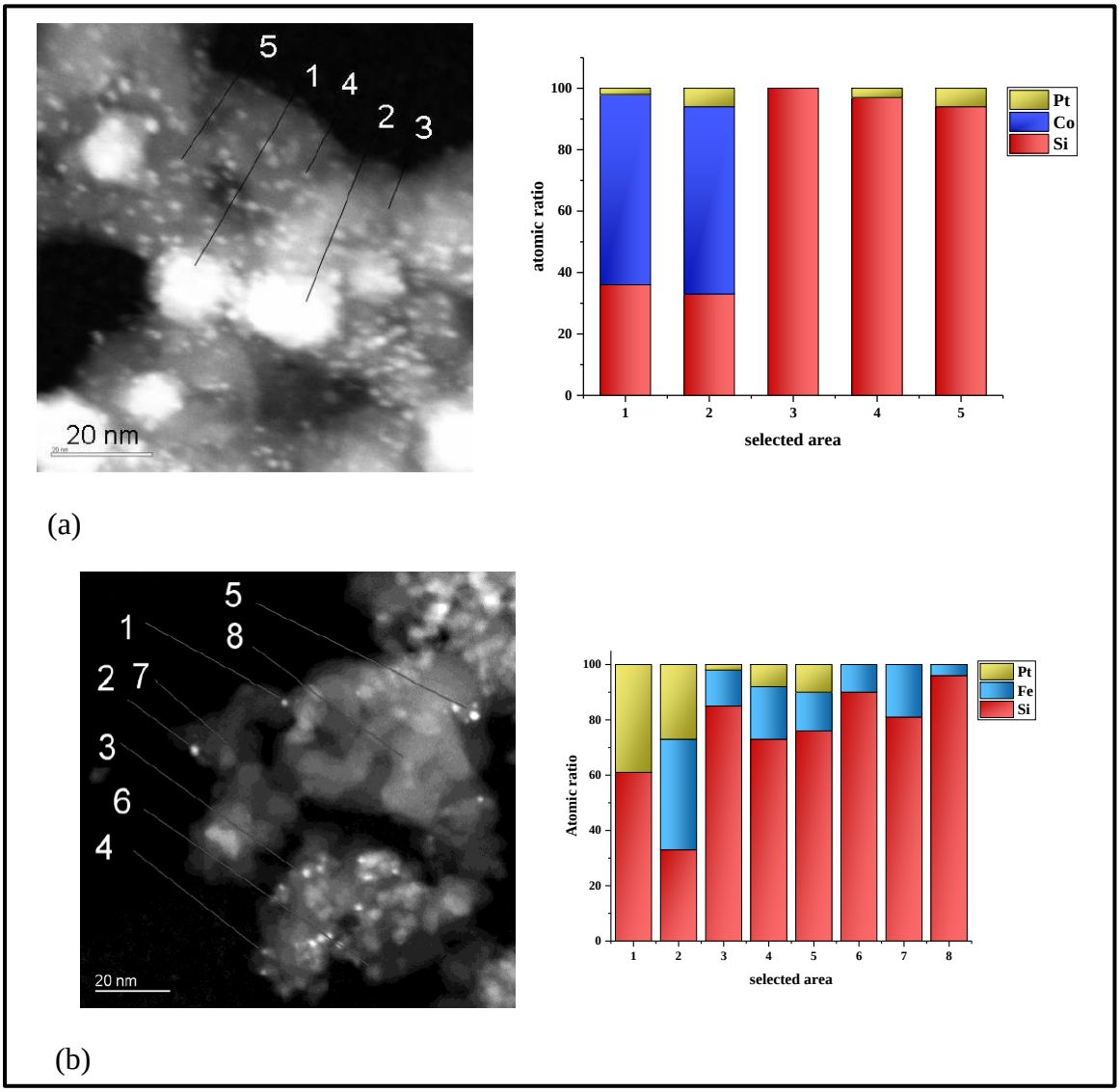

Figure 2.10: STEM images for (a) Pt-Co/SiO_2 simultaneous IWI (b) Pt-Co/SiO_2 simultaneous IWI and their EDXS analyses

Figure 2.9 shows the distribution of Pt nanoparticles, which are readily apparent from HAADF STEM images and can be seen by observing bright spots, which represent the

metal particles. Therefore, well distributed Pt nanoparticles were observed on Co/SiO_2 and Fe/SiO_2 catalysts. These are prepared by the rational synthesis method of sequential IWI-SEA. Spots were then chosen for EDXS elemental analysis and are shown in Figure 2.9 for both catalysts beside STEM images.

A similar characterization of HAADF STEM images was conducted for the second method of preparation, which is the conventional co-impregnation or simultaneous IWI for both Co and Fe catalysts. From this, it was obvious that Pt nanoparticles' dispersion in simultaneous IWI is less compared to analysis from sequential IWI-SEA catalysts. All of these images and each EDXS analysis are shown in Figure 2.10. These characterizations of STEM and EDXS analysis were conducted during previous work of our group, C. Cao et al.

2.3 Discussion

The adsorption of CPA on each oxide, SiO_2, CO_3O_4, and Fe_2O_3 is different. In Figure 2.5, almost no adsorption was observed on SiO_2, and that is explained by the low PZC of SiO_2. It is concluded that the anionic CPA precursors in the solution do not adsorb on silica below its PZC. Not only is the silica surface not strongly protonated and positively charged, at low pH the ionic strength, which is deleterious to adsorption, is high. This observation on silica was studied by Schreier and Regalbuto using the RPA model and conducting an uptake survey experiment of the platinum tetraammine chloride precursor solution onto silica. The retardation in Pt uptake occurred at an extremely basic pH, due to the high ionic strength of the high concentration of hydroxide ions in this solution [105].

Shah and Regalbuto observed the effect of ionic strength by conducting a series of Pt uptake experiments over alumina and silica oxides by varying experiment conditions, in an effort to isolate effect of the support dissolution from ionic strength. However, it was verified that at extreme pH levels, the retardation of Pt uptake is caused by ionic strength effects at which a decrease in double layer thickness and "electric screening" of the charged surface by electrolyte occurs and consequently reduces the adsorption constants [106-108]. Another noticeable observation from Figure 2.5 is the difference in uptake of Pt onto iron oxide and cobalt oxide surfaces. This might be attributed to the difference in the degree of Pt complex hydration over the different oxides.

The study of Pt uptake on pure oxides gives the optimum pH at which Pt uptake is highest on each oxide. According to the Pt uptake data in Figure 2.5, the optimum final pHs are 3.6 and 4.7 for Fe_2O_3 and Co_3O_4, respectively, and that is consistent with SEA principles, by which the adsorption of Pt occurred on the positively charged surfaces of Fe_2O_3 and Co_3O_4 at pH below their PZCs, which are typically more basic compared to the silica PZC. Since silica has low PZC, a very small uptake was observed, but it is considered a negligible amount compared to Pt uptake on transition metal oxide surface.

This is an advantage of our rational synthesis and confirms the selective adsorption of CPA onto transition metal oxides surfaces, instead of being wasted on the silica surface. Moreover, the amount of Pt that is adsorbed onto th transition metal oxide surface can be controlled during SEA synthesis procedures by adjusting the CPA concentration in the impregnation solution. This ability of selective adsorption of Pt and controlling its amount would lead to more control on Pt-Co or Pt-Fe interaction, and therefore, the pronounced effect of the presence of Pt onto transition metal surfaces would be studied easily and could

be more beneficial toward improving catalysts' reduction and FT reaction performance. The selective adsorption of CPA was observed also in a physical mixture of the oxides. The reduced physically mixed oxides (Fe_2O_3+SiO_2) and (Co_3O_4+SiO_2) were imaged by STEM and analyzed by EDXS as seen in Figure 2.7. In these images, the platinum nanoparticles were observed in the darker areas, while bright areas had very small amounts. Also, the weight percent of different elements have been analyzed by EDXS for chosen spots on both dark and bright areas.

It is obvious from the EDXS spot analysis of the physical mixtures that the Co_3O_4 phase (the darker areas) hosts the most Pt, more than 95%, and this is an indication of a selective adsorption onto Co_3O_4, while no Pt was detected on chosen spots of the silica surface as shown in the images of Figure 2.7 (a). Similarly, with a physical mixture of (Fe_2O_3+SiO_2), more than 99% of Pt was found on the iron oxide surface and very small amounts on the silica surface. The transition metal oxide surfaces seem to have more electrostatic attraction to Pt than silica, due to the high potential charge built on their surfaces at low pH. Therefore, based on the CPA survey and STEM-EDXS results, the anionic Pt complexes can be controlled by selective deposition onto either Co_3O_4 or Fe_2O_3 surface, but the very little amount, less than 5%, might still be adsorbed on the silica surface.

The uptake of Pt onto Co_3O_4/SiO_2, Fe_2O_3/SiO_2, and SiO_2 is presented in Figure 2.8. The shape of the Pt uptake peak on Co_3O_4 is very sharp and is located at the Co_3O_4 PZC. This might be attributed to a difference in cobalt oxide species' behavior from large particles to small particles. In small nanoparticles of cobalt oxide, the Co^{2+} are more concentrated on the surface, and that would alter the electrochemical properties of cobalt

oxide [106-107]. The interaction between the Pt complex and the cobalt oxide surface supported by silica does not appear to follow the SEA mechanism, while the Fe_2O_3/SiO_2 does, exhibiting a CPA uptake almost at the optimum final pH of CPA uptake, similar to the pure iron oxide Pt uptake.

The HAADF STEM images for Pt-Co/SiO_2 sequential IWI-SEA and Pt-Fe/SiO_2 sequential IWI-SEA are presented in Figure 2.9 (a) and (b), respectively. Here, high dispersion of Pt-Co and Pt-Fe nanoparticles can be readily observed. Therefore, using the SEA to add Pt keeps the particle size relatively small after thermal treatments. From chosen spots for EDXS analysis, the Pt-Co/SiO_2 shows Pt and Co usually coexist in the same spot, which indicates the interaction is intimate. Therefore, Pt is mainly deposited on Co surfaces. A similar observation was readily seen in Pt-Fe/SiO_2 EDXS analysis.

The bimetallic Pt-Co and Pt-Fe prepared by co-impregnation of IWI, resulted in less interaction between Pt and transition metals. It is obvious from STEM images in Figure 2.10 (a) that large particles of Pt-Co were seen, and its EDXS analysis showed Pt particles on both silica and Co surfaces, which means the adsorption of Pt during catalysts synthesis is uncontrolled. This consequence is a result of the absence of interaction between the Pt complex and transition metal surface.

Figure 2.10 (b) for Pt-Fe/SiO_2 simultaneous IWI or co-impregnation shows similar results compared to Pt-Co/SiO_2 STEM-EDXS results, and Pt particles were observed on both silica and iron oxides surfaces. This study is providing evidence of the beneficial use of SEA, or at least, of pH control, as a rational and efficient preparation parameter which exploits the significant potential of transition metal oxide surfaces, as they can be charged

to address the individual noble metal complex adsorption via strong electrostatic attractions. Thus an adsorbiong noble metal would strongly interact with the surface and after thermal treatment at elevated temperatures, well-dispersed nanoparticles can form, increasing the density of promoted active sites.

2.4 Conclusion

The adsorption of Pt onto pure transition metal oxides and silica surfaces was conducted and compared to the Pt adsorption onto silica-supported transition metal catalysts. Pt uptake survey shows no Pt adsorption on silica. This is attributed to the lack of electrostatic force of adsorption between the silica and Pt complexes in the solution due to the low PZC of silica and the effect of ionic strength at extremely acidic pH of the solution. Therefore, the adsorption of anionic Pt complexes can be selectively adsorbed onto transition metal oxide surfaces due to the different potential behaviors of the transition metal surfaces caompred to the silica surface potential charge and their relatively high PZC. Well-dispersed nanoparticles were observed for Pt using SEA (or pH control), but IWI method does not provide selective deposition of Pt onto transition metal oxide surfaces. EDXS analysis showed that the Pt nanoparticles are located on transition metal surfaces and silica surface in simultaneous IWI catalysts. The SEA has the ability to selectively deposit Pt, more than 95%, onto transition metal surfaces. The lack of electrostatic attraction on transition metal surface using IWI would lead to an inefficient use of Pt particles. Control of pH to that of optimum interaction leads to an intimate interaction between Pt and transition metal, which enhances the noble metal functionality and potentially increases its efficient use to improve FT catalyst reducibility and reaction performance. This is examined in the next two chapters.

CHAPTER 3

CHARACTERISTICS AND CATALYTIC ACTIVITY OF PLATINUM-PROMOTED COBALT-BASED CATALYSTS

3.1. Introduction

Nowadays, Cobalt-based catalysts play a key role in the CO hydrogenation reaction due to their active CO adsorption and sufficient hydrogenation rate during methylene (surface-monomer) formation, chain propagation, and termination elementary steps in the FT reaction. In commercial FTS, Fe and Co-based catalysts are widely used, due to the compromise between catalysts' price and activity, but the choice between them is determined by the purpose of FT technology and source of syngas feedstock. As mentioned in Chapter 1, the superior CO hydrogenation activity at low temperatures, long life, and high selectivity toward both high molecular-weight and low aromatic straight chain hydrocarbons of cobalt-based catalysts were accounted for in order to show Co as the best choice for LTFT synthesis. However, the main challenges of Co catalyst design are maximizing the number of active surface sites, increasing the intrinsic activity TOF, and tuning the hydrogenation rate to reduce low molecular-weight hydrocarbons. These factors are interrelated to each other, and for Co-based catalysts, the number of active sites can be influenced by metal-support interaction, the structure of support, pore, and catalyst synthesis.

Earlier studies have focused on the effect of Co particle size on the reaction activity, which was normalized to Co weight loading [109-110]. In these studies, the activity showed a dependency on the particle size of Co in a range of size. It was concluded that cobalt is structure-sensitive and its activity increases with its particle size. While Iglesia in 1997 verified the independence of normalized activity, TOF, for Co particles greater than 9 nm [44], which indicates structure-insensitivity. Below 9 nm there is a dramatic decrease in TOF. This was attributed to many effects, such as high concentration of Co^{+2} in small Co nanoparticles and strong interaction between metal and support, which would form a cobalt-support complex. However, this complex is hard to reduce. Others ascribed this to the formation Co-carbide in the small nanoparticles of Co and others attributed this to the direct effect of chemical properties of the support [44], [71], [111], & [112].

Later, Bezemer et al. studied the effect of Co particle size on catalytic activity and reaction performance, but that effect was isolated from strong metal-support interaction by applying this study on carbon nanofiber-supported Co, so the carbon nanofiber is inert for the reaction and has no metal-support interaction effect on Co nanoparticles [60]. In their study, different Co precursors and different weight loadings were chosen to have a range of Co particle sizes from a few nanometers to about 50 nm. The TOF shows independent correlation with Co particles' size greater than 6 nm for 1 bar reaction pressure and 8 nm for 35 bar reaction pressure, while for Co particles smaller than 6-8 nm, the TOF is dramatically retarded, according to the decrease in Co particles size. This effect of the particle size on catalyst activity, TOF, methane selectivity, and hydrogenation is depicted in Figure 3.1.

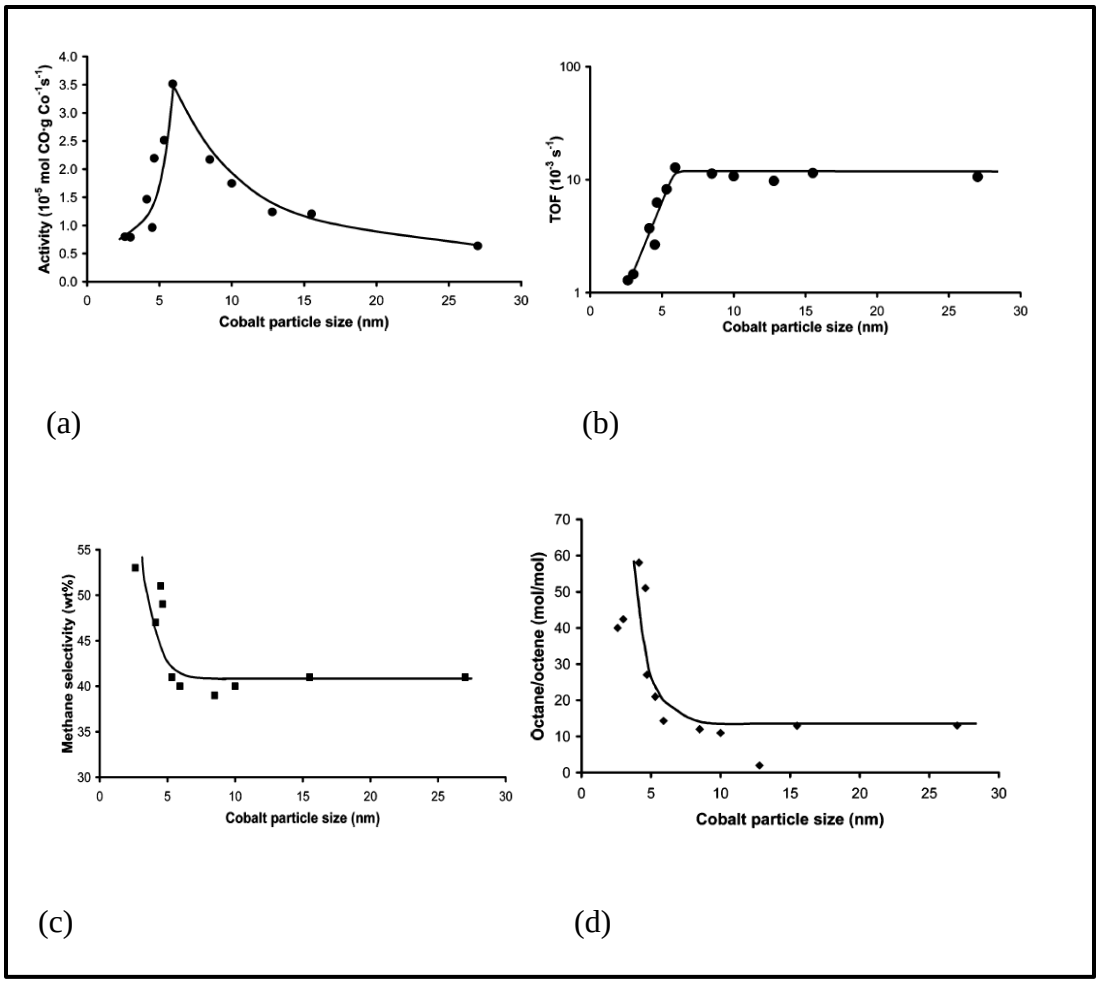

Figure 3.1: The influence of Co particle size on (a) activity normalized to the cobalt loading (b) TOF, (c) methane selectivity, (d) hydrogenation

Similar behavior was demonstrated later by Breejen et al. studying the effect of Co nanoparticle size on catalytic performance and applying Steady-State Isotopic Transient Kinetic Analysis (SSITKA). It was found that the increase of irreversibly bonded CO in small Co particles below 6 nm is attributed to the increase in low-coordinated surface sites. Therefore, these sites (corner and edge) become blocked, resulting in lower activity and TOF of small Co nanoparticles [71].

Oxide supports such alumina, titania, and silica are the most widely used to support the Co small nanoparticles and improve their volumetric productivity at high dispersion based on the high surface area these supports have. The pore size and chemical properties of support surfaces have some influence on the Co particles' reduction and reaction behaviors. It was reported that the Co particle size on γ-alumina was smaller than the ones on α-alumina, which is attributed to the difference in chemical properties between different kinds of alumina. However, the main challenge in supported Co-based catalysts is how to mitigate the strong metal-support interaction [113-114].

According to literature, there is a general agreement on the optimum size for Co particles (6-8 nm) in order to have maximum intrinsic activity at the highest number of active sites. However, a decrease in Co particle size is accompanied by increased resistance to reduction, as studied by Khodakov et al. [113]. In their results of XRD, EXAFS, and FTIR, the hydrogen reduction properties of Co were reported to decrease from large Co particles (70 nm) to small particles (6 nm). Thus, it hard to reduce small Co nanoparticles, and that was attributed to the presence of different species of Co ions in Co particle surfaces, the percentage of which increases with small Co nanoparticles.

Adding promoters to the catalyst can be one of the most efficient methods to address the challenge in Co-based catalyst design. Promoters can increase Co active sites, known as a structural promotion, and facilitate the reduction of small Co nanoparticles at a lower temperature. Another possible beneficial use of promoters is reducing the activation energies at FT elementary reaction steps by altering the electronic properties of the active sites. This is known as electronic promotion. These benefits are usually associated with an increase of catalyst stability and lifetime [115].

One of the most widely used promoters is the platinum, compared to other noble metal promoters, Ru, Re, and Pd. This preferred choice of promoters is feasible in commercial FTS due to a relatively high global production of Pt compared to other promoters, which are scarce. An early study on the addition of Pt in the Co-based catalyst was investigated by Zsoldos et al.; they noticed a significant increase in Co extent of reduction by adding very small amount of Pt, 1.5 wt.% [116]. The effect of promotional effect of Pt on CO conversion was observed by Schanke et al. It exhibited a 3-5 time increase in the CO-hydrogenation rate and it was greatest at atmospheric pressure. It was also found that 0.1% Pt is sufficient for approximately 70% increase in catalysts activity [117-118 However, the presence of Pt, particularly in high weight loading, results in high selectivity in methane and low molecular-weight hydrocarbon, low chain growth probability, and low C_{5+} selectivity. This effect of high rate methanation is known as reverse syngas production, and the target of catalyst design is to minimize it [119]. It has been noted that the promotional Pt performance on catalytic activity, metal dispersion, and reduction behaviors is strongly affected by the synthesis method and thermal activation procedure of bimetallic Pt-Co catalysts [120].

In this study, we will focus on using a rational synthesis method to selectively deposit the precious noble metal Pt onto the Co oxide surface. Strong Electrostatic Adsorption (SEA) is used to synthesize Pt-Co catalysts; these will be compared with a second set of conventionally prepared catalysts using co-incipient wetness impregnation of Pt and Co. All catalysts in both sets are supported by high surface area silica. The characterization and a catalytic comparison between each catalyst set will be demonstrated.

3.2. Materials and methods

3.2.1 Preparation

First, the monometallic silica-supported cobalt oxide was prepared using incipient wetness impregnation by dissolving cobalt nitrate ($Co(NO_3)_2 \cdot 6H_2O$, 98%) and citric acid (mole/mole ratio) in a volume of deionized water corresponding to the pore volume of silica support. Accordingly, the cobalt precursor salt used was weighed to achieve 10 wt.% of Co of the total weight of Co/SiO_2. The benefit of using citric acid is mentioned in Chapter 2 section 2. An easy way to get the optimum size of cobalt nanoparticles was utilizes the addition of citric acid to cobalt nitrate to increase the metal precursor-support interaction. By drop-wise adding solution to Aerosil®300 silica and shaking continuously, a paste eventually formed and was dried at ambient temperature for at least 48 hours. The sample after drying was calcined in a muffle furnace at 400 ºC for 4 hours and cooled to room temperature.

The first series of $Pt\text{-}Co/SiO_2$ catalysts was prepared by a sequence of two procedures. The first is mentioned in the previous paragraph, utilized citrate-assisted IWI to prepare 10 wt.% Co/SiO_2. In the second procedure, SEA was used to deposit different loadings of Pt onto Co/SiO_2 by changing the initial concentration of Pt and adjusting to the pH at optimum, according to the Pt uptake survey on silica-supported cobalt catalysts data that was presented in Chapter 2. The final optimum pH was reported at 7.2; thus, for all samples, a corresponding initial pH was selected such that the final pH of each shifted to the optimum. The weight loading of Pt was calculated by conducting ICP measurement for CPA pre- and post-contact with Co/SiO_2.

In the initial CPA solutions, concentrations varied from 200 ppm to 30 ppm. To achieve the lowest Pt loading, a surface loading of 2000 m^2/L was employed with 30 ppm solution. A significant decrease in Pt wt. loading was achieved compared to 30 ppm prepared at 1000 m^2/L. After impregnation and filtering, all samples were dried at room temperature for 48 hours and then at 100ºC for 2 hours, before conducting a TPR experiment to investigate the reduction profile of Pt-Co/SiO_2 catalysts.

Another set of series of Pt-Co/SIO_2 catalysts was synthesized in a single step of co-incipient wetness impregnation. Both metal precursors, platinum tetraammine chloride and cobalt nitrate hexahydrate were dissolved in DI water in amounts corresponding to the metal weight loadings of the first series of Pt-Co/SiO_2 samples that used two the two steps of preparation, IWI + SEA. The samples were dried for 48 hours at ambient temperature and calcined in the muffle furnace at 400ºC for four hours.

The purpose of the preparation of the second series of Pt-Co/SiO_2 is to compare our rational synthesis of SEA, with the conventional and most commonly used preparation of co-incipient wetness impregnation. This conventional method cannot achieve the selective deposition of Pt onto Co_3O_4 surface and due to the lack of interaction between the cobalt oxide surface and platinum. Therefore, it is anticipated that Pt would deposit on both oxide surfaces, cobalt oxide and silica. Next, the TPR experiment, with similar condition and gas flow to the first set of catalysts, was conducted for this second set of Pt-CO/SiO_2, samples, to investigate the reduction profiles of Co. More details of TPR experiments will be mentioned in the following section.

3.2.1. Characterization

Monometallic and bimetallic samples were analyzed by powder X-ray diffraction (XRD) performed on Rigaku Miniflex II benchtop diffractometer with a CuKα radiation source (λ = 1.5406 Å) operated at 30kV and 15 mA. Scanning was conducted over a 2θ range of 10-80º with a scanning speed of 1º/min. Samples were loaded in a holder with an amorphous glass background and a sampling width of 0.02º. A high sensitivity Rigaku D/tex ultra diffractometer equipped with a silicon strip enables very small nanoparticles (~ 1.5 nm) to be detected and observed in XRD profiles. Metal nanoparticles sizes were calculated using the Scherrer equation.

H_2-reduction properties were characterized by H_2 temperature program reduction (TPR) profiles, where a 100-mg dried and calcined sample was loaded on quartz wool in a quartz tube. A 10% H_2 balanced with Ar with 50 ml min^{-1} flow was introduced to the sample. The H_2-consumption was monitored by a thermal conductivity detector (TCD) over the temperature range from ambient temperature to 800 ºC with a ramp rate of 5 ºC/min. High angle annular dark field (HAADF) images were obtained by using an aberration-corrected JEOL JEM-ARM200CF (200 kV electron) scanning transmission electron microscopy (STEM) with an imaging resolution of 0.078 nm and an energy resolution of 0.35 eV. Also, Thermo Noran Vantage Energy Dispersive X-ray spectroscopy (EDXS) analysis was conducted by Chongjiang Cao, Zongxuan Hong and John R. Regalbuto at the University of Illinois at Chicago for physical mixtures of cobalt oxide and silica, which was exposed to a 200 ppm (pH-adjusted at 3.33) chloroplatinic acid solution and pretreated in H_2 at 250 ºC for 1 hour. The images and EDXS analysis results were discussed in Chapter 2. The sample surface area was measured by the Brunauer-

Emmett-Teller (BET) ASAP 2020 Micrometrics apparatus. N_2 physisorption for surface area, microporous, and mesoporous measurements were performed by the ChemBET-300 apparatus Quantachrome instrument.

3.2.2. Fischer-Tropsch reaction test

Carbon monoxide hydrogenation reaction (Fischer-Tropsch synthesis) was carried out in a fixed bed stainless steel tubular reactor (d_{in}=5 mm and length=50 cm) operating at 220ºC and 20 bar (Figure 3.2). Two thermocouples were used: one in contact with the sample inside the reactor to monitor the temperature, and the other in a hole in an aluminum shell (length=25 cm) that surrounds the middle part of the reactor to minimize the high exothermicity effect of FT reaction and avoid hot spots. A 100 mg sample was crushed and sieved (149-250 microns), and mixed with 400 mg crushed and sieved quartz with a similar mesh size to maintain steady temperature through the catalyst bed. Three mass flow controllers were used to control CO, H_2, and He flows into the system, and a back pressure regulator was mounted just after the reaction zone to pressurize reactant flow to the target pressure. 60 sccm total flow with $H_2/CO \approx 2$ and balanced with 15 sccm of He were introduced to the reactor, after H_2 pretreatment of the loaded sample at atmospheric pressure and 400 ºC for 4 hours. A cold trap was used at 10ºC downstream of the back pressure regulator, where the pressure is atmospheric, to collect waxes and heavy hydrocarbons. The gas phase product, which was split from the liquid phase in the cold trap, is analyzed by a gas chromatograph (GC) with two HP PLOT-Q columns and equipped with thermal conductivity and flame ionization detectors. The temperature in the GC was programmed to analyze and separately identify hydrocarbon paraffins and olefins in a range of C_1 to C_8.

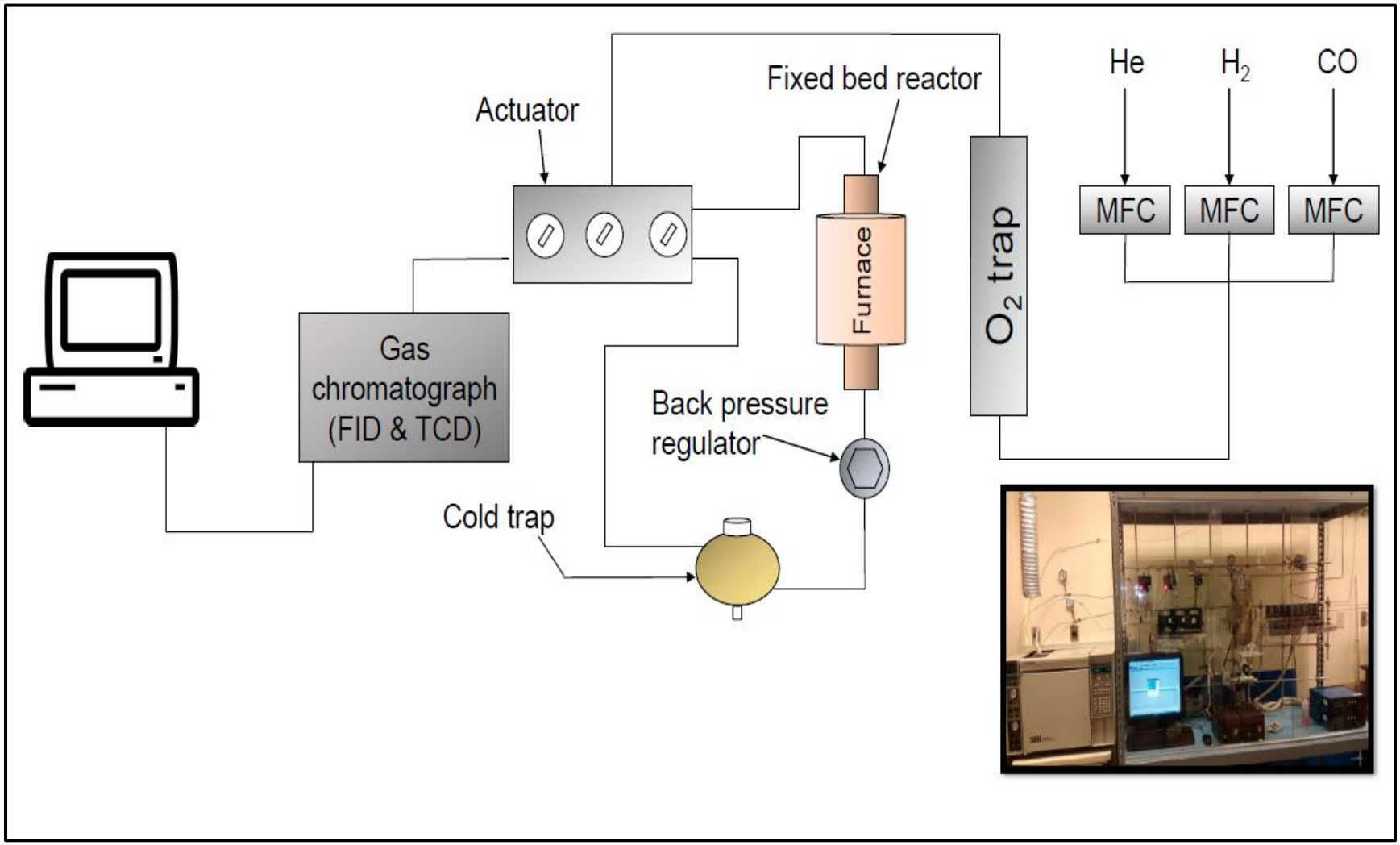

Figure 3.2: Fischer-Tropsch reaction flow system equipped with GC

3.3. Results and discussion

Results from Pt adsorption onto Co/SiO_2, including Pt wt% and Pt/Co atom%, are presented in Table 3.1. In Pt uptake experiments, we employed various initial Pt concentration (30-200) following SEA procedure, but since there is no significant difference between 200 ppm and 150 ppm uptake, we considered the 150 ppm as the highest Pt wt. loading in all subsequent experiment and excluded 200 ppm. Moreover, we repeated the 30 ppm at higher surface loading to minimize the weight loading of Pt. The surface loading was chosen according to the specific area of Co_3O_4 calculated from the approximate nanoparticle size that was analyzed by XRD, 62 m^2/g. Therefore, 1000 m^2/L was chosen for all sample except the last one, the 30 ppm solution, that was contacted with athet higher surface loading at 2000 m^2/L. We assume there is no uptake on SiO_2 based on the STEM-EDXS result in Chapter 2 for Pt uptake on a physical mixture of oxides (SiO_2+Co_3O_4) and Pt-Co/SiO_2 sequential IWI+SEA catalysts. Therefore, by varying the initial concertation of Pt we were able to produce a diverse Pt/Co atomic% from the highest at 0.89 % to the lowest at 0.02 %.

Table 3.1: Pt weight loading and Pt/Co atomic % based on SEA uptake onto Co/SiO_2

Initial Pt Conc. (ppm)	Final Pt Conc. (ppm)	Pt uptake μmol/m^2	Pt/Co atomic %
150	25	0.86	1.7
100	18.6	0.73	0.7
50	13.8	0.38	0.2
30	9.67	0.11	0.08
30*	~ 0	0.02	0.03
0		Co/SiO_2	

(*) conducted at higher surface loading 2000 m^2/L

Another series of samples, prepared by co-incipient wetness impregnation also known as simultaneous impregnation of Pt and Co, had Pt/Co atomic%'s of 1.72, 0.23 and 0.03. It should be mentioned that the amount of cobalt is fixed in all samples as originally prepared at 10 wt. %, and was kept the same as well for Pt-Co/SiO_2 simultaneous-IWI catalysts. Both series of catalysts, Pt-Co/SiO_2 sequential IWI + SEA and Pt-Co/SiO_2 simultaneous IWI, have been calcined at 450 ºC for 4 hours and TPR was first conducted to determine the optimum temperature for the thermal reduction treatment of catalysts. All samples were reduced at 650 ºC in 10% H_2/He for 4 hours and XRD was conducted for reduced samples as depicted in Figure 3.3 and 3.4 for Pt-Co/SiO_2 sequential IWI + SEA and Pt-Co/SiO_2 simultaneous IWI, respectively.

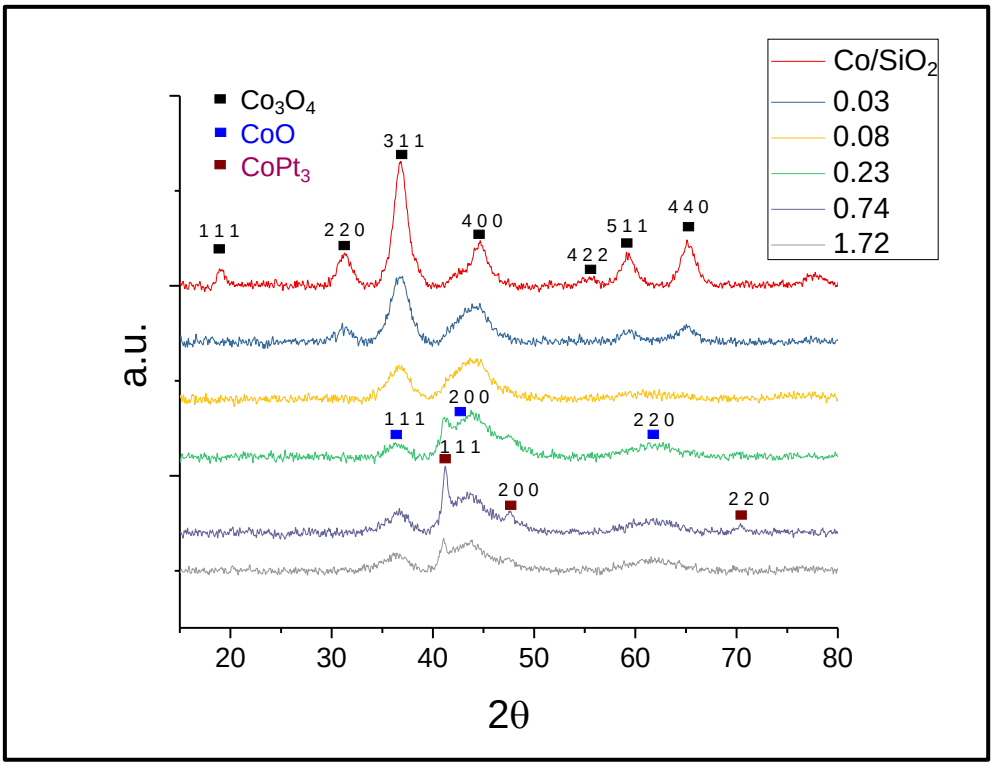

Figure 3.3: XRD profiles of Pt-Co/SiO_2 sequential IWI +SEA catalysts

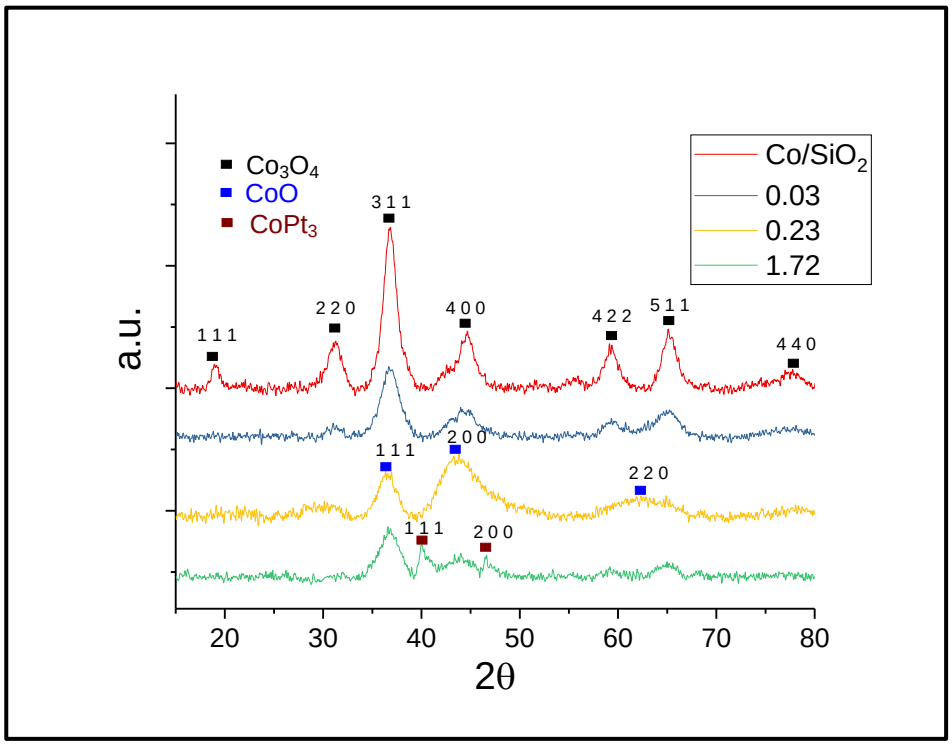

Figure 3.4: XRD profiles for Pt-Co/SiO_2 simultaneous IWI catalysts

From Figure 3.3 for Pt-Co/SiO_2 sequential IWI + SEA, the monometallic Co-based catalyst that was prepared by IWI was included in these profiles as a control sample at Pt/Co atomic % of 0. The main structure that was detected by XRD was Co_3O_4 in the monometallic Co/SiO_2 (the first XRD profile from the top) with an average particle size around 5.3 nm. The appearance of a small shoulder just after the peak at 38º 2θ indicates the presence of CoO, which was not detected in the calcined monometallic Co/SiO_2 XRD profile. The size of CoO was calculated from Scherrer equation as 6.1 nm (Table 3.2). As Pt is added, there is a drop in Co_3O_4 nanoparticle size from 7.8 nm to 5.3 nm, which might be ascribed to a reduction of a small portion of Co_3O_4 to either CoO or Co^0 metal phase in a size that is not detectable by the X-ray diffractometer. The reduction of the Co_3O_4 nanoparticles size is caused by the addition of Pt. This change is reflected in the broadening

of Co_3O_4 peaks. and is correlates with the amount of Pt, and this effect is extended to CoO as well, starting from the smallest amount of Pt. The appearances of Co (fcc), Co (HCP), and $CoPt_3$ were detected from 0.08 Pt/Co atomic %. The particle size of Co (fcc) and Co (hcp) seems to be unchanged by the amount of Pt, and they are almost constant in a range of (2.6 to 4.1) nm and (2.1 to 3.2) nm, respectively. A $CoPt_3$ alloy is detected and its particle size increased from 5.5 to 15 nm with increasing amounts of Pt deposited onto the Co_3O_4 surface. The (111) peak of the $CoPt_3$ fcc-like structure was detected at 41.1º and it appears at higher 2θ compared to the Pt-rich structure which its (111) facet usually appearing between 39 and 39.5º. That shift in (111) $CoPt_3$ is attributed to a change in the Pt fcc lattice constant of 3.899 Å caused by the presence of Co atoms in the structure. The transition from disordered alloy to the ordered $CoPt_3$ structure has been reported to be affected by the thermal treatment temperature and in our case, the catalysts were reduced in 650 ºC. Therefore, the $CoPt_3$ that appeared in XRD profiles is in the ordered form [121-122]. This is an indication of an intimate interaction between the Co and Pt that was formed by the selective deposition of Pt onto Co_3O_4 and sufficient temperature of treatment.

In Pt-Co simultaneous IWI XRD profiles, the reduction in Co_3O_4 is observed and correlated with the amount of Pt, but the structure of CoO seems to be more stable and almost unchanged with respect to the amount of Pt. Its average particle size is deconvoluted from Co (fcc) and Co (hcp) peaks and computed to be 3.4 nm (given in tables 3.2 and 3.3). The appearance of $CoPt_3$ was detected only at high wt loading of Pt, which might be attributed to the lack of intimate interaction at medium and low wt of Pt prepared via the co-IWI method. It is obvious that the preparation method has a direct effect on the interaction between Pt and Co and that can be exhibited from the XRD profile especially

in low wt loading of Pt. The formation of $CoPt_3$ might be inactive for CO hydrogenation reaction; therefore, it might not be efficient to synthesize catalysts with a high amount of Pt by which a $CoPt_3$ alloy can be easily formed. In conclusion, the addition of Pt has a structural effect on the Co nanoparticles, decreasing the apparent Co particle size.

Table 3.2: Co and Pt species particles size of Pt-Co/SiO_2 sequential IWI + SEA

Pt/Co atomic %	Co_3O_4	CoO	Co(FCC)	Co(HCP)	CoPt3
0 .0 (Co/SiO_2)	5.26	6.1			
0.03	3.66	4.26			
0.08		2.87		3.2	5.5
0.23			4.1	2.3	8.5
0.74			2.6	2.2	15
1.72			2.6	2.1	15

Table 3.3: Co and Pt species particles size of Pt-Co/SiO2 simultaneous IWI

Pt/Co atomic %	Co_3O_4	CoO	Co(FCC)	Co(HCP)	CoPt3
0 .0 (Co/SiO_2)	5.26	6.11			
0.03	3.57	3.34		2.68	
0.23		3.45	4.69	3.8	
1.72		3.56	2.9	4.38	22.01

The TPR peaks of un-promoted and promoted Co based catalysts for Pt-Co/SiO_2 sequential IWI + SEA and Pt-Co/SiO_2 simultaneous IWI are shown in Figure 3.5 and 3.6, respectively. In unpromoted Co/SiO_2, H_2 consumption peaks are shown at temperatures of 230, 370, 560 and 745ºC. The first relatively sharp peak at low temperature is attributed to the reduction of Co_3O_4 to CoO. This has been reported in several studies on Co reduction

profiles [73], [123-124]. The CoO species usually reduce at higher and various temperatures, which might be attributed to the different reduction behavior of different nanoparticles' sizes of CoO. However, these reduction peaks are located between 370-560 ºC and represent the transition of CoO to Co metal phase. These reduction profiles, especially at high temperature, would be a powerful tool to get enough information about the interaction degree between Co and support. It is obvious that the Co^{+2} ion has more tendency to interact with oxide support ions.

Therefore, the replacement between the Co^{+2} ion and oxide support ions is more likely to take place among well-dispersed cobalt particles. In Pt-Co/SiO_2 sequential IWI + SEA production profiles, the addition of a minimum amount of Pt has significantly lowered the temperature of all Co-oxides species' reduction peaks. This shift is greatest at the higher reduction peaks at 745 ºC, which shifted to 680 ºC for Pt/Co atomic % at 0.03. But this shift to lower temperature is not significant with high Pt/Co atomic % samples and this is an indication that a small amount of Pt promoter would be sufficient to promote Co reduction. It is observed that the reduction of most of the Co^{+2} species was promoted and their reduction peaks are shifted to a temperature around 400 ºC. Another interesting observation is the appearance of a new low temperature peak, too large to be assigned to Pt reduction, and it is located at the lowest reduction temperature and might be attributed to the promotion of Co^{+3} reduction in the Co_3O_4 phase. In TPR profiles of Pt-Co/SiO_2 simultaneous IWI (Figure 3.6), the shift of the highest temperature reduction peak for the lowest Pt loading (at 750ºC) from the Pt free sample is observed to be less than the corresponding sequential IWI + SEA sample observed at 705ºC in Figure 3.5.

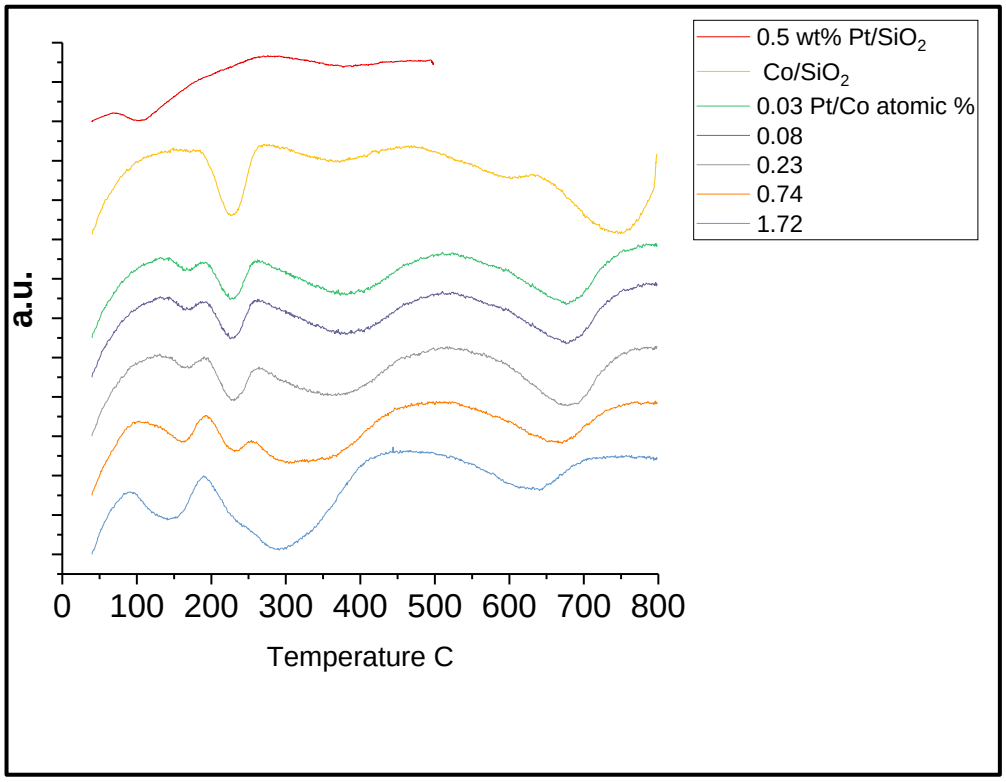

Figure 3.5: TPR profiles of Pt-Co/SiO_2 sequential IWI + SEA

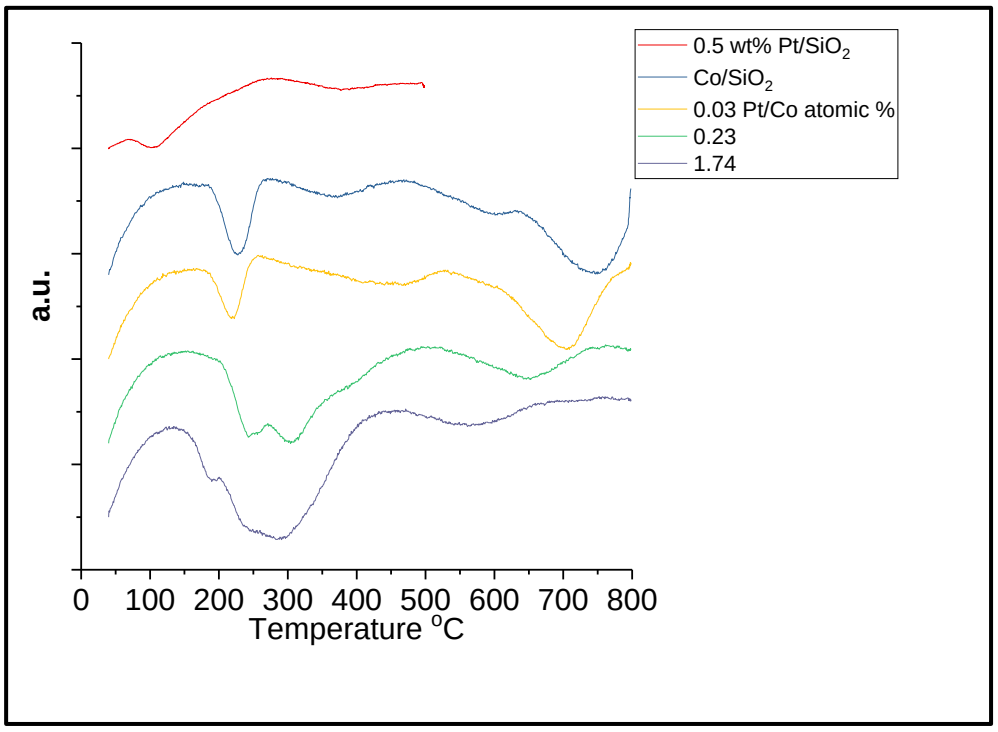

Figure 3.6: TPR profiles of Pt-Co/SiO2 simultaneous IWI

This is attributed to the fact that most Pt atoms in the co-IWI preparation method are not located as close to the Co oxides species. This contrasts the pH controlled selective deposition of Pt onto Co oxide, which gives intimate Pt-Co contact even at the lowest loadings.

Also for the low Pt loading co-IWI sample, the shift of the next higher reduction peak to 461 ºC, which represents the reduction of Co^{+2} species, is less compared to the sequential IWI + SEA catalyst with the lowest Pt loading. This lessening of the promotional effect of Pt in the lowest Pt loading can be attributed to the same reason mentioned previously for the hardest-to-reduce Co species. Also, the appearance of the low-temperature reduction peak in the sequential IWI + SEA catalysts is not seen in simultaneous IWI with the exception of the highest Pt loading (bottom profile of Figure 3.6).

This lowest temperature peak, which is attributed to the promotion of Co^{+3} species reduction, is surmised to require a high degree of contact between Pt and Co, and co-IWI does not provide this except at the highest Pt loading, where apparently some of the Pt randomly deposited on the cobalt oxide phase.

The un-promoted and promoted catalysts for both catalyst sets were tested under realistic conditions of the Fischer-Tropsch reaction at a gas hourly space velocity of 5100 ml/($g_{catalyst}$·hr). More information about the flow reactor system was provided in the material and method section in this chapter. The activity and selectivity were measured for each catalyst after the reaction had attained steady state at about 48 hours on stream.

The CO conversions of both catalyst sets are presented in Figure 3.7. Table 3.4 and Table 3.5 present the TOF (10^{-3} s^{-1}) and CTY (10^{-5} $mol_{CO} \cdot g_{Co}^{-1} \cdot s^{-1}$) for both sets of catalysts.

Table 3.4: TOF and CTY of Pt-Co/SiO_2 sequential IWI + SEA

Pt/Co atomic %	TOF (10^{-3} s^{-1})	CTY (10^{-5} $mol_{CO} \cdot g_{Co}^{-1} \cdot s^{-1}$)
0 .0 (Co/SiO_2)	40.2	7.9
0.03	24.0	7.2
0.08	16.0	6.5
0.23	11.2	5.1
0.74	9.9	4.5
1.72	7.0	3.2

Table 3.5: TOF and CTY of Pt-Co/SiO_2 simultaneous IWI

Pt/Co atomic %	TOF (10^{-3} s^{-1})	CTY (10^{-5} $mol_{CO} \cdot g_{Co}^{-1} \cdot s^{-1}$)
0.03	8.6	2.89
0.23	13.12	3.58
1.72	12.9	4.5

The CO conversion, TOF, and CTY are higher for the unpromoted Co/SiO_2 catalyst than all Pt promoted Co catalysts in both sequential IWI + SEA and simultaneous IWI sets. This is attributed to the known decrease in activity with Co particle size (Figure 3.1); XRD in Figure 3.5 and 3.6 show that the CO domain size decreases with increasing Pt content (and Tables 3.2 and 3.3).

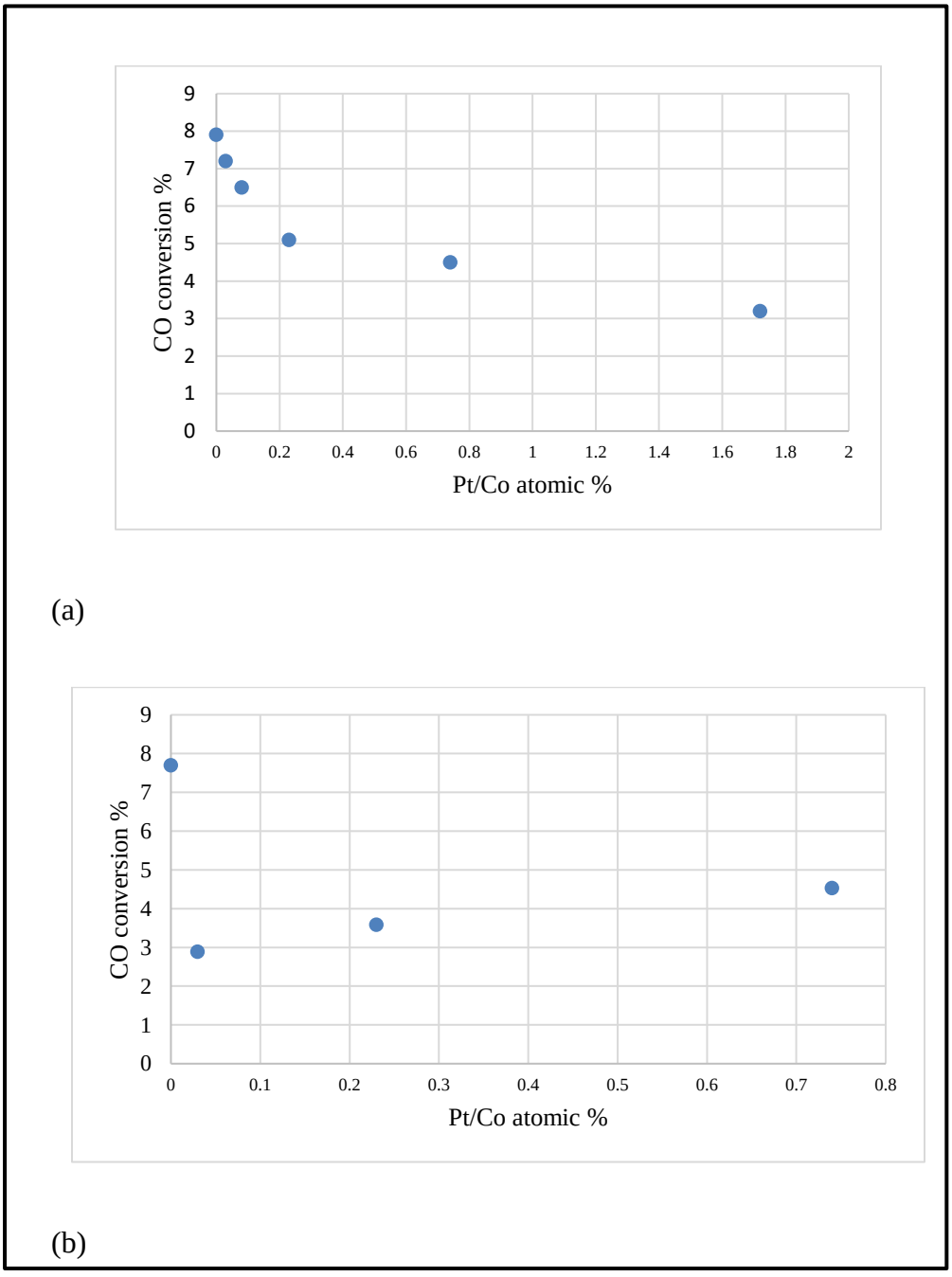

Figure 3.7: CO conversion % for (a) Pt-Co/SiO_2 sequential IWI +SEA (b) Pt-Co/SiO_2 simultaneous IWI

Hydrocarbon selectivity including C_1, C_{2-4}, and C_{5+} are presented in Figure 3.8 for both catalyst sets.

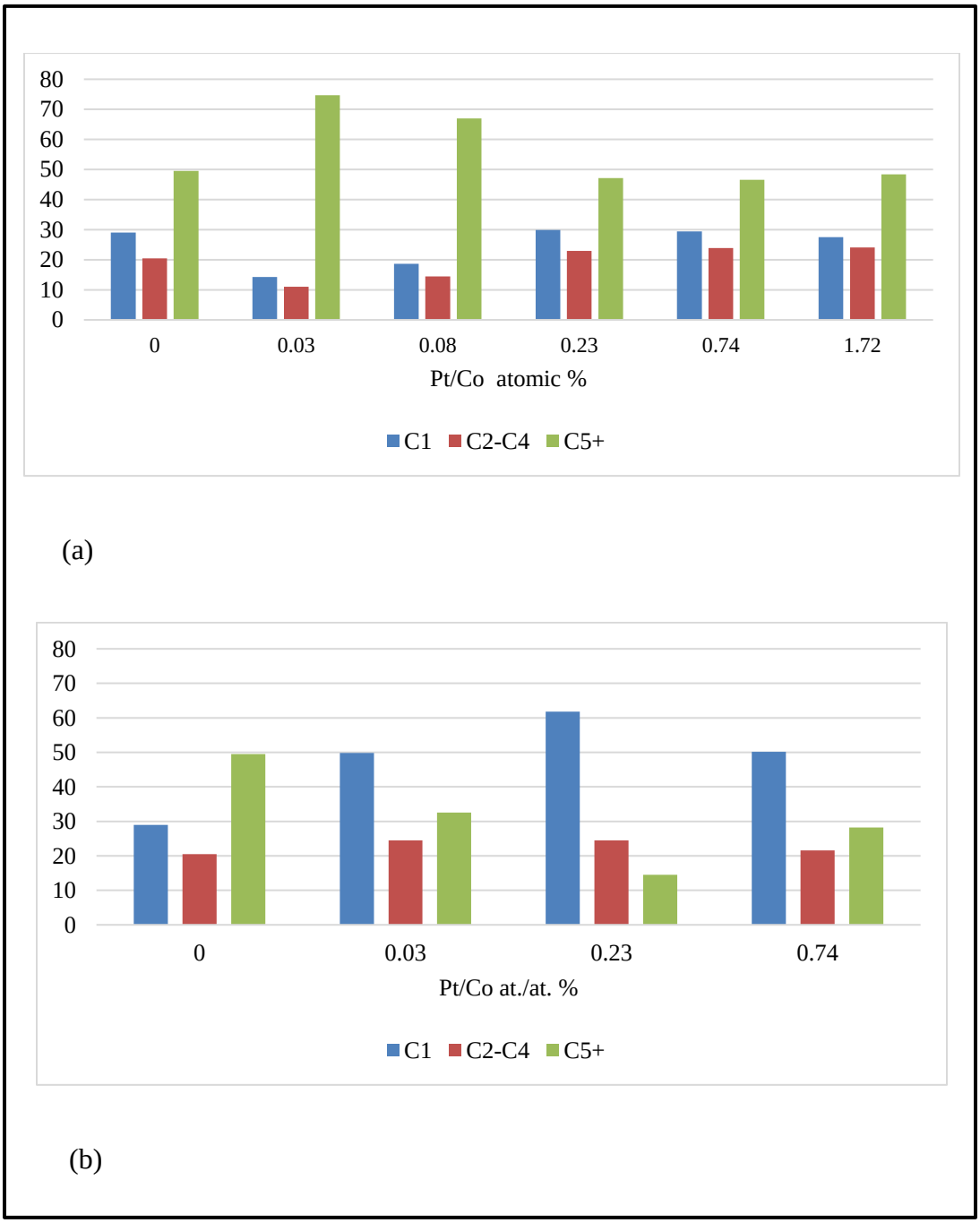

Figure 3.8: Hydrocarbon selectivity (a) Pt-Co/SiO_2 sequential IWI +SEA (b) Pt-Co/SiO_2 simultaneous IWI

The hydrogenation of hydrocarbon is presented in olefin/paraffin ratio and shown in Figure 3.9.

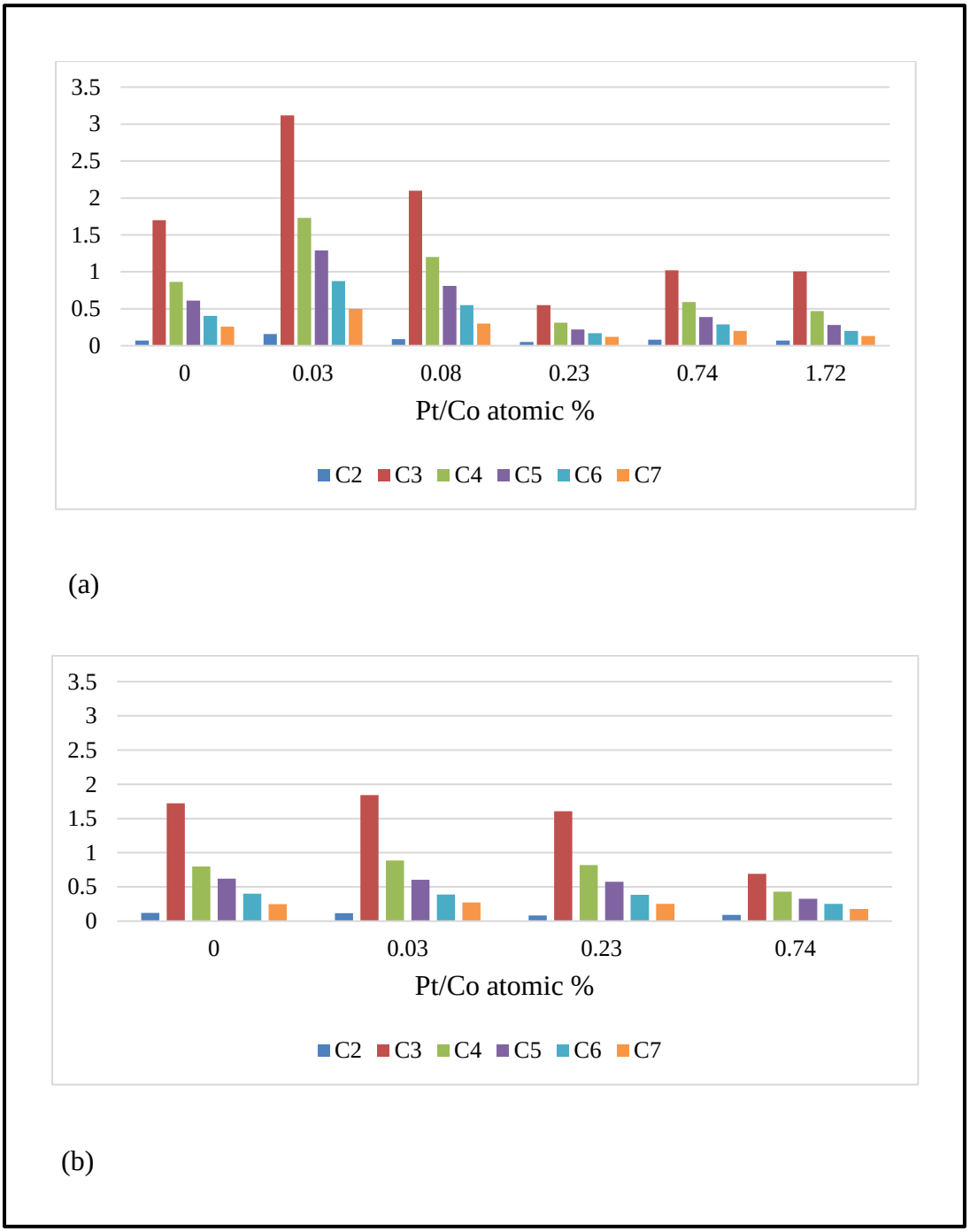

Figure 3.9: Olefin/Paraffin ratio for hydrocarbons of (a) Pt-Co/SiO_2 sequential IWI +SEA (b) Pt-Co/SiO_2 simultaneous IWI

The decrease in activity was gradual and seems to be more controlled in sequential IWI +SEA catalysts, especially at low amounts of Pt. There is a drop in Co nanoparticles from approximately 6.5 nm for un-promoted Co catalysts to 2.3 nm, which has a strong effect on the catalysts' reaction performance; thus, it seems to be independent of the presence of Pt.

This is consistent with Bezemer et al. work which showed that the increase in CH_4 selectivity, decrease in C_{5+} selectivity, and decrease in activity were observed for Co particles smaller than 6-8 nm [63].

For the lowest Pt loading deposited by IWI + SEA there is approximately a 50 % increase in C_{5+} selectivity and a 50% decrease in methane selectivity compared to the unpromoted catalyst. This level of C_{5+} selectivity is unprecedented in the literate (see Table 3.6). Additional Pt loading in this series decreases C_{5+} and increases methane selectivity.

Performance enhancements at low loading of Pt were also seen by Montes et al. [125] to a lesser extent, where a small amount of Pt decreased the methane selectivity (by 40%, Table 3.6) and increased C_{5+} selectivity (by 14%).

Their Pt/Co atomic % is higher than those in our study. Most other studies of the catalytic activity of bimetallic Pt-Co for FTS have shown increases in catalyst activity and methane selectivity (Table 3.6); they have usually employed a non-selective deposition by co-impregnation, with relatively higher Pt/Co atomic % [126-128].

In Pt-Co/SiO_2 simultaneous IWI catalysts, a decrease in catalysts activity is associated with the presence of Pt of any amount, with higher CH_4 and lower C_{5+} selectivity as is usually observed.

The degree of hydrocarbon hydrogenation can be presented in the olefin/paraffin ratio which exhibits an improvement by rationally adding Pt onto Co using SEA in a small amount (Figure 3.9).

Otherwise for high loading and unselective deposition of Pt, these ratios decreased. This indicates a high hydrogenation rate, likely caused by a separate Pt catalytic function, which increases paraffin production and consequently decreases the olefin/paraffin ratios. However, we designed Co/SiO_2, the starting material for our synthesis of sequential IWI + SEA, at the optimum Co particle size of 6.5 nm.

Therefore, any size reduction would cause a decrease in catalyst activity and C_{5+} selectivity and an increase in CH_4 selectivity as observed in many studies and that was previously mentioned.

But using SEA with a very small amount of Pt significantly improved the catalyst performance without introducing a Pt function, that is, without introducing increased hydrogenation during the FT reaction. At low loadings the function of Pt would then appear to be that of increasing the extent of Co reduction, and so increasing the number of active sites 125-126] & [128-133].

Table 3.6: FT activity and hydrocarbons selectivity comparisons

Co wt.%	Pt/Co at. %	FT conditions	Conv.%	CO_2	C_1	C_2-C_5	C_5+
15	0.0	• 1 bar. • 190 C • GHSV 1800 cm^3	$2.7^{(un)}$	--	6.5	13.8	79.8
	0.2		$19.3^{(pro)}$		9.6	18.4	72.1
15	0.0	• 20 bar. • 230 C • GHSV 900 cm3	60	2.8	14.8	2.6	82.6
	1.05		81.6	9.6	17.1	3.3	79.6
12	0.0	• 20 bar. • 210 C	2.1	2.61	21.2	12.2	64
	0.25		11.7	0.18	12.8	13.8	73
	0.63		17	0.23	13.4	13.9	72
9.8	0.0	• 20 bar. • 220 C	29.2		6.3		85
	0.34		30.4		7.6		83
	0.65		30		8.3		84
	1.2		34.2		7.3		83
10	0.0	slurry-phase reactor • 10 bar. • 240 C	33.5	1.27	8.89	--	--
	0.6		49.5	9.48	13.78	--	--
10	0	Packed bed reactor • 20 bar. • 220 C	21.4	1	6	8	84.7
	0.3		66.3	2	7	7	85
	0.75		66.6	3	6	8	85
	1.5		68.7	3	7	8	82
	6.04		63.9	6	9	8	74
20	0	Packed bed reactor • 20 bar. • 220 C • 2400 ml(min gCal)$^{-1}$	9.5		21	--	65
	0.76		19		30	--	57
12	0	Fixed bed reactor • 20 bar. • 230 C	6.4	0	27.5	20.3	52.2
	1		61.3	9.1	15.6	7.9	67.4
10	0	Our Fixed bed reactor • 20 bar. • [this study] • Pt-Co sequential IWI+SEA • Pt-Co simultaneous IWI • 230 C • GHSV 5800	7.9		29	20.4	49.5
	0.03		7.2		14.2	11.0	74.6
	0.08		6.5		18.6	14.5	67
	0.23		5.1		29.9	22.8	47.1
	0.74		4.5		29.4	23.9	46.6
	1.72		3.2		27.5	24.1	48.4
10	0		7.9		29	20.4	49.5
	0.03		2.8		49.8	24.5	32.5
	0.23		3.5		61.8	24.5	14.5
	1.72		4.5		50.2	21.6	28.2

3.4. Conclusion

A well dispersed Co/SiO_2 catalyst was prepared by citrate-modified IWI to produce Co nanoparticles at the optimum size for the FT reaction. In both $Pt/Co/SiO_2$ sequential IWI + SEA and simultaneous IWI catalysts sets, the Pt has a strong structural effect on Co which was detected by XRD and a noticeable decrease in Co nanoparticle size which is correlated with the amount of Pt. Cobalt reduction was enahnced at low temperatures by the selective depostion of platinum onto cobalt. The very smallest amount of Pt had significant promotional effect on the hardest-to-reduce Co species, and shifted more when Pt was deposited onto Co by SEA. A similar observation of minimum Pt addition was seen for Co^{2+} species reduction and improved more with the SEA mechanism of Pt adsorption on Co/SiO_2. At the higher amount of Pt deposition on Co/SiO_2, the differentiation between synthesis methods is not significant, which is attributed to lesser control of Pt onto Co_3O_4 oxide during the synthesis procedure and thermal treatment. The catalyst activity for both $Pt\text{-}Co/SiO_2$ catalysts sets were decreased by adding Pt and that is attributed to a strong structural effect of Pt on Co particles which results in a reduction in Co nanoparticle size. Consequently, a decrease in catalysts' activity was observed for all Pt-promoted catalysts but this can be minimized by limiting the amount of Pt. The high hydrogenation rate during the FT reaction was observed when Pt deposition onto Co/SiO_2 was uncontrolled or overabundant, and that occurs at a high Pt/Co atomic % in sequential IWI + SEA and all Pt loadings in simultaneous IWI catalysts.

CHAPTER 4

CHARACTERISTICS AND CATALYTIC ACTIVITY OF PLATINUM-PROMOTED IRON-BASED CATALYSTS

4.1. Introduction

Interest in alternative energyis based on biomass has gained a lot of attention to reduce the world's fossil fuel demand and provide a sustainable and secure source of energy. Another source of energy, coal, can be used in Fischer-Tropsch synthesis and is abundant compared to other sources. Co-based catalysts are not used in Coal-to-Liquid and Biomass-to-Liquid Fischer Tropsch due to deficient H_2 in the feedstock which requires a Water-Gas-Shift (WGS) reaction to modify the H_2/CO ratio before syngas is introduced to the FT reactor. Despite relatively low activity and stability in the FT reaction compared to Co, iron-based catalysts can provide an advantage in CTL and BTL technologies due to the high activity of WGS reaction along with CO hydrogenation; as a result the catalysts tolerate various H_2/CO ratios. Despite the cheap price of Fe, the catalysts suffer from low activity and less lifetime compared to Co-based catalysts. Therefore, many studies focused on improving the catalyst's performance for a FT reaction. Different promoters have been used in Fe-based catalysts such Cu, K, and Mn [134-136].

Each promoter has provided a different effect on Fe-based catalysts such as an enhancement of the degree of reduction, increased CO hydrogenation activity, and modified hydrocarbons distribution during the FT reaction. In addition, these parameters improve Fe metal phase transition to Fe carbides which are widely thought of as the active phase for CO hydrogenation reaction [137-138]. The main challenge of Fe-based catalyst design and synthesis is the avoidance of strong interaction between Fe and support which mostly results in attrition in the catalyst's reducibility. A decoration of Fe nanoparticles with species of support such alumina or silica is another common consequence of the interaction between Fe and the support. Therefore, ineffective synthesis methods result in catalysts with poor reduction quality and low catalytic performance.

There is a debate on determining the active site of iron-based catalysts and this would be a major consideration in iron-based catalyst design and synthesis. The instability of the Fe metal phase during the FT reaction and the ease of transition to iron-carbide are the main reasons in support that the Fe-carbide is the active phase for CO hydrogenation. As discussed in Chapter 2, there are various kinds of Fe-oxides, -carbides and metal phases which makes it hard to determine which phase is active [139]. Usually, the reduction of α-Fe_2O_3 under H_2 leads to the formation of α-Fe, and then this species of the Fe metal phase would transform to different Fe-carbides during the FT reaction. As mentioned in Chapter 2, H_2 and CO can reduce Fe-oxide species into different Fe-metal or Fe-carbides species; therefore, the environment of gases and its condition could determine the final structure of the Fe species. However, using the noble

metal promoter Pt in literature is very limited and that is ascribed to a complexity in transitions between Fe-oxides, Fe-metal, and carbides species during reduction.

In this study, we introduced Pt as a promoter to study its effect on iron-based catalyst reducibility; we observed its reaction performance at similar conditions to the Co-based catalysts reported in Chapter 3. We synthesized two sets of catalysts analogous to our study on Co/SiO_2 in Chapter 3 and more synthesis details were described in Chapter 2.

4.2. Methods and materials

First, the monometallic silica-supported iron oxide was prepared using citrate-modified incipient wetness impregnation by dissolving iron nitrate ($Fe(NO_3)_3 \cdot 9H_2O$) and citric acid (mole/mole ratio) in a volume of deionized water corresponding to the pore volume of silica support. Similar weight % in the cobalt-based catalyst was used for iron which is 10 wt. % with similar procedure of IWI and drying, but the calcination was conducted at 275 ºC for 5 hours. Similar procedures to the $Pt\text{-}Co/SiO_2$ sequential IWI + SEA catalysts preparation were followed for the $Pt\text{-}Fe/SiO_2$ sequential IWI and SEA method with a similar variation of Pt concentration from 200-30 ppm except for the final pH. The final optimum pH, which was determined by uptake survey on Fe/SiO_2 was 3.4. The weight loading of Pt was calculated by conducting the ICP measurement for CPA solution pre- and post-contact with Fe/SiO_2. Then, all samples were dried at room temperature for 48 hours and heated at 100 ºC for 2 hours, before conducting a TPR experiment to investigate the reduction profile of $Pt\text{-}Fe/SiO_2$ catalysts. A similar procedure to $Pt\text{-}Co/SiO_2$ simultaneous IWI was conducted for $Pt\text{-}Fe/SiO_2$ preparation. Thus both metal precursors, platinum tetraammine chloride and iron nitrate hydrate, were dissolved

in DI water with amounts that corresponded to metal weight loadings in the first series of Pt-Fe/SiO_2 that used two procedures of preparation, IWI + SEA. Then, samples were dried for two nights at ambient temperature and calcined in the muffle furnace at 275 ºC for 5 hours. However, similar characterization techniques and reaction test procedures to cobalt catalysts were chosen for iron catalysts except the reaction was conducted at 250ºC.

4.3. Results and discussion

Results from Pt adsorption onto Fe/SiO_2, including Pt wt.% loading and Pt/Fe atomic % are presented in Table 4.1. The variation of Pt uptake onto Fe/SiO_2 for different initial concentrations of Pt, 200 -30 ppm, was not significant at 1000 m^2/L surface loading; therefore, we conducted three additional SEA experiments, two of them at initial Pt of 50 ppm and one at initial Pt of 30 ppm, at a higher surface loading of 3K, 10K, and 15K, respectively. We assumed there is no uptake on SiO_2 based on the STEM-EDXS result in Chapter 2 for Pt uptake on a physical mixture of oxides (SiO_2+Fe_2O_3) and Pt-Fe/SiO_2 sequential IWI+SEA catalysts. By varying the initial concentration of Pt we were able to produce a diverse weight loading of Pt, from the maximum at 1.14 % to the minimum at 0.009 %. The corresponding range of Pt/Fe atomic % is from 3.23 to 0.03, but for the reaction experiment, we excluded the highest Pt/Fe atomic % due to similar characteristics and catalytic performance of Pt/Fe atomic % at 1.72 and 3.23. Another series of samples were prepared by co-incipient wet impregnation, or simultaneous Pt-Fe IWI, and have Pt/Fe atomic %s similar to Pt-Fe/SiO_2 sequential IWI +SEA catalysts as shown in Table 4.1. It should be mentioned that the amount of iron is fixed in all samples as originally prepared at 10 wt. %. The amount of Fe has also been kept the same for Pt-Fe/SiO_2 simultaneous-IWI catalysts. Both series of catalysts, Pt-Fe/SiO_2 sequential IWI + SEA

Both series of catalysts, Pt-Fe/SiO_2 sequential IWI + SEA and Pt-Fe/SiO_2 simultaneous IWI have been calcined at 275 ºC for 5 hours and the TPR first conducted to determine the optimum temperature for thermal reduction treatment of catalysts. All samples were reduced at 650 ºC in 10% H_2/He for 4 hours and XRD was conducted for reduced samples and is shown in Figures 4.1 and 4.2 for Pt-Fe/SiO_2 sequential IWI + SEA and Pt-Fe/SiO_2 simultaneous IWI, respectively.

Table 4.1: Pt weight loading and Pt/Fe atomic % based on SEA uptake onto Fe/SiO2

Initial Pt Conc. (ppm)	Surface Loading (m^2/L)	Pt uptake μmol/m^2	Pt/Fe atomic %
200	1000	0.84	3.23
100	1000	0.44	1.72
50	1000	0.19	0.74
50	3000	0.06	0.23
30	10000	0.02	0.08
30*	15000	0.007	0.03

The XRD patterns in Figure 4.1 showed the Fe metallic diffraction peak at 44.6º and it is relatively broad at the lower Pt loadings. By using Scherrer equation, the Fe particle size is calculated at 6.6 nm. However, the peak is slightly shifting to a higher degree and becoming sharper with the increasing the amount Pt. These XRD profiles of sequential IWI + SEA Pt-Fe catalysts verified the intimate interaction between Fe and Pt. It is expected that the shift of the peak at 44.6º results from the formation of Pt-Fe alloy, which, in effect, has various structures. This alloy is more vulnerable to sintering based on the amount of Pt content in the catalysts [139]. For Pt-Fe co-IWI reduced catalysts, XRD profiles show no noticeable shift, which implies that the interaction between Pt and Fe is not strong enough to form a Pt-Fe alloy structure even at a high Pt/Fe atomic %.

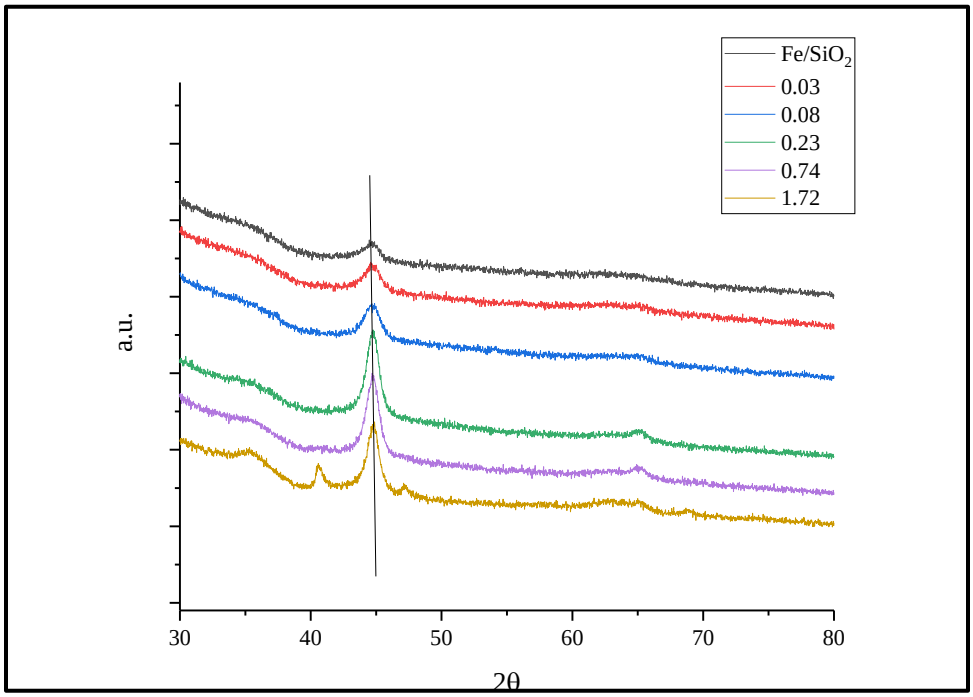

Figure 4.1: XRD profiles of Pt-Fe/SiO_2 sequential IWI +SEA catalysts

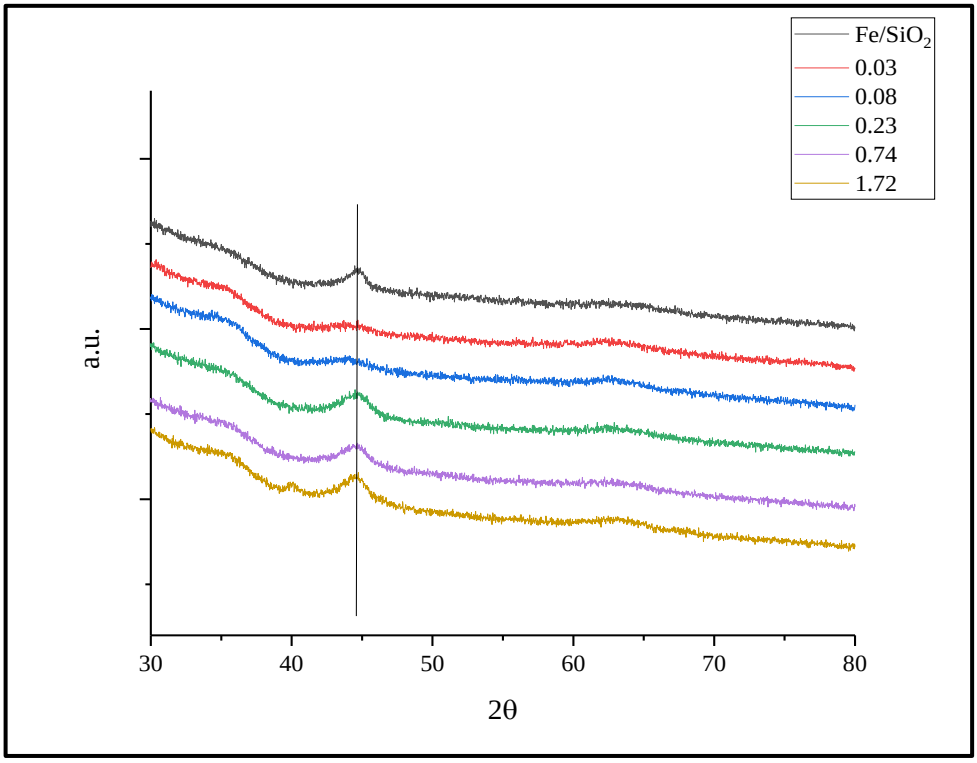

Figure 4.2: XRD profiles of Pt-Fe/SiO_2 simultaneous IWI catalysts

It was reported that the reduction of Fe oxide species is following α-$Fe_2O_3 \rightarrow Fe_3O_4 \rightarrow FeO \rightarrow \alpha Fe$. This transformation consists of various species of iron oxide which can be represented by different reduction peaks in Figure 4.3. In the monometallic Fe/SiO_2 reduction profile, broad peaks were observed and may be attributed to a reduction of more than one iron oxide species at very close temperatures. The unstable FeO species is the last one that is reduced to the Fe metal phase and it is strongly dependent on the interaction with the support. Therefore, the last reduction peak is attributed to the reduction of FeO to the Fe metal phase at a temperature of 660 ºC. The addition of Pt using SEA slightly shifted the FeO species reduction peak to a lower temperature, and it is shifted more with the addition more Pt to the Fe-based catalyst. This shift is associated with increases in peak intensity, which might be attributed to the diminishing of one of the Fe-oxide species during the reduction transformation, but it is more complex to determine which species would be eliminated during reduction transformation of Fe-oxides species. The other low-temperature reduction peaks of other Fe-oxides species are not showing a significant change in their reduction behavior. The second catalysts set of simultaneous IWI catalysts showed a different TPR profile from the first set. In these TPR profiles, all reduction species are shifted to a lower temperature and all of them are correlated to the amount of Pt. This is attributed to a different interaction that was established between Pt and Fe in simultaneous IWI, which improves the reduction of all Fe-oxides species. The random interaction between Pt and Fe results in the creation of new reduction peaks, and this might be attributed to the presence of new Fe-oxides species that tend to reduce at a different

temperature, which is more profound in high Pt/Fe atomic %. This significant difference in reduction peaks is still not understood [141].

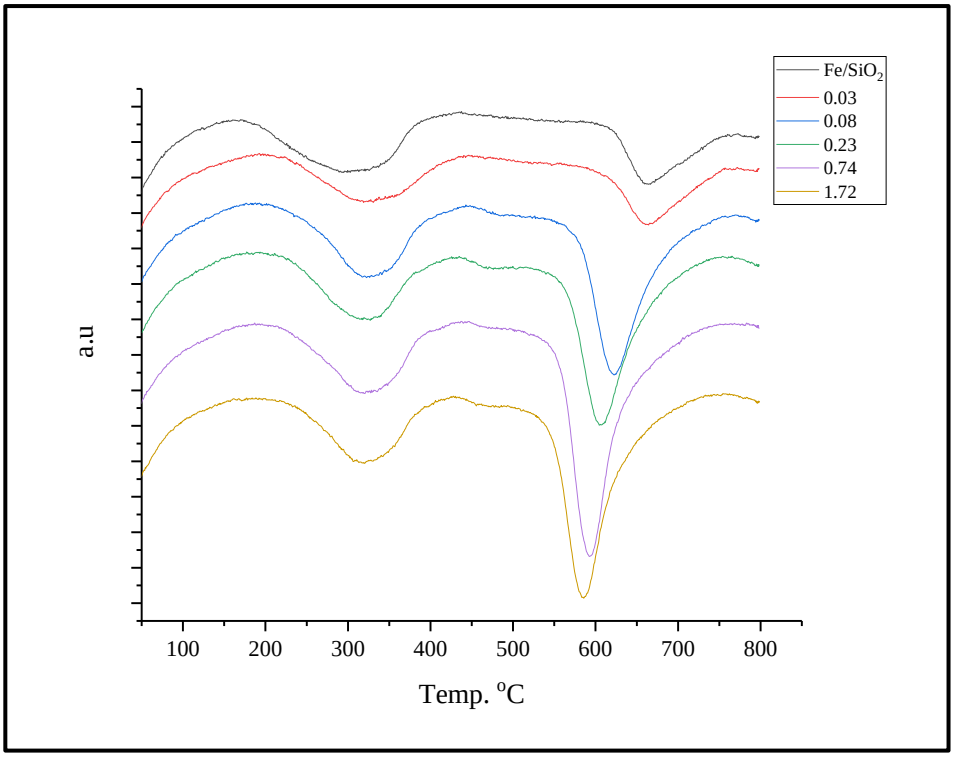

Figure 4.3: TPR profiles of Pt-Fe/SiO_2 sequential IWI + SEA

The CO conversion as a function of Pt/Fe atomic % is plotted in Figure 4.5a for the IWI + SEA series and Figure 4.5b for the co-IWI series. In most promoted catalysts of the Pt-Fe/SiO_2 sequential IWI + SEA set, the CO conversion increased compared to the unpromoted Fe/SiO_2 CO conversion, except for the minimum Pt content, where there is a slight decrease in CO conversion compared to the unpromoted one.

The CO conversion of the co-IWI series is roughly independent of Pt content. The effect of Pt in both series is most clearly seen in the higher olefin to paraffin ratios (Figure 4.7) of essentially all Pt containing catalysts of either set (which are also curiously all about

the same value) as well as selectivity to CO_2 which increasing proportionately with Pt content (Figure 4.8) with the exception of the highest Pt loading.

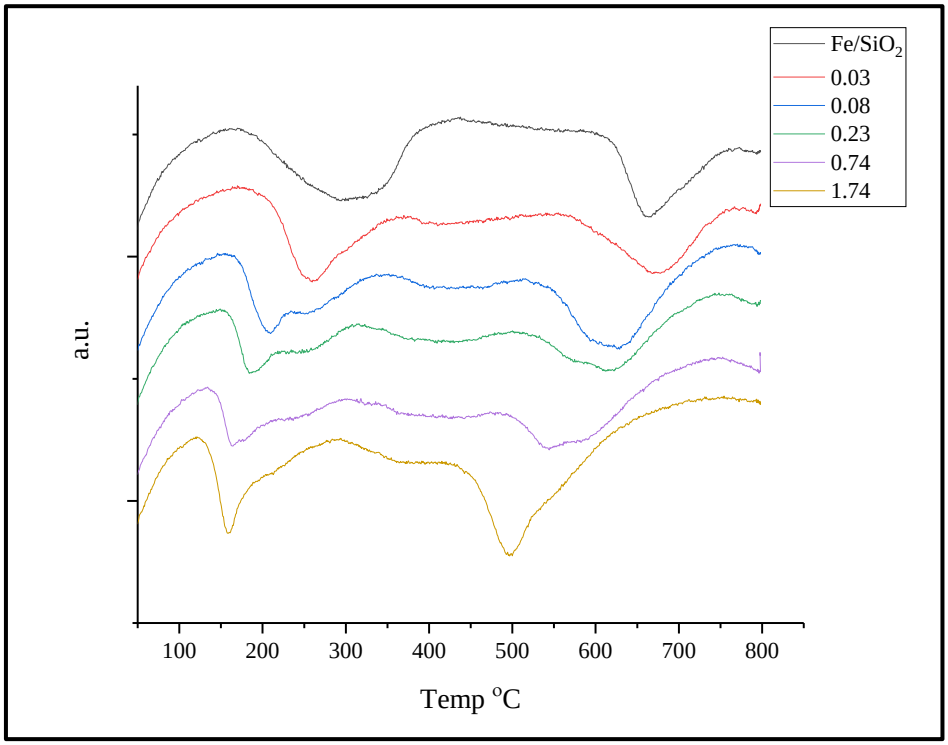

Figure 4.4: TPR profiles of Pt-Fe/SiO_2 simultaneous IWI

The selectivity of the catalysts is also relatively unchanged by the addition of Pt for either set, with the exception that the lowest Pt loading of the IWI + SEA catalyst gives significantly more methanol, while all other IWI + SEA and co-IWI catalysts give less methanol than the Pt-free catalyst. These attributes are consistent with the notion that the active sites in iron catalysts are iron carbides, and not reduced iron. Both sets of TPR data in Figures 4.3 and 4.4 show enhanced reduction with increased Pt loading, but this is not reflected at all in the selectivity trends. Table 4.2 and 4.3 summarize the TOF and FTY for both Pt-Fe/SiO_2 sequential IWI + SEA and simultaneous IWI sets.

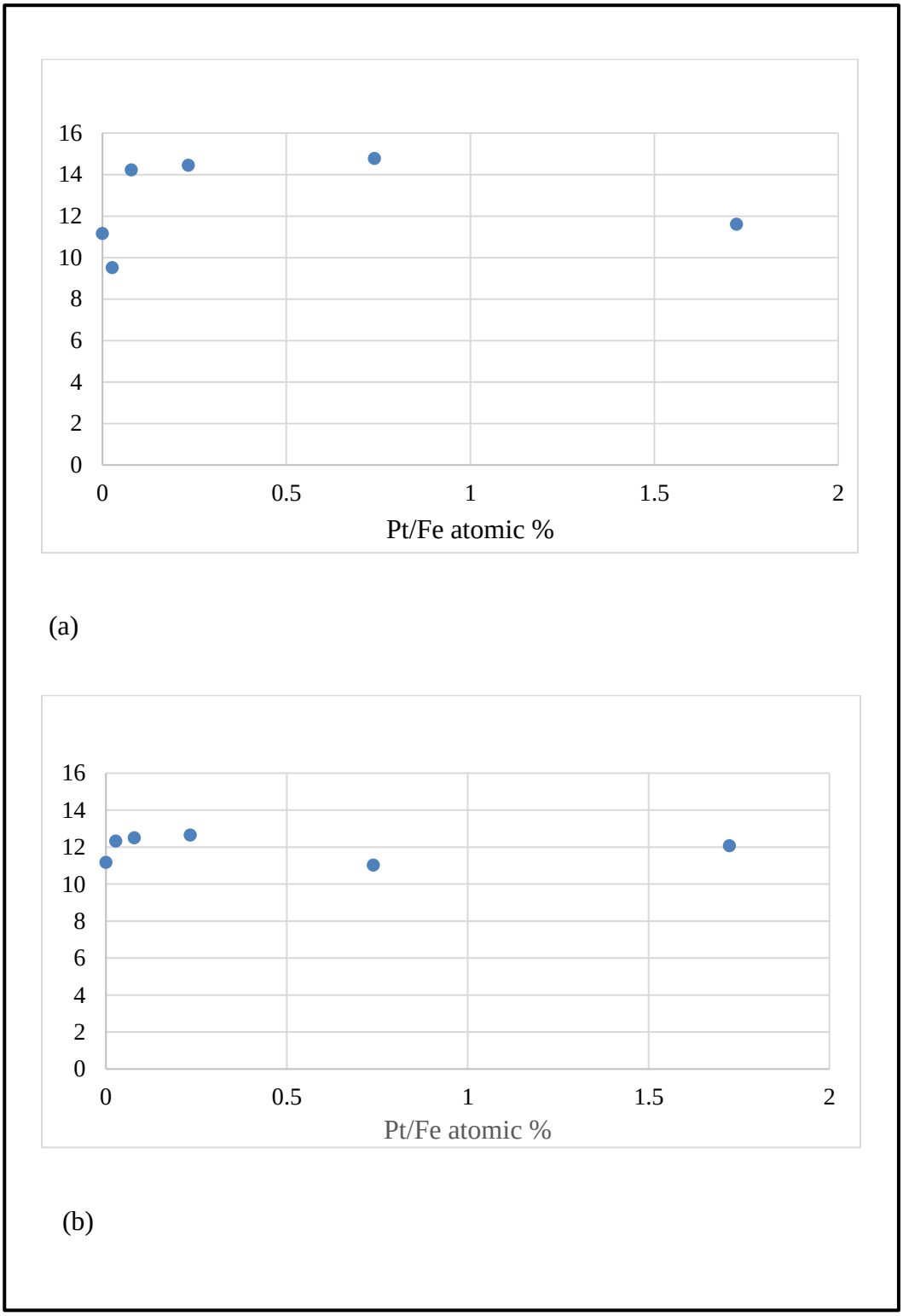

Figure 4.5: CO conversion % for (a) Pt-Fe/SiO_2 sequential IWI +SEA (b) Pt-Fe/SiO_2 simultaneous IWI

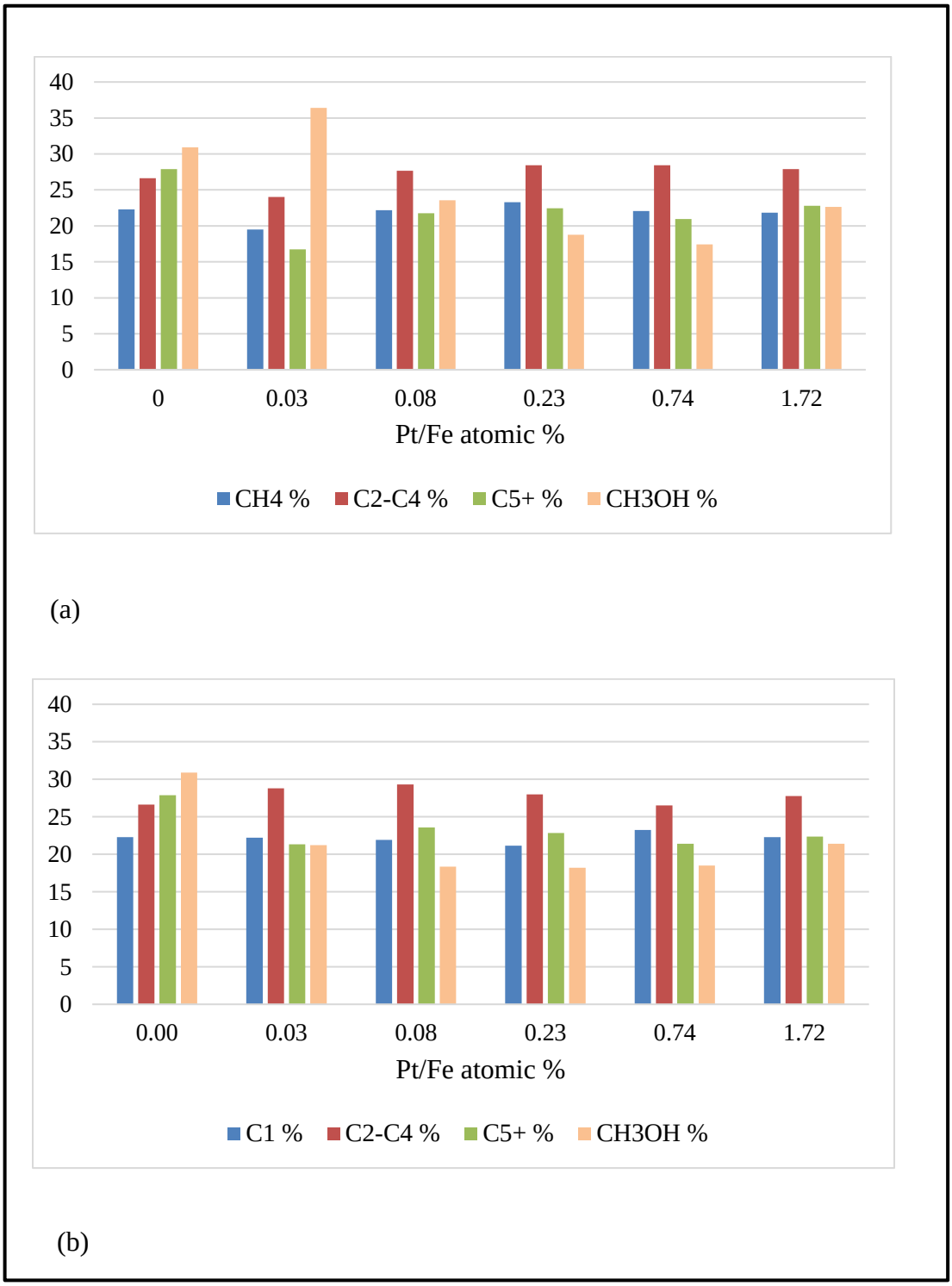

Figure 4.6: Hydrocarbon selectivity (a) Pt-Fe/SiO_2 sequential IWI +SEA (b) Pt-Fe/SiO_2 simultaneous IWI

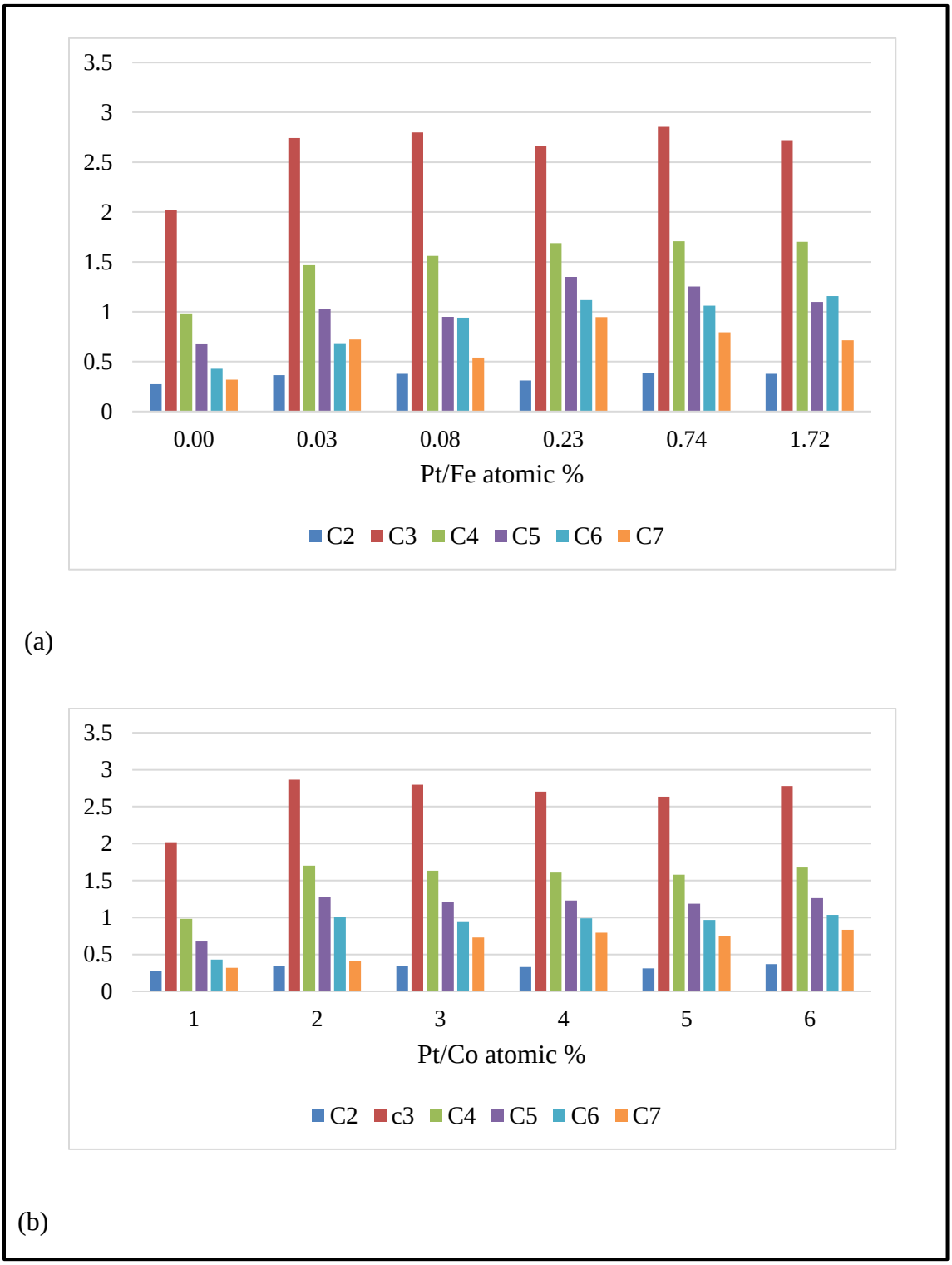

Figure 4.7: Olefin/Paraffin ratio for hydrocarbons of (a) Pt-Fe/SiO_2 sequential IWI +SEA (b) Pt-Fe/SiO_2 simultaneous IWI

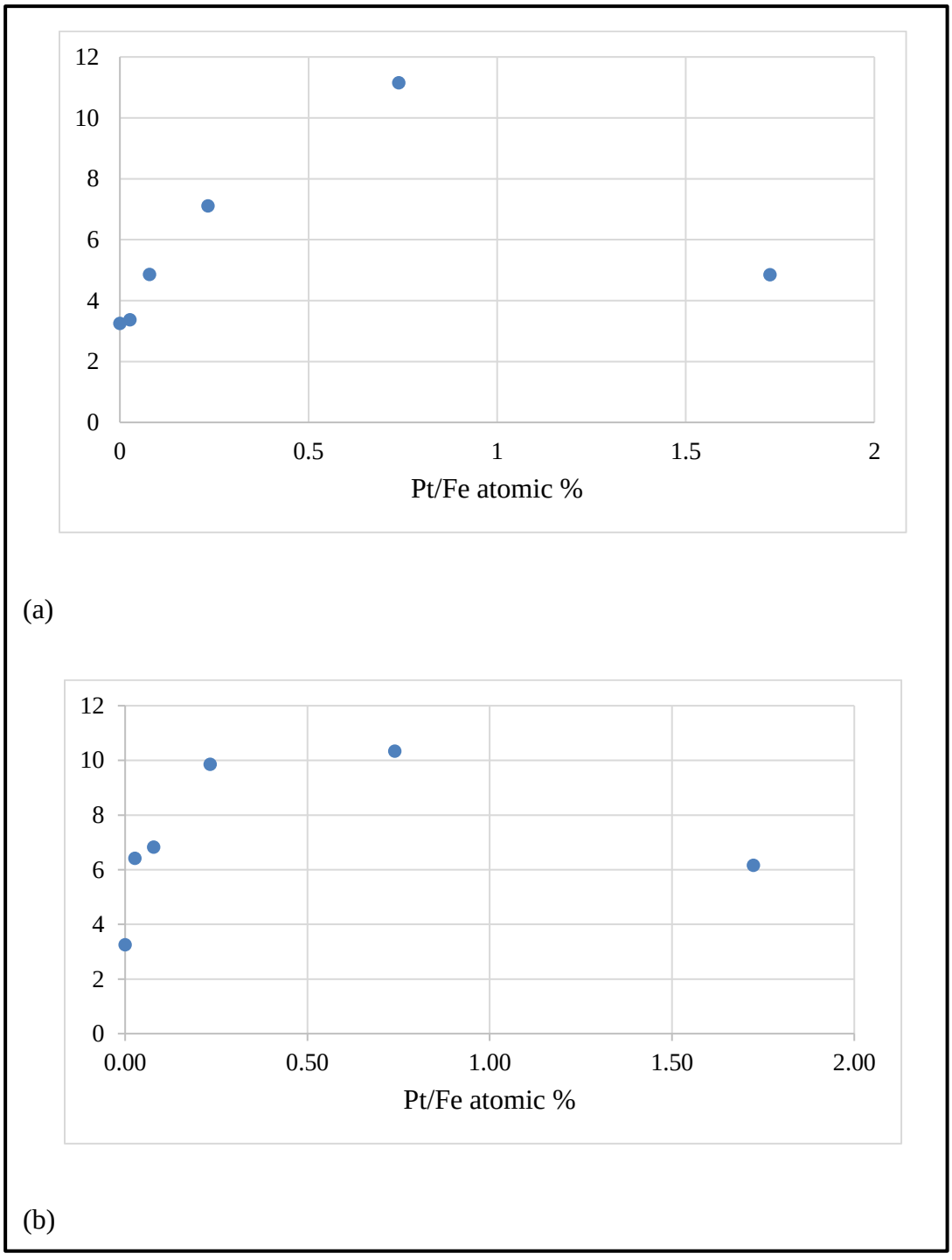

Figure 4.8: CO_2 selectivity for (a) Pt-Fe/SiO_2 sequential IWI +SEA (b) Pt-Fe/SiO_2 simultaneous IWI

Table 4.2: TOF and FTY of Pt-Fe/SiO_2 sequential IWI + SEA

Pt/Fe atomic %	FTY (10^{-5} $mol_{CO} \cdot g_{Fe}^{-1} \cdot s^{-1}$)	TOF (10^{-3} s^{-1})
0 .0 (Fe/SiO_2)	3.1	5.9
0.03	2.7	5.4
0.08	4.1	8.5
0.23	4.1	9.1
0.74	4.2	10.2
1.72	3.3	9.0

Table 4.3: TOF and FTY of Pt-Fe/SiO_2 simultaneous IWI

Pt/Fe atomic %	FTY (10^{-5} $mol_{CO} \cdot g_{Fe}^{-1} \cdot s^{-1}$)	TOF (10^{-3} s^{-1})
0.03	3.5	2.2
0.08	3.6	2.5
0.23	3.6	5.0
0.74	3.2	4.7
1.72	3.4	5.3

There was a significant increase in TOF for Pt-Fe/SiO_2 sequential IWI + SEA catalysts that appears to be indirectly related to Pt content, as the Fe particle size increases with increasing Pt content as seen in the sharper XRD peaks at higher Pt loadings in Figure 4.1. The FTY was relatively unaffected by the amount of Pt in this series. For the Pt-Fe/SiO_2 simultaneous IWI catalysts, TOF also increased considerably, to 5.0×10^{-3} s^{-1} at a Pt/Fe atomic % of 0.23, which is again related to the increased particle size of the higher Pt loadings (sharper Fe peaks in Figure 4.2) while FTY was again unaffected by the amount of Pt. The effect of Pt on the selectivity of the catalyst is much less than the Co-based catalysts.

4.4. Conclusion

The Pt content in Pt-Fe sequential IWI + SEA catalysts was precisely controlled by varying the preparation parameters of pH, Pt precursor concentration, and support surface loading. Pt/Fe atomic ratios similar to the IWI + SEA samples were used for simultaneous IWI catalyst preparation. The deposition of Pt onto Fe/SiO_2 catalysts using SEA has a strong structural effect that resulted in the new formation a Pt-Fe alloy clearly seen in XRD whose particle size correlated with the amount of Pt content. This effect on alloying was not seen on Pt-Fe simultaneous catalysts, which is attributed to the lack of Pt selective deposition using the co-impregnation method.

The reduction behavior of Pt-promoted Fe-based catalysts is affected by both synthesis methods. A more pronounced effect was seen on the simultaneous IWI catalysts, for which all peaks occurred at lower temperature with increasing Pt content; sequential IWI + SEA catalysts exhibited enhanced reduction only of the high-temperature reduction species.

The conversion of both sets of catalysts was not strongly affected by Pt loading, while the TOF increased for both sets of catalysts which can be linked to the decrease in Fe particle size with increasing Pt content. The hydrocarbon selectivity is not strongly affected by Pt in both catalysts sets, except changes in methanol and C_{5+} selectivity for some catalysts, whereas the hydrogenation function was slightly changed as indicated by an increase in olefin/paraffin ratios. The CO_2 selectivity exhibited a similar volcano shape in both catalysts sets. In general, the use of Pt is more beneficial for Co-based catalysts compared to Fe-based catalysts, and that might be attributed to the active site in Fe-based

catalysts being Fe-carbide, the formation of which is not promoted by Pt. However, in Co-based catalysts, the reduced Co metal phase is expected to be the active phase and it can be strongly promoted by Pt.

REFERENCES

[1] International Energy Outlook 2017 (IEO2017).
[2] OPEC's World Oil Outlook 2017, launched in Vienna.
[3] CO_2 emissions from fuel combustion, (EIP2017).
[4] K. Ribeiro, S., S. Kobayashi, M. Beuthe, J. Gasca, D. Greene, D. S. Lee, Y. Muromachi, P. J. Newton, S. Plotkin, D. Sperling, R. Wit, P. J. Zhou, 2007: Transport and its infrastructure. In Climate Change 2007: Mitigation. Contribution of Working Group III to the Fourth Assessment Report of the Intergovernmental Panel on Climate Change [B. Metz, O.R. Davidson, P.R. Bosch, R. Dave, L.A. Meyer (eds)], Cambridge University Press, Cambridge, United Kingdom and New York, NY, USA.
[5] H. Engerer, U. Kunert, Gasoline and diesel will continue to dominate in the future of road transport, In Fuels Consumption in Road Traffic, DIW Economic Bulletin, 36 (2015) 469-477.
[6] M. E. Dry, High quality diesel via the Fischer-Tropsch process- a review, J Chem Tecchnol Biotechnol, 77 (2001) 43-50.
[7] A. M.K.P. Taylor, Science review of internal combustion engines, Energy Policy, 36 (2008) 4657-4667.
[8] R. Agrawal, N. R. Singh, F. H. Ribeiro,W. N. Delgass, Sustainable fuel for transport sector, PNAS, 104 (2007) 4828-4833.
[9] D. Leckel, Diesel Production from Fischer-Tropsch: The Past, the Present, and New Concepts, Energy Fuels, 23 (2009) 2342-2358.
[10] H. Schulz, Short History and present trends of Fischer Tropsch Synthesis, Applied Catalysis A: General, 186 (1999), 3-12.
[11] A. P. Steynberg, Chapter 1 – Introduction to Fischer-Tropsch Technology, Studies in Surface Science and Catalysis, 152 (2004) 1-63.
[12] A. C. Vosloo, Fischer-Tropsch: a futuristic view, Fuel Processing Technology 71 (2001) 149-155.
[13] L. P. Duncuart, A. P. Steynberg, Fischer-Tropsch based GTL Technology: A New Process? Studies in Surface Science and Catalysis, 163 (2007) 379-399.
[14] P. M. Maitlis, What is Fischer-Tropsch? In Greener Fischer-Tropsch Processes for Fuels and Feedstocks (eds P. M. Maitlis and A. de Klerk), (2013).
[15] E. G. Pereira, J. N. de Silva, J. L. de Oliveira, C. S. Machado, Sustainable energy: A review of gasification technology, Renewable and Sustainable Energy Reviews, 16 (2012) 4753-4762.
[16] M. E. Dry, Practical and theoretical aspects of the catalytic Fischer-Tropsch process, Applied Catalysis A: General, 138 (1996) 319-344.
[17] A. P. Steynberg, H. G. Nel, Clean coal conversion options using Fischer-Tropsch technology, Fuel, 83 (2004) 765-770.
[18] H. L. Chum, R. P. Overend, Biomass and renewable fuels, Fuel processing Technology, 71 (2001) 187-195.

[19] B. Sharma, R. G. Ingalls, C. L. Jones, A. Khanchi, Biomass supply chain design and analysis: Basis, overview, modeling, challenges, and future, Renewable and Sustainable Energy Reviews, 24 (2013) 608-627.
[20] J. M. Ebeling, B. M. Jenkins, Physical and Chemical Properties of Biomass Fuels, Transactions of the ASAE, 28 (1985) 898-902.
[21] N. Seifkar, X. Lu, M. Withers, R. Malina, R. Field, S. Barrett, H. Hezog, Biomass to Liquid Fuels Pathways: A Techno-Economic Environmental Evaluation, An MIT Energy Initiative Report, (2015).
[22] M. J. A. Tijmensen, A. P.C. Faaij, C. N. Hamelinck, M. R. M. van Hardeveld, Exploration of the possibilities for production of Fischer Tropsch liquids and power via biomass gasification, Biomass and Bioenergy, 23 (2002) 129-152.
[23] P. M. Maitlis, R. Quyoum, H. C. Long, M. L. Turner, Towards a chemical understanding of the Fischer-Tropsch reaction: alkene formation, Applied Catalysis A: General, 186 (1999) 363-374.
[24] Q. Ge, M. Neurock, H. A. Wright, N. Srinivasan, A first principal study of carbon-carbon over {0001} surface of Co and Ru, The Journal of Physical Chemistry B, 106 (2002) 2826-2829.
[25] M. Zhuo, K. F. Tan, A. Borgna, M. Saeys, Density functional theory study of the CO insertion mechanism for Fischer-Tropsch synthesis over Co catalysts, The Journal of Physical Chemistry C, 113 (2009) 8357-7365.
[26] A. Y. Khodakov, W. Chu, P. Fongarland, Advanced in the development of novel cobalt Fischer-Tropsch catalysts for synthesis of long-chain hydrocarbons and clean fuels, Chemical Reviews, 107 (2007), 1692-1744.
[27] O. O. James, B. Chowdhury, M. A. Mesubi, S. Maity, Reflection on the chemistry of the Fischer-Tropsch synthesis, RSC Advances, 2 (2012) 7347-7366.
[28] B. H. Davis, Fischer-Tropsch synthesis: current mechanism and futuristic needs, Fuel Processing Technology, 71 (2001) 157-166.
[29] G. P. van der Laan, A. A. C. M. Beenackers, Kinetics and selectivity of the Fischer-Tropsch synthesis: A literature review, Catalysis Reviews, 41 (1999) 255-318.
[30] P. Biloen, W. M. H. Sachtler, Mechanism of hydrogen synthesis over Fischer-Tropsch catalysts, Advanced in Catalysis, 30 (1981) 165-216.
[31] A. T. Bell, Catalystic synthesis of hydrocarbons over group VIII metals: A discussion of the reaction mechanism, Catalysis Reviews, 23 (1981) 203-232.
[32] R. B. Anderson, R. A Friedel, H. H. Storch, Fischer-Tropsch reaction mechanism involving stepwise growth of carbon chain, The Journal of Chemical Physics, 19 (1951) 313-319.
[33] X. Zhang, W. Qian, H. Zhang, Q. Sun, W. Ying, Effect of the operation parameters on the Fischer-Tropsch synthesis in fluidized bed reactors, Chinese journal of Chemical Engineering, 26 (2018) 245-251.
[34] D. Selvatico, A. Lanzini, M Santarelli, Low temperature Fischer-Tropsch fuels from syngas: Kinetic modeling and process simulation of different plant configuration, Fuel, 186 (2016) 544-560.
[35] B. Shi, L. Wu, Y. Liao, C. Jin, A. Montavon, Explanation of the formation of branched hydrocarbons during Fischer-Tropsch synthesis by alkylidene mechanism, Topics in Catalysis, 57 (2014) 451-459.

[36] N. T. Kemp, N. K. Singh, Evidence of carbon-carbon bond formation on GaAs(100) via Fischer-Tropsch methylene insertion reaction mechanism, Chemical Communications, 34 (2005) 4348-4350.
[37] R. Zhang, L. Kang, LL. He, BJ. Wang, Insight into C-C chain growth in Fischer-Tropsch synthesis on HCP Co(10-10) surface: The effect of crystal facets on the preferred mechanism, Computational Material Science, 145 (2018) 263-279.
[38] H. Jahangiri, J. Bennett, P. Mahjoubi, K. Wilson, S. Gu, A review of advanced catalyst development for Fischer-Tropsch synthesis of hydrocarbons from biomass derived syn-gas, Catalysis Science and Technology, 4 (2014) 2210-2229.
[39] Y. H. Bi, A. K. Dalai, Selective production of C-4 hydrocarbons from syngas using Fe-Co/ZrO2 ans SO42-/ZrO2 catalysts, Canadian Journal of Chemical Engineering, 81 (2003) 230-242.
[40] G. W. Norval, Notes on the issues of equilibrium in the Fischer-Tropsch synthesis, Canadian Journal of Chemical Engineering, 86 (2008) 1062-1069.
[41] M.C. Bell, Thermodynamically controlled catalysis – equilibria in Fischer-Tropsch synthesis, Canadian Metallurgical Quality, 34 (1995) 331-341.
[42] B. Jager, R. Espinoza, Advances in low-temperature Fischer-Tropsch synthesis, Catalysis Today, 23 (1995) 17-28.
[43] D. Hibbitts, E. Dybeck, T. Lawlor, M. Neurock, E. Iglesia, Preferntial activation of CO near hydrocarbon chian during Fischer-Tropsch synthesis on Ru, Journal of catalysis, 337 (2016) 91-101.
[44] E. Iglesia, Design, synthesis, and use of cobalt-based Fischer-Tropsch synthesis catalysts: Review, Applied Catalysis A: General, 161 (1997) 58-78.
[45] R. Guttel, U. Kunz, T. Turkek, Reactors for Fischer-Tropsch synthesis, Chemical Engineering & Technology, 31 (2008) 746-754.
[46] B. Gu, A. Y. Khodakov, V. V. Ordomsky, Selectvity shift from parraffins to alpha-olefins in low-temperature Fischer-Tropsch synthesis in the presence of carboxylic acids, Chemical Communications, 54 (2018) 2345-2248.
[47] T. Riedel, G. Schaub, Low-temperature Fischer-Tropsch synthesis on cobalt catalysts-effects of CO2, Topics in Catalysis, 26 (2003) 145-156.
[48] B. C. Shi, R. A. Keogh, B. H. Davis, Fischer-Tropsch synthesis: The formation of branched hydrocarbons in the Fe and Co catalyzed reaction, Journal of Molecular Catalysis A-Chemical, 234 (2005) 85-97
[49] A. de Klerk, Fischer-Tropsch fuels refinery design, Energy & Environmental Science, 4 (2011) 1177-1205.
[50] X. Guo, G. Liu, E. D. Larson, High-octane production by upgrading low-temperature Fischer-Tropsch syncrude, Industrial & Engineering Chemistry Research, 50 (2011) 9743-9747.
[51] J. H. Ryu, S. H. Kang, J. H. Kim, Fischer-Tropsch synthesis on Co-Al2O3 (promoter)/ZSM5 hybrid catalysts for the production of gasoline range hydrocarbons, Korean Journal of Chemical Engineering, 32 (2015) 1993-1998.
[52] H. T. Luk, C. Mondelli, D. C. Ferre, J. A. Stewart, J. Perez-Ramirez, Status and prospects in higher alchols synthesis from gas, Chemical Society Reviews, 46 (2017) 1358-1426.
[53] E. J. M. Hensen, P. Wang, W. Xu, Research Trends in Fischer-Tropsch catalysts for coal to liquid technology, Frontiers of Engineering Management, 3 (2016) 321-330.

[54] V. Subramani, S. K. Gangwal, A review of recent literature to search for an efficient catalytic process for the conversion of syngas to ethanol, Energy & Fuels, 22 (2008) 814-839.
[55] Q. Zhang, J. Kang, Y. Wang, Development of novel catalysts for Fischer-Tropsch synthesis: Tuning the product selectivity, ChemCatChem, 2 (2012) 1030-1058.
[56] Q. Zhang, W. Deng, Y. Wang, Recent advances in understanding the key catalysts factors for Fischer-Tropsch synthesis, Journal of Energy Chemistry, 22 (2013) 27-38.
[57] S. Storsæter, B. Tøtdal, J. C. Walmsley, B. S. Tanem, A. Holmen, Characterization of alumina-, silica-, and titania-supported cobalt Fischer-Tropsch catalysts, Journal of Catalysis, 236 (2005) 139-152.
[58] S. W. Ho, M. Houalla, D. M. Hercules, Effect of particle size on carbon monoxide hydrogenation activity of silica supported cobalt catalysts Journal of Physical Chemistry, 94 (1990) 6396-6399.
[59] A. H. Kababji, B. Joseph, J. T. Wolan, Silica-supported cobalt catalysts for Fischer-Tropsch synthesis: Effects of calcination temperature and support surfaces area on cobalt silicate formation, Catalysis Letter, 130 (2009) 72-78.
[60] G. L. Bezemer, J. H. Bitter, H. P. C. E. Kuipers, H. Oosterbeek, J. E. Holewijn, X. Xu, F. Kapteijn, A. J. Dillen, K. P. de Jong, Cobalt particle size effects in the Fischer-Tropsch reaction studied with carbon nanofiber supported catalysts, Journal of the American Chemical Society, 128 2006 3956-3964.
[61] A. Y. Khodakov, A. Griboval-Constant, R. Bechara, V. L. Zholobenko, Pore size effects in Fischer Tropsch synthesis over cobalt supported mesoprous silica, Journal of Catalysis, 206 (2002) 230-241.
[62] A. Martínez, C. López, F. Márquez, and I. Díaz, Fischer-Tropsch synthesis of hydrocarbons over mesoporous Co/SBA-15 catalysts: the influence of metal loading, cobalt precursor, and promoters, Journal of Catalysis, 220 (2003) 486-499.
[63] G. Jacobs, T. K. Das, Y. Zhang, J. Li, G. Racoillet, B. H. Davis, Fischer-Tropsch synthesis: support, loading, and promoter effects on the reducibility of cobalt catalysts, Applied Catalysis A: General, 233 (2002) 263-281.
[64] G. Jacobs, Y. Ji, B. H. Davis, D. Cronauer, A. J. Kropf, and C. L. Marshall, Fischer–Tropsch synthesis: Temperature programmed EXAFS/XANES investigation of the influence of support type, cobalt loading, and noble metal promoter addition to the reduction behavior of cobalt oxide particles, Applied Catalysis A: General 333 (2007) 177-191.
[65] B. H. Davis, Fischer-Tropsch synthesis: comparison of performances of iron and cobalt catalysts, Industrial & Chemical Chemistry Research, 46 (2007) 8938-8945.
[66] E. van Steen, M. Claeys, Fischer-Tropsch catalysts for the biomass to liquid process, Chemical Engineering & Technology, 31 (2008) 655-666.
[67] F. G. Botes, J. W. Niemantsveriet, J. van de Loosdrescht, A comparison of cobalt and iron based slurry phase Fischer-Tropsch synthesis, 215 (2013) I12-I20.
[68] M. V. Kulikova, S. N. Khadzhiev, Metal-containing nanodispersions as Fischer-Tropsch catalysts in three-phase slurry reactors, Petroleum Chemistry, 57 (2017) 1173-1176.
[69] M. Y. Ding, Y. Yang, B. S. Wu, Y. W. Li, T. J. Wang, L. L. Ma, study on reduction and carburization of iron-based Fischer-Tropsch synthesis catalyst, Energy Procedia, 61 (2014) 2267-2270.

[70] E. van Steen, G. S. Sewell, R. A. Makhothe, C. Micklethwaite, H. Manstein, M. de Lange, C. T. O'Connor, TPR study in the preparation of impregnation Co/SiO2 catalysts, Journal of Catalysis, 162 (1996) 220-229.
[71] J. P. den Breejen, P. B. Radstake, G. L. Bezemer, J. H. Bitter, V. Frøseth, A. Holmen, K. P. de Jong, On the origin of the cobalt particle size effects in Fischer-Tropsch catalysis, Journal of the American Chemical Society 131 (2009) 7197-7203.
[72] J. van de Loosdrecht,M. van der Haar,A.M. van der Kraan,A.J. van Dillen,J.W. Geus, Preparation and properties of supported cobalt catalysts for Fischer-Tropsch synthesis, Applied Catalysis A: General, 150 (1997) 365-376.
[73] B. Ernst, A. Bensaddik, L. Hilaire, P. Chaumette, A. Kiennemann, Study on a cobalt silica catalyst during reduction and Fischer–Tropsch reaction: in situ EXAFS compared to XPS and XRD. Catalysis today, 39 (1998) 329-341.
[74] A. Y. Khodakov, Fischer-Tropsch synthesis: relations between structure of cobalt catalysts and their catalytic performance, Catalysis Today, 144 (2009) 251-257.
[75] J. Yang, V. Froseth, D. Chen, A. Holmen, Particles size effect for cobalt Fischer-Tropsch catalysts based on in situ CO chemisorption, 648 (2016) 67-73.
[76] O. Ducreux, B. Rebours, J. Lynch, M. Roy-Auberger, D. Bazin. Microstructure of supported cobalt Fischer-Tropsch catalysts, Oil & Gas Science and Technology-Revue, de l'IFP 64 (2009) 49-62.
[77] S. Bessell, Support effects in cobalt-based fischer-tropsch catalysis, Applied Catalysis A: General 96 (1993) 253-268.
[78] G. Prieto, A. Martienz, P. Conception, and R. Moreno-Tost, Cobalt particle size effects in Fischer–Tropsch synthesis: structural and in situ spectroscopic characterisation on reverse micelle-synthesised Co/ITQ-2 model catalysts, Journal of Catalysis 266 (2009) 129-144.
[79] J. Park, Y. Lee, P. R. Karandikar, K. Jun, K. Ha, and H. Park, Fischer–Tropsch catalysts deposited with size-controlled Co3O4 nanocrystals: Effect of Co particle size on catalytic activity and stability, Applied Catalysis A: General 411 (2012) 15-23.
[80] M. E. Dry, The Fisher-Tropsch process: 1950-2000, Catalysis Today, 71 (2002) 227-241.
[81] T. Herranz, S. Rojas, F. J. Pérez-Alonso, M. Ojeda, P. Terreros, J. L. G. Fierro, Genesis of iron carbides and their role in the synthesis of hydrocarbons from synthesis gas, Journal of catalysis 243 (2006) 199-211.
[82] R. M. M. Abbaslou, A. Tavasoli, A. K. Dalai, Effect of pre-treatment on physico-chemical properties and stability of carbon nanotubes supported iron Fischer–Tropsch catalysts, Applied Catalysis A: General 355 (2009) 33-41.
[83] S. Li, R. J. O'Brien, G. D. Meitzner, H. Hamdeh, B. H. Davis, E. Iglesia, Structural analysis of unpromoted Fe-based Fischer–Tropsch catalysts using X-ray absorption spectroscopy, Applied Catalysis A: General 219 (2001) 215-222.
[84] M. Boudart, M. A. McDonald, Structure sensitivity of hydrocarbon synthesis from carbon monoxide and hydrogen, The Journal of Physical Chemistry, 88 (1984) 2185-2195.
[85] D. Barkhuizen, I. Mabaso, E. Viljoen, C. Welker, M. Claeys, E. V. Steen, J. CQ Fletcher, Experimental approaches to the preparation of supported metal nanoparticles, Pure and Applied Chemistry, 78 (2006) 1759-1769.

[86] A. N. Pour, S. Chekreh, M. R. Housaindokht, A. Eftekhari, Structural sensitivity of carbon monoxide hydrogenation by nano-structured iron catalyst, Journal of Nanoscience and nanotechnology, 16 (2016) 5856-5864.
[87] Z. Gholami, N. A. M. Zabidi, F. Gholami, O. B. Ayodele, M. Vakili, The influence of catalyst factors for sustainable production of hydrocarbons via Fischer-Tropsch synthesis, Reviews in Chemical Engineering, 33 (2017) 337-358.
[88] J. X. Liu, P. Wang, W. Xu, E. J. M. Hensen, Particle size and crystal phase effects in Fischer-Tropsch catalysts, Engineering, 3 (2017) 467-476.
[89] M. Melander, K. Laasonen, .H. Jónsson, Effect of Magnetic States on the Reactivity of an FCC (111) Iron Surface, The Journal of Physical Chemistry C, 118 (2014) 15863-15873.
[90] I. Chorkendorff, J. W. Niemantsverdriet, Concept of Modern Catalysis and Kinetics, 3rd Edition, What is Catalysis? Wiley-VCH (2013) 2-3. Print
[91] E. Farnetti, R. Di Monte, J. Kašpar, Homogeneous and heterogeneous catalysis. Inorganic and bioinorganic chemistry, 2 (2009) 50.
[92] G. J. Hutchings, Heterogeneous catalysts-discovery and design, Journal of Material Chemistry, 19 (2009) 1222-1235.
[93] J. W. Niemantsverdriet, Spectroscopy in Catalysis: An Introduction, 3rd Edition, Introduction, Wiley-VCH (2007) 5-7.
[94] P. E. Strizhak, Nanosize effects in heterogenous catalysis. Theoretical and experimental Chemistry, 49 (2013) 2-21.
[95] J. A. Schwarz, Methods for preparation of catalytic materials, Chemical Reviews, 95 (1995) 477-510.
[96] P Munnik, P. E. de Jongh, K. P. de Jong, Recent development in the synthesis of support catalysts, Chemical Reviews, 115 (2015) 6687-6718.
[97] N. Wilde, R. Gläser, Solid materials for heterogenous catalysis, Contemporary Catalysis: Science and Technology Applications, Royal Society of Chemistry, 2013, 353-356.
[98] J. S. Noh, J. A. Schwarz, Estimation of the point of zero charge of simple oxides by mass titration. Journal of Colloid and Interface Science, 130 (1989) 157-164.
[99] J. Park, J. R. Regalbuto, A simple, accurate determination of oxide PZC and the strong buffering effect of oxide surfaces at incipient wetness. *Journal of colloid and interface science*, *175* (1995) 239-252.
[100] W.A. Spieker, J. R. Regalbuto, A fundamental model of platinum impregnation onto alumina, Chemical Engineering Science, 56 (2001) 3491-3504.
[101] X. Hao, W. A. Spieker, J. R. Regalbuto, A further simplification of the revised physical adsorption (RPA) model. Journal of colloid and interface science, 267 (2003) 259-264.
[102] J.R. Regalbuto, A scientific method to prepare supported metal catalysts, Surface and Nanomolecular Catalysis, (2006) 161-194.
[103] S. L. Soled, E. Iglesia, R. A. Fiato, J. E. Baumgartner, H. Vroman, S. Miseo, Control of metal dispersion and structure by changes in the solid-state chemistry of supported cobalt Fischer-Tropsch Catalysts, Topics in Catalysis, 26 (2003) 101-109.
[104] K. Al-Dalama, A. Stanislaus, A comparative study of the influence of chelating agents on the gydrodesulfurization (HDS) activity of alumina and silica-alumina supported CoMo catalysts, Energy & Fuels 20 (2006) 1777-1783.

[105] M. Schreier, J. R. Regalbuto, A fundamental study of Pt tetraammine impregnation of silica: 1. The electrostatic nature of platinum adsorption, Journal of Catalysis, 1 (2004) 190-202.
[106] A. M. Shah, J. R. Regalbuto, Retardation of Pt adsorption over oxide support at pH extreme: Oxide dissolution or high ionic strength, Langmuir, 10 (1994) 500-504.
[107] A. Feller, M. Claeys, E. van Steen, Cobalt Cluster Effects in Zirconium Promoted Co/SiO2 Fischer–Tropsch Catalysts, Journal of Catalysis, 185 (1999) 120–130.
[108] J. P. den Breejen, J. R. A. Sietsma, H. Friedrich, J. H. Bitter, K. P. de Jong, Design of supported cobalt catalysts with maximum activity for the Fischer-Tropsch synthesis, Journal of Catalysis, 270 (2010) 146–152.
[109] R. Reuel, C. H. Bartholomew, Effects of Support and Dispersion on the CO Hydrogenation Activity / Selectivity Properties of Cobalt, Journal of Catalysis, 85 (1984) 78– 88.
[110] A. S. Lisitsyn, A. V. Golovin, V. L. Kuznetsov, Y. I. Yermakov, Properties of catalysts prepared by pyrolysis of Co2(CO)8 on silica containing surface Ti ions, Journal of Catalysis, 95 (1985) 527–538.
[111] J. Grams, A. Ura, W. Kwapiński, ToF-SIMS as a versatile tool to study the surface properties of silica supported cobalt catalyst for Fischer–Tropsch synthesis. *Fuel*, *122* (2014) 301-309.
[112] Ø. Borg, P. D. C. Dietzel, A. I. Spjelkavik, E. Z. Tveten, J. C. Walmsley, S. Diplas, S. Eri, A. Holmen, E. Rytter, Fischer-Tropsch synthesis: Cobalt particle size and support effects on intrinsic activity and product distribution, Journal of Catalysis, 259 (2008) 161–164.
[113] A. Y. Khodakov, J. Lynch, D. Bazin, B. Rebours, N. Zanier, B. Moisson, P. Chaumette,. Reducibility of cobalt species in silica-supported Fischer–Tropsch catalysts. Journal of Catalysis, 168 (1997) 16-25.
[114] G. Prieto, A. Martínez, P. Concepción, R. Moreno-Tost, Cobalt particle size effects in Fischer–Tropsch synthesis: structural and in situ spectroscopic characterisation on reverse micelle-synthesised Co/ITQ-2 model catalysts, Journal of Catalysis, 266 (2009) 129-144.
[115] H. Xiong, Y. Zhang, K. Liew, J. Li, Fischer–Tropsch synthesis: the role of pore size for Co/SBA-15 catalysts. Journal of Molecular Catalysis A: Chemical, 295 (2008), 68-76.
[116] Z. Zsoldos, T. Hoffer, L. Guczi, Structure and catalytic activity of alumina-supported platinum-cobalt bimetallic catalysts. 1. Characterization by x-ray photoelectron spectroscopy, Journal of Physical Chemistry, 95 (1991) 798–801.
[117] D. Schanke, S. Vada, E. A. Blekkan, A. M. Hilmen, A. Hoff, A. Holmen, Study of Pt-promoted cobalt CO hydrogenation catalysts. Journal of Catalysis, 156 (1995) 85-95.
[118] S. Vada, A. Hoff, E. Ådnanes, D. Schanke, A. Holmen, Fischer-Tropsch synthesis on supported cobalt catalysts promoted by platinum and rhenium. Topics in Catalysis, 2 (1995) 155-162.
[119] G. Jacobs, T. K. Das, P. M. Patterson, J. Li, L. Sanchez, B. H. Davis, Fischer–Tropsch synthesis XAFS: XAFS studies of the effect of water on a Pt-promoted Co/Al2O3 catalyst. Applied Catalysis A: General, 247 (2003) 335-343.
[120] W. Ma, G. Jacobs, R. A. Keogh, D. B. Bukur, B. H. Davis, Fischer–Tropsch synthesis: Effect of Pd, Pt, Re, and Ru noble metal promoters on the activity and selectivity of a 25% Co/Al2O3 catalyst. Applied Catalysis A: General, 437 (2012) 1-9.

[121] S. Saedy, D. Palagin, O. Safonova, J. A. van Bokhoven, A. A. Khodadadi, Y. Mortazavi, Y, Understanding the mechanism of synthesis of Pt 3 Co intermetallic nanoparticles via preferential chemical vapor deposition. Journal of Materials Chemistry A, 5 (2017) 24396-24406.
[122] J. M. Christensen, A. J. Medford, F. Studt, A. D. Jensen, High pressure CO hydrogenation over bimetallic Pt–Co catalysts. Catalysis letters, 144 (2014), 777-782.
[123] C. W. Tang, C. B. Wang, S. H. Chien, Characterization of cobalt oxides studied by FT-IR, Raman, TPR and TG-MS. Thermochimica Acta, 473 (2008) 68-73.
[124] B. A. Sexton, A. E. Hughes, T. W. Turney, An XPS and TPR study of the reduction of promoted cobalt-kieselguhr Fischer-Tropsch catalysts. *Journal of catalysis*, *97* (1986) 390-406.
[125] V. Montes, M. Boutonnet, S. Järås, M. Lualdi, A. Marinas, J.M. Marinas, F.J. Urbano, M. Mora, Preparation and characterization of Pt-modified Co-based catalysts through the microemulsion technique: Preliminary results on the Fischer–Tropsch synthesis, In Catalysis Today, 223 (2014) 66-75.
[126] V. Vosoughi, A. K. Dalai, N. Abatzoglou, Y. Hu., Performances of promoted cobalt catalysts supported on mesoporous alumina for Fischer-Tropsch synthesis. Applied Catalysis A: General, 547 (2017) 155-163.
[127] H. Karaca, O. V. Safonova, S. Chambrey, P. Fongarland, P. Roussel, A. Griboval-Constant, A. Y. Khodakov, A. Y. Structure and catalytic performance of Pt-promoted alumina-supported cobalt catalysts under realistic conditions of Fischer–Tropsch synthesis. *Journal of catalysis*, *277* (2011) 14-26.
[128] W. Chu, P. A. Chernavskii, L. Gengembre, G. A. Pankina, P. Fongarland, A. Y. Khodakov, Cobalt species in promoted cobalt alumina-supported Fischer–Tropsch catalysts, Journal of Catalysis, 252 (2007) 215-230.
[129] T. O. Eschemann, J. Oenema, K. P. de Jong, Effects of noble metal promotion for Co/TiO2 Fischer-Tropsch catalysts, Catalysis Today, 261 (2016) 60-66.
[130] N. Tsubaki, S. Sun, K. Fujimoto, Different Functions of the Noble Metals Added to Cobalt Catalysts for Fischer–Tropsch Synthesis, Journal of Catalysis, 199 (2001) 236-246.
[131] C. Pirola, M. Scavini, F. Galli, S. Vitali, A. Comazzi, F. Manenti, P. Ghigna, Fischer–Tropsch synthesis: EXAFS study of Ru and Pt bimetallic Co based catalysts, Fuel, 132 (2014) 62-70.
[132] D. Nabaho, J.W. (Hans) Niemantsverdriet, M. Claeys, E. van Steen, Hydrogen spillover in the Fischer–Tropsch synthesis: An analysis of gold as a promoter for cobalt–alumina catalysts, Catalysis Today, 275 (2016) 27-34.
[133] D. Xu, W. Li, .H Duan, Q. Ge, H. Xu, Reaction performance and characterization of Co/Al2O3 Fischer--Tropsch catalysts promoted with Pt, Pd and Ru, Catalysis Letters, 102 (2005) 229-235.
[134] S. Li, S. Krishnamoorthy, A. Li, G. D. Meitzner, E. Iglesia, Promoted iron-based catalysts for the Fischer–Tropsch synthesis: design, synthesis, site densities, and catalytic properties. Journal of Catalysis, 206 (2002) 202-217.
[135] T. Li, Y. Yang, C. Zhang, Z. Tao, H. Wan, X. An, Y. Li, Phase transformation and textural properties of an unpromoted iron Fischer–Tropsch catalyst. Colloids and Surfaces A: Physicochemical and Engineering Aspects, 302 (2007) 498-505.

[136] J. Xu, C. H. Bartholomew, J. Sudweeks, D. L. Eggett, Design, synthesis, and catalytic properties of silica-supported, Pt-promoted iron Fischer–Tropsch catalysts. Topics in catalysis, 26 (2003) 55-71.
[137] C. H. Zhang, Y. Yang, B. T. Teng, T. Z. Li, H. Y. Zheng, H. W. Xiang, Y. W. Li, Study of an iron-manganese Fischer–Tropsch synthesis catalyst promoted with copper. Journal of Catalysis, 237 (2006) 405-415.
[138] T. Herranz, S. Rojas, F. J. Pérez-Alonso, M. Ojeda, P. Terreros, J. L. G. Fierro, Hydrogenation of carbon oxides over promoted Fe-Mn catalysts prepared by the microemulsion methodology. Applied Catalysis A: General, 311 (2006) 66-75.
[139] F. G. Botes, J. W. Niemantsverdriet, J. Van De Loosdrecht, A comparison of cobalt and iron based slurry phase Fischer–Tropsch synthesis. *Catalysis today*, *215* (2013) 112-120.
[140] Y. Ishikawa, K. Kawaguchi, Y. Shimizu, T. Sasaki, N. Koshizaki, Preparation of Fe–Pt alloy particles by pulsed laser ablation in liquid medium. Chemical physics letters, 428 (2006) 426-429.
[141] M. Ding, Y. Yang, B. Wu, Y. Li, T. Wang, L. Ma, Study on reduction and carburization behaviors of iron-based Fischer-Tropsch synthesis catalyst. Energy Procedia, 61 (2014) 2267-2270.